On Thermospheric Density and Wind Modeling Driven by Satellite Observations

by

Daniel A. Brandt

A dissertation submitted in partial fulfillment
of the requirements for the degree of
Doctor of Philosophy
(Climate and Space Sciences and Engineering)
in The University of Michigan
2021

Doctoral Committee:

Professor Aaron J. Ridley, Chair
Professor Stephen W. Bougher
Associate Professor Ilya V. Kolmanovsky
Associate Professor Shasha Zou

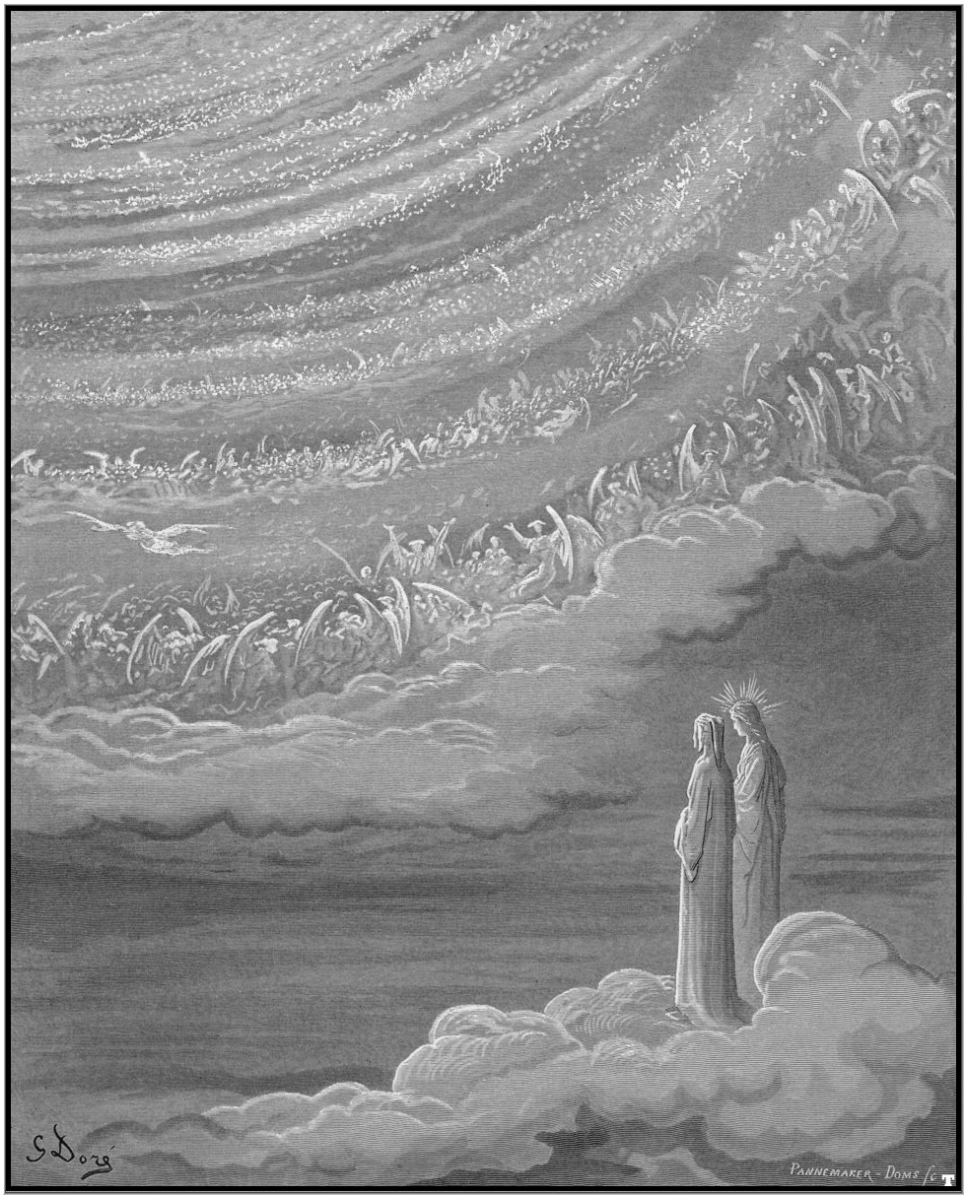
G. Doré
PANNEMAKER - DOMS fc

Daniel A. Brandt

branddan@umich.edu

ORCID id: 0000-0003-3034-5440

In honor of the Holy Face, and St. Alphonsus Maria de Ligouri.

ACKNOWLEDGEMENTS

My principal thanks are to be given to Divine Providence, by which through a series of unforeseen circumstances I was graced with the opportunity to conduct research at one of the most reputable and well-supported institutions in the nation.

Among mortals, my chief thanks is extended to Professor Aaron Ridley, who in great generosity and faith took me on a graduate student, and was persistently supportive and patient of my career aspirations, especially in light of a process of discernment that was lengthy, arduous, and truly tried the patience of my friends, colleagues, and family. Whether it is the fellowships I applied to, the manuscripts I wrote, or the conferences I presented at, each of these endeavors would not have occurred, much less successfully, without your guidance, tireless editing, and practical wisdom.

I extend additional thanks to Dr. Charles Bussy-Virat, Your mentorship and insight regarding SpOCK, as well as your moral support of the pursuit of my pilot's license was invaluable. In many ways, you are very much the standard by which I measured my own progress at Michigan.

I am also very thankful to Professor Mark Moldwin. Whether it is through your space instrumentation class, your willingness to sit on the committee of my first qualification exam, your persistent support of me seeking out chances to develop my aptitude for public speaking, or your continuous relaying of opportunities for professional development, your tireless work in support of myself and other students has been exemplary and has served as a model for myself as to what selfless mentorship

looks like.

I am deeply grateful to Fr. John of God, MC, who's spiritual guidance during these last several years has provided invaluable wisdom and aided me greatly both in discernment and the cultivation of virtues I will continue to take a lifetime to perfect. It has been through your guidance that the cacophony of my misguided intellect, reason, and will, and my misdirected passions has grown far more sonorous and properly-ordered under the principles of St. Ignatius of Loyola.

I must also thank Agnit Mudkhopadhyay, Colten Peterson, Brandon Ponder, and Brian Swiger, as well as the numerous other colleagues and fellow students who have aided me very much in bolstering mastery of the topics of my subfield and with programming challenges it would have otherwise taken me a significant amount of time to overcome.

A special thanks is extended to Anthony Allen, Jonathan Altes, Ralf Bejko, Jacob Dale, Alfred Kalantar, and the rest of my brothers of the parish. Your prayers and admonitions in regards to the care of my soul and the right application of my reason in concert with virtue have been indispensable, especially during particularly difficult times of desolation and trial, and during my discernment. It would not be possible for me to have felt home at Michigan without your friendship. Truly, as Solomon writes, "Iron sharpens iron, and one man sharpens another."

Last, but not least, I give my thanks to CLaSP. As far as memory serves, every professor, administrator, or student I've needed assistance, guidance, or mentorship from has aided me above and beyond what was necessary or pointed me in the right direction, and so frequently as well. It has been a privilege to conduct research in this department, and additionally be graced so generously with opportunities for outreach, networking, special projects, interdisciplinary work, mentorship, and the like. I am deeply indebted to CLaSP for these reasons, and many more that elude recollection.

TABLE OF CONTENTS

LIST OF FIGURES

Figure

LIST OF TABLES

Table

LIST OF ABBREVIATIONS

AE Auroral Electroject Index

ACE Advanced Composition Explorer

AGI Analytical Graphics Incorporated

APOPT ap Optimization Subprocess

AROPT Area Optimization Subprocess

CAD Computer-Aided Design

CHAMP CHAllenging Minisatellite Payload

CIR Corotating Interaction Region

CIRA COSPAR International Reference Atmosphere

CME Coronal Mass Ejection

CTIM Coupled Thermosphere-Ionosphere Model

CTIPe Coupled Thermosphere Ionosphere Plasmasphere electrodynamics Model

CYGNSS Cyclone Global Navigation Satellite System

DCA Dynamic Calibration Atmosphere

DMDc Dynamic Mode Decomposition with control

DOY Day-of-the-Year

Dst Disturbance Storm Time

DTM Drag-Temperature Model

EGG Electrostatic Gravity Gradiometer

EIA Equatorial Ionization Anomaly

EUV Extreme Ultraviolet Radiation

EGM96 Earth Gravitational Model 1996

ESA European Space Agency

EVE Extreme Ultraviolet Variability Experiment

FAC Field-Aligned Current

FISM Flare Irradiance Spectrum Model

FOPT F10.7 Optimization Subprocess

FPI Fabry-Perot Interferometer

FUV Far-Ultraviolet

GCM Global Climate Model

GPS Global Positioning System

GRACE Gravity Recovery and Climate Experiment

GITM Global Ionosphere-Thermosphere Model

GOCE Gravity Field and Steady-State Ocean Circulation Explorer

HF High-Frequency

JB Jacchia-Bowman

HASDM High-Accuracy Satellite Drag Model

HWM Horizontal Wind Model

ICME Interplanetary Coronal Mass Ejection

IGRF International Geomagnetic Reference Field

IMF Interplanetary Magnetic Field

IRI International Reference Ionosphere

ISR Incoherent Scatter Radar

ISRO Indian Space Research Organization

LEO Low-Earth Orbit

ME Mean Error

MF Medium-Frequency

MLT Magnetic Local Time

MLAT Magnetic Latitude

MOA Multifaceted Optimization Algorithm

MSIS Mass Spectrometer and Incoherent Scatter Radar

NASA National Aeronautics and Space Administration

NCAR National Center for Atmospheric Research

NOAA National Oceanographic and Atmospheric Administration

NRLMSISE-00 United States Naval Research Laboratory Mass Spectrometer and Incoherent Scatter Radar Atmospheric Model

POD Precise Orbit Determination

ROM Reduced-Order Model

RMS Root-mean-square

SDO Solar Dynamics Observatory

SEA Superposed Epoch Analysis

SLR Satellite Laser Ranging

SpOCK Spacecraft Orbital Characterization Kit

SSC Storm Sudden Commencement

SSN Sunspot Number

SVD Singular Value Decomposition

SWPC Space Weather Prediction Center

Sq Solar-Quiet

TAD Traveling Atmospheric Disturbance

TGCM Thermosphere General Circulation Model

TIE-GCM Thermosphere-Ionosphere-Electrodynamics General Circulation Model

TIME-GCM Thermosphere-Ionosphere-Mesosphere-Electrodynamics General Circulation Model

TIMED Thermosphere-Ionosphere-Mesosphere Energetics and Dynamics

TLE Two-line Element Set

UARS Upper Atmospheric Research Satellite

UCL University College of London

UT Universal Time

UTC Universal Coordinated Time

UV Ultraviolet Radiation

VHF Very High Frequency

WATS Wind and Temperature Spectrometer

WDCG World Data Center for Geomagnetism

WGS84 Word Geodetic System 1984

ABSTRACT

The thermosphere is home to a plethora of orbiting objects ranging in size from flecks of paint to modular spacecraft with masses on the order of thousands of kilograms. The region spans hundreds of kilometers in vertical extent, from ∼100 km where fixed-wing flight by aerodynamic lift is unsupportable, out to ∼500-700 km, depending on solar activity, where the particle density is so sparse that the atmosphere can no longer be treated as a fluid. The thermosphere is subject to dynamical energy input from radiation and magnetic sources that make quantifying its dynamics a nontrivial endeavor. This is particularly a challenge during geomagnetic storms, where increased magnetic activity primarily at high-latitudes drives global heating, traveling atmospheric disturbances, and intense winds throughout the thermosphere. Modeling of the neutral density and horizontal winds is a challenging endeavor for these conditions, and it is vital not only for understanding the physics of neutral atmospheres, but also for the practical purposes of improving orbit prediction, as the thermosphere is home to an increasing number of satellite missions, in addition to being the abode of astronauts.

Various atmospheric models have been constructed and developed over decades in order to model the thermosphere, with the most prominent being the empirical models MSIS-00, JB-2008, and DTM-2013, which are primarily used to model the neutral density, and GITM, a physics-based model capable of modeling atmospheric electrodynamics and investigating thermospheric winds.

This dissertation focuses on three important means by which the interplay between satellite measurements and atmospheric models can drive scientific development for

use in satellite mission operations and model development outright. In order to reduce the empirical mode bias during storms, we created the Multifaceted Optimization Algorithm (MOA), a method to modify the drivers of the models by comparing actual and simulated orbits through the model to reduce the errors. Applying MOA to the MSIS-00 model allowed a decrease in model error from 25% to 10% in the event that was examined, and represents an easy-to-implement technique that can use publicly available two-line-element orbital data. A superposed epoch analysis of three empirical density models shows persistent storm-time overestimation by JB-2008 and underestimation DTM-2013 by MSIS-00 for more intense geomagnetic storms that may be addressed with a Dst-based calibration, and a statistical analysis of GITM horizontal winds indicates the best performance in the polar and auroral zones and difficulty capturing seasonality.

The work contained in this dissertation aims to provide techniques and analysis tools to improve density and wind model performance, in order to support satellite mission operators and atmospheric research. Ultimately, it demonstrates that simple tools and methods can be utilized to generate significant results and scientific insight, serving to augment and supplement more computationally intensive and cost-prohibitive strategies for investigating the thermospheric environment.

CHAPTER I

Introduction

The upper atmosphere is a unique region which has been the subject of growing scientific inquiry starting in the decades following WWII (*Larsen* 2003). Satellites deployed into the region since the 1970s have afforded the opportunity to investigate the physics and dynamics of this region, and therefore grant the capability of developing atmosphere models. Products of these models of particular importance are their predictions of winds and densities, which have a great impact on the structure of the atmosphere and the orbits of numerous spacecraft. This dissertation focuses on three ways data from spacecraft orbiting in the upper atmosphere have driven forwards developments in those models.

1.1 Description of the Upper Atmosphere

1.1.1 The Thermosphere and Ionosphere

The terrestrial atmosphere consists of several layers: (1) The troposphere, from the surface to ∼10 km in altitude, (2) the stratosphere, from ∼10 km to ∼50 km, (3) the mesosphere between ∼50 km and ∼ 90 km, (4) the thermosphere between ∼90 km and ∼500 km, and (5) the exosphere, the extraordinarily diffuse layer of the upper atmosphere that fades into space as the geocorona, which may extend past

lunar orbit (*Baliukin et al.*, 2019). Numerous Low-Earth Orbit (LEO) satellites orbit below 2,000 km, with orbits passing through or completely within the thermosphere.

1.1.1.1 The Thermosphere

The lower regions of the thermosphere consist primarily of N_2 and O_2, but the upper regions are dominated by atomic oxygen (O), due to the impact of photodissociation and molecular diffusion at high altitudes. The thermosphere is sensitive to energy input from solar heating and geomagnetic/auroral processes, and its dynamics are influenced by the resulting pressure gradients and dissipative processes.

The temperature in the thermosphere increases dramatically with altitude, and while it is primarily influenced by solar Ultraviolet Radiation (UV) and Extreme Ultraviolet Radiation (EUV) radiation, the overall temperature profile exhibits a baseline variation due to the ∼11 year solar cycle, as well as shorter variations based on the 27-day solar rotation (*Craig*, 1965). Figure 1.1 shows the relationship between the global mean temperature profile and the solar activity (represented by $F_{10.7}$, the solar 10.7 cm radio emission, which correlates with solar EUV).

A full 33% of the energy deposition driven by EUV and UV radiation goes to dissociation of molecular oxygen ($O_2 + h\nu \rightarrow 2O$), while the remaining 67% is radiated vertically in either direction (*Schunk and Nagy*, 2018). The primary way the thermosphere undergoes cooling is through downward molecular heat conduction, and secondarily via NO and CO_2 infrared emissions that are affected by solar variability (*Mlynczak et al.*, 2014).

The auroral processes that influence thermospheric temperatures find their origin the interaction of the solar wind with the terrestrial geomagnetic field. The energy carried to Earth by the solar wind is primarily transferred to the thermosphere by the Field-Aligned Current (FAC). These FACs (also called Birkeland currents) deposit the incoming energy at high-latitudes in two regions that form a closed current via

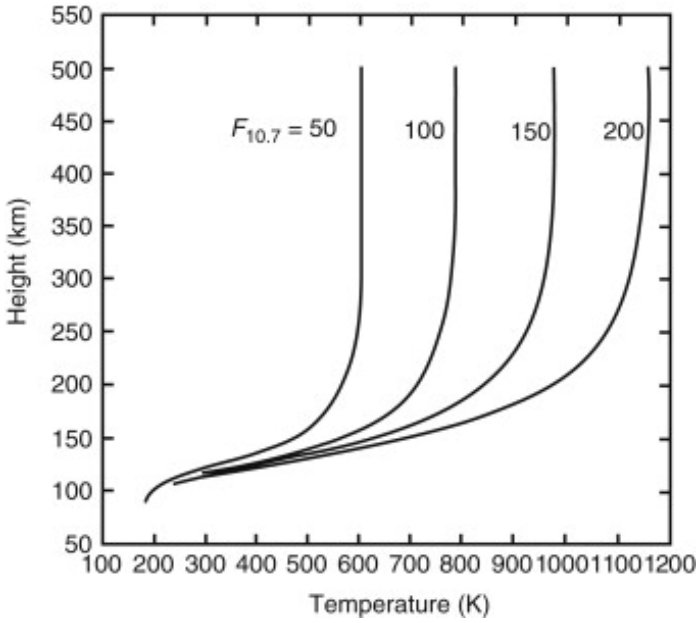

Figure 1.1: Thermosphere temperature profiles as a function of solar flux, from *Solomon and Roble* 2015.

the Pedersen current which flows between the footprint of each zone in the lower ionosphere, and across the polar cap in a series of current loops (*Le et al.*, 2010). Auroral particles cause ionization, followed by exothermic reactions that create photoelectrons that heat up the neutrals. In particle precipitation, the incoming energetic species lose their energy by collisions with N_2 and O_2 (*Jones and Rees*, 1973). The chemical processes facilitated by these collisions excite various atomic and molecular energy levels, generating a visible airglow (*Frederick and Hays*, 1978), and they play a pivotal role in changing the composition of the atmosphere, particularly in changes to the budget of atmospheric nitric oxides (NO_x = N, NO, NO_2), affecting cooling rates (*Venkataramani et al.* 2016, *Lu et al.* 2010, and *Mlynczak et al.* 2010) and catalyzing ozone destruction in the atmosphere below (*Sinnhuber et al.*, 2012).

The thermosphere responds to the heating brought on through solar and auroral processes with vertical motion consisting in three components: (1) a barometric motion that represents the vertical movement of constant-pressure surfaces due to thermal expansion (*Mayr et al.* 1978 and *Prölss* 1980), (2) vertical winds associated

with horizontal wind divergence through mass continuity (*Larsen and Meriwether* 2012 and *Rishbeth et al.* 1987), and (3) non-hydrostatic driving, where the pressure-gradient force (∇P) becomes out of balance with gravity (g), and vertical winds can be accelerated until ∇P becomes equivalent to g again (*Deng et al.*, 2008). The wind then over compensates, so that ∇P needs to re-balance again, resulting in a wave structure to the vertical wind, pressure, and density (*Deng et al.*, 2021). That barometric motion, often termed 'upwelling', changes the scale height (Eq. 1.1) of the local atmosphere, which has the form

$$H = \frac{kT}{mg} \tag{1.1}$$

where the Boltzmann constant $k = 1.38 \times 10^{-23} \mathrm{J} \cdot \mathrm{K}^{-1}$, T = Temperature, m is the mean mass of a species in kg, and g is the local acceleration due to gravity. This quantity, which represents the increase in altitude for which the atmospheric pressure decreases by a factor of e, results in an increase in the local density at an altitude, when incorporated into the barometric equation (Eq. 1.2), which is of the form

$$\begin{aligned} \frac{1}{H} &= -\frac{1}{\rho}\frac{\mathrm{d}\rho}{\mathrm{d}z} \\ \rho &= \rho_0 e^{-\frac{z-z_0}{H}} \end{aligned} \tag{1.2}$$

where ρ represents the neutral density, ρ_0 represents the density at lower atmospheric level, and z_0 is the reference altitude.

Satellites orbiting in LEO experience a drag force of the following form

$$F_D = ma_D = \frac{1}{2}\rho C_D A v^2 \tag{1.3}$$

where F_D is the drag force, m is the mass of the satellite, a_D is the acceleration due

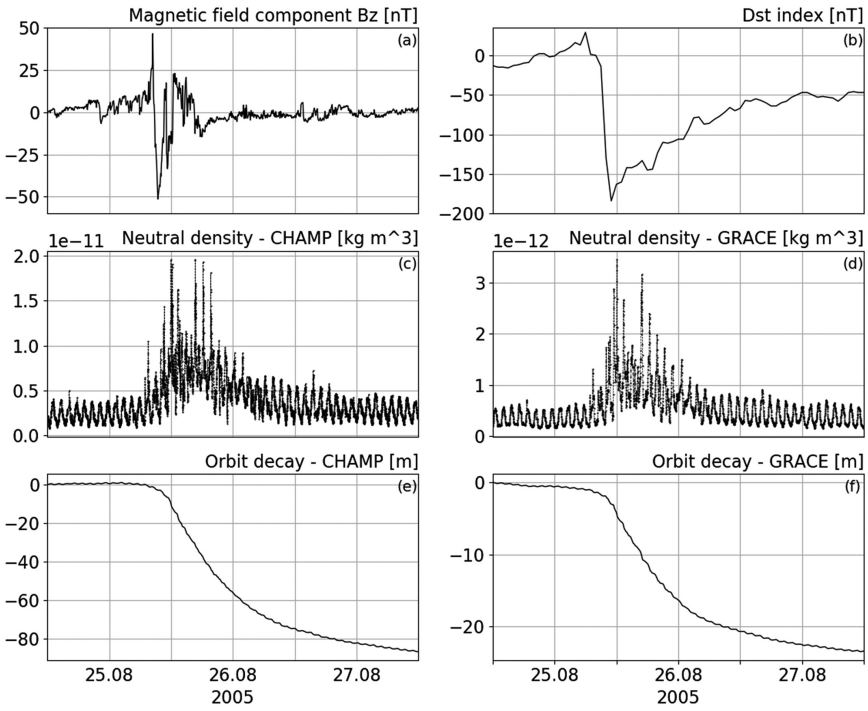

Figure 1.2: CHAMP and GRACE orbit decay rates increasing during a surge in geomagnetic activity (lowest row).

to drag, ρ is the local mass density, v is the flow velocity relative to the satellite, C_D is the drag coefficient which is dependent on gas-surface interactions and the viscosity, and A is the cross-sectional area of the satellite in the direction of motion. An increase in the local neutral density due to heating thus translates into an increase in the drag experienced by LEO satellites, causing their orbits to decay more rapidly (Figure 1.2).

The physics underlying these changes in the thermospheric density has been a subject of much investigation and inquiry, given that they have such a major a impact on satellite orbits (*Oliveira and Zesta*, 2019). Geomagnetic storms are the major source of the most rapid, significant, global density changes that affect satellites in this way. In the next section, an overview of geomagnetic storms is given.

1.1.1.2 The Ionosphere

The thermosphere overlaps with the ionosphere, a region of gas ionized by X-rays and EUV from the Sun. It has a tendency to separate into five layers (Fig. 1.3), which stratify most prominently during the daytime, when ionization is strongest (*Schunk and Nagy* 2018). In the D-region (60-90) km and E-region (90-150 km), the dominant ions are NO^+, O_2^+, and N_2^+, with X-ray wavelengths driving heating and photoionization in the former and EUV radiation doing so in the latter, and loss processes dominated by dissociative recombination (for example: $O_2^+ + e^- \rightarrow 2O$). High-Frequency (HF) radio waves are strongly absorbed in the D-region, while Medium-Frequency (MF) radio waves are reflected in the E-region. The D-region is significantly reduced at night, and the ion density in the E-region during the day is on the order of 10^5 cm^{-3}. Collisions between neutrals and ions drag the ions across geomagnetic field lines, while there are very few collisions between the neutrals and the electrons. The flow difference between the ions and electrons drives a current system. The most important of these current systems is the Solar-Quiet (Sq) current system driven by EUV radiation. It is dominated by the diurnal tide, a daily large-scale oscillation in atmospheric wind, temperature, density, and pressure that moves westward as the Earth rotates. Horizontal winds reaching up to $\sim$ 100m/s drive this tide, causing the Sq current to maximize at 150 km (*Kohl and King* 1967, *Hays et al.* 1994, and *Lindzen and Chapman* 1969). The F-region extends from 140 to nearly 800 km, and separates into two layers during the day. In the F_1-region (150-250 km) NO^+ and O^+ are found, with O^+ dominating just above 200 km. Charge exchange and transport processes become important in this region. The F_2-region (250-800 km) contains the ionization maximum that occurs as a result of the balance between plasma transport and chemical processes. The peak density in F_2-region (also known as the F-region peak) is on the order of 10^6 cm^{-3}. In this region, processes such as plasma diffusion along magnetic field lines (*Jin and Maruyama* 2008), thermospheric winds driving

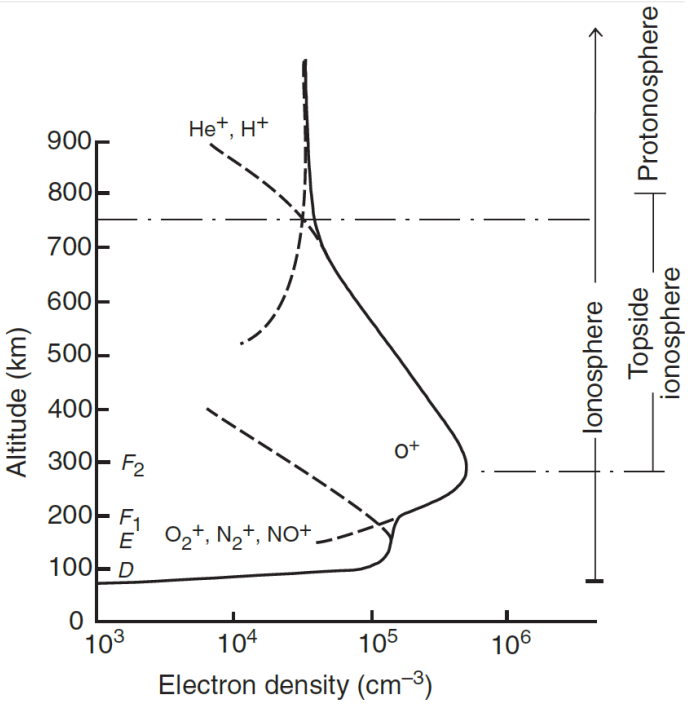

Figure 1.3: Representative ion density profiles for the daytime mid-latitude ionosphere, layer by layer (*Schunk and Nagy* 2018).

plasma along field lines (*Blanch and Altadill* 2012), and ambipolar diffusion (*Gong et al.* 2012) become highly important. The topside ionosphere (technically, the layer above the peak density, but often >300 km) increasingly features He^+ and H^+, and becomes completely ionized.

The ionosphere is coupled to the thermosphere, with ion-neutral collisions contributing to heating and enhancements of the thermospheric density. The Joule heating driven by currents in the ionosphere plays a significant role in the dynamics of thermosphere, affecting its composition and playing a role in how energy and momentum is distributed globally, especially during periods of elevated activity (*Johnson et al.* 1995). This is explained in detail in the subsequent sections.

1.1.2 Geomagnetic Storms

The interaction between the solar wind and Earth's magnetic field forms a cavity called the magnetosphere (*Chapman and Ferraro* 1930). The magnetosphere is asymmetric, extending roughly 10 Earth radii in the sunward direction and beyond 200 Earth radii in the antisunward direction (*Parks* 1991). As the incoming solar wind travels at supersonic speeds, its impact and subsequent abrupt slowing down upon impacting the geomagnetic field on the sunward side forms a bow shock (*Gedalin* 2001). The magnetopause is the boundary where the solar wind dynamic pressure balances the pressure of the geomagnetic field, and the magnetosheath is the region between the bow shock and the magnetopause (*Heikkila* 2011). The inflow of solar plasma happens in a periodic manner known as the Dungey Convection Cycle (*Dungey* 1961 and *Zhang et al.* 2015), where ionospheric plasma flows antisunward over the polar cap, and following reconnection of the field lines in the tail, this plasma is redirected sunward and injected at auroral latitudes, depositing energy in the form of particle precipitation and Joule heating in thermosphere (*Milan et al.* 2007) and completing the two-cell convection of plasma in the ionosphere (*Snevkik et al.*). This process establishes that the Sun, solar wind, magnetosphere, and ionosphere-thermosphere system are all coupled. Geomagnetic storms operate within this complex system.

Geomagnetic storms themselves are disturbances of the terrestrial magnetosphere brought on by either a solar wind shock or interplanetary plasma structures that interconnect with the Earth's magnetic field (*Gonzalez et al.* 1994). The origin of geomagnetic storms ultimately lies in the Sun, and the phenomena transferred from it to Earth along the Interplanetary Magnetic Field (IMF). Storms are brought on by two sources: (1) a Coronal Mass Ejection (CME), or (2) a Corotating Interaction Region (CIR).

A CME (Figure 1.4) is a powerful release of plasma and magnetic field from the surface of the sun into the heliosphere that can travel at speeds reaching 2,500 km/s

and with masses of up to 10^{16}g (*Byrne et al.* 2010). CMEs tend to be released more frequently when the sun is active, as shown by higher Sunspot Number (SSN) levels (*Ramesh* 2010). CMEs typically consists of three distinct parts: a leading edge with a shock, a magnetized interior region, and a magnetic void (*Illing and Hundhausen* 1985). Structures in the solar corona, the aura of plasma surrounding the Sun that extends millions of km into space and can reach temperatures exceeding 1×10^6 K, can accelerate, deform, and deflect CMEs (*Jones et al.* 2017), and variations in the solar wind speed can either enable the CME to accelerate or decelerate (*Tucker-Hood et al.* 2015). A CME propagating through the solar wind en route to Earth develops into an Interplanetary Coronal Mass Ejection (ICME), and the arrival of the leading shock wave at the terrestrial magnetosphere compresses it on the day side and stretches the night side magnetic tail. When the magnetosphere reconnects on the night side, terawatts of power can be released that is directed back to the thermosphere, beginning at high latitudes. CME-driven storms may last 1-3 days, tend to be dominant during solar maximum, cause moderate spacecraft surface charging, and distort the Earth's magnetic dipole very strongly (*Borovsky and Denton* 2006). More than 70% of all geomagnetic storms are caused by ICMEs that arrive at Earth (*Mendaza et al.* 2017).

A CIR (Figure 1.5) is a persistent large-scale plasma structure formed in the low- and middle-latitude regions of the heliosphere by the interaction of a stable fast solar wind stream with the surrounding slow solar wind. Fast solar wind (typically ∼800 km/s) is ejected from coronal holes on the Sun's surface, cooler regions of the corona with open magnetic field lines, and this fast solar wind rams into slower flowing wind (typically ∼400 km/s) ahead of it, and can form a structure containing an intense magnetic field that can last for several solar rotations. These structures are typically composed of two components: (1) a forward shock moving into the slow wind ahead and (2) a reverse shock which is moving backwards into the fast stream (*Heber et al.* 1999). The distinct boundary between the forward and reverse shock, where proton

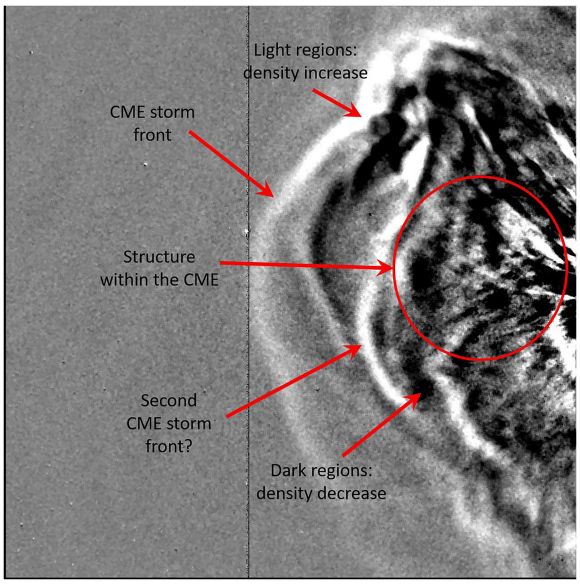

Figure 1.4: An image of a CME taken by the STEREO-A spacecraft showing several distinct features within the CME (*Jones et al.* 2020).

temperature abruptly increases and the speed rises, is often described as the interface region (*Gosling et al.* 1978 and *Wimmer-Schweingruber et al.* 1997). CIR-driven storms tend to be more common during solar minimum, tend to be less intense than their CME-driven counterparts due the oscillatory nature of the z component of the magnetic field they contain (*Tsurutani et al.* 1995), cause more severe spacecraft charging (*Denton et al.* 2006), cause weaker perturbations in Dst, distort the Earth's magnetic dipole less (*Borovsky and Denton* 2006) and tend to be longer-lived, lasting up to 5 days and beyond (*Chen et al.* 2014).

While CIR-driven storms are not as intense as CME-driven storms (and may be recurrent do to their connection to the ∼27-day solar rotation), they are more efficient in transferring energy to the Earth's magnetosphere (*Turner et al.* 2009), and they last much longer (from several days to even weeks), resulting in much greater satellite orbit decays than are caused by CME-driven storms (*Gonzalez et al.* 1999 and *Chen et al.* 2012).

The geomagnetic impact of magnetic storms can partially captured using the Dst

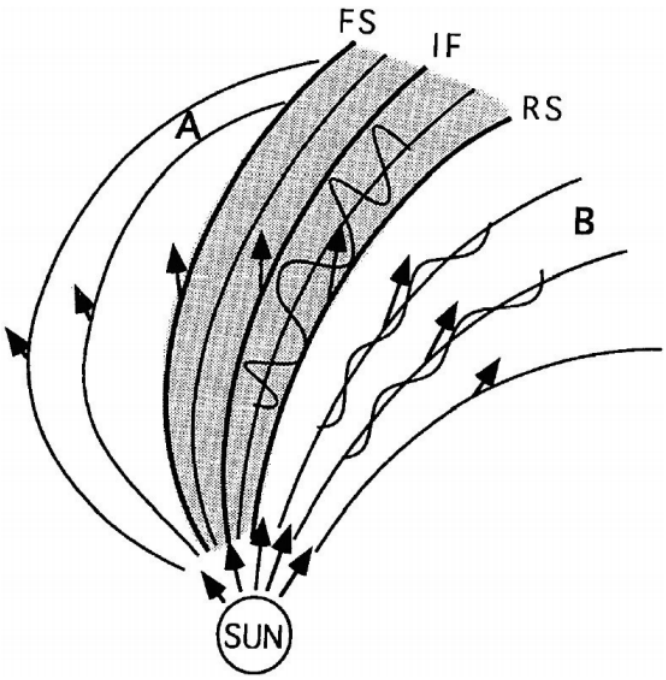

Figure 1.5: A schematic of a CIR: Region A corresponds to the slow solar wind, region B the fast solar wind, the shaded region the CIR, FS the foreward shock, IF the interface region, and RS the reverse shock (*Tsurutani et al.* 2005).

index, a measurement of the strength of the ring current around the Earth that produces a magnetic field that opposes the Earth's magnetic field (*Carovillano and Siscoe* 1973). The Dst index is derived from a network of near-equatorial geomagnetic observatories, is measured hourly, and will be increasingly negative for elevated levels of geomagnetic activity. Dst is one of several geomagnetic indices used to describe variations in the terrestrial magnetic field. Others include the K_p and a_p indices. The former of these is a 3-hour-range index on a 0-9 scale that is the mean of the 3-hourly range in magnetic activity relative to an assumed quiet day curve collected from 13 geomagnetic observatories between 44° and 60° northern or southern geomagnetic latitude (*Bartels et al.* 1939 and *Bartels* 1949). The a_p index is derived from the Kp index, and ranges from 0-400 (*Bartels and Veldkamp* 1954).

Geomagnetic storms are mainly characterized by a decrease in the horizontal component of the geomagnetic field, and are typically characterized by three distinct

phases (Figure 1.6), which can be identified by certain behavior in the Dst index (*Jordanova et al.* 2020):

1. Initial Phase - Storm Sudden Commencement (SSC)

   A sudden impulse coinciding with the arrival of the interplanetary shock structure at the Earth's magnetosphere. Dst typically will rise to near positive of positive values.

2. Main Phase

   Enhancement of the ring current occurs due to particle energization and trapping. Dst will rapidly increase in intensity to a minimum.

3. Recovery Phase

   A gradual return to normal conditions due to various loss processes. Dst will return to a quiet time value over a period of several days.

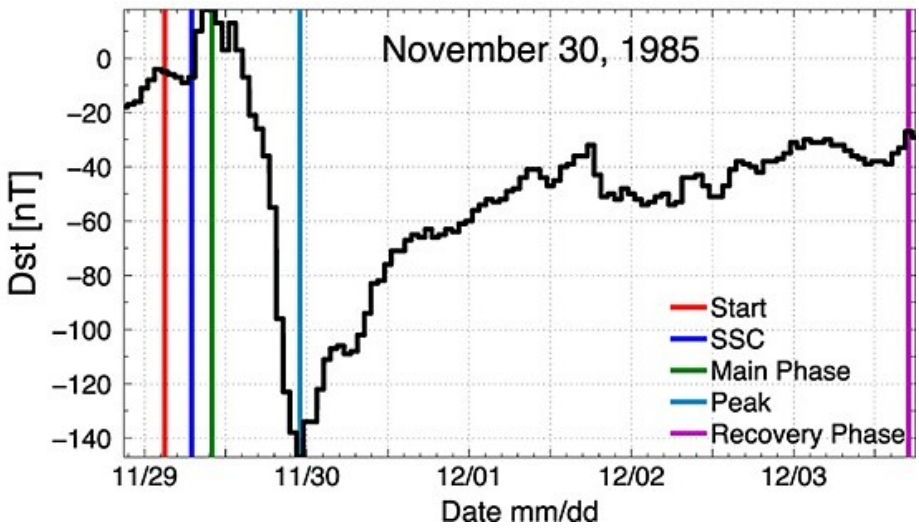

Figure 1.6: Dst during different phases of a geomagnetic storm.

Geomagnetic storms can be classified according to their intensity, which is characterized by Dst. Generally, a storm is classified as moderate for $-50\text{nT} > \text{DST}_{\text{min}} > -100\text{nT}$, as intense for $-100\text{nT} > \text{DST}_{\text{min}} > -250\text{nT}$, and as a superstorm for

$\mathrm{DST}_{\mathrm{min}} < -250\mathrm{nT}$ (*Cid et al.* 2013a and *Waheed et al.* 2019). For severe enough storms, electrical currents induced on the Earth's surface can cause life-threatening power outages and pipelines can be corroded. The surges in local density at altitude can cause loss of satellites in LEO, can cause satellites to become damaged through extensive spacecraft charging, satellite communication failures can occur, and navigational problems can result. The space weather community has therefore a vested interest in studying the density response of the thermosphere to geomagnetic storms, and the efforts to achieve this end are outlined in the next section.

1.1.3 Characterization of Storm Time Neutral Densities

The thermospheric density response to geomagnetic storms has been the subject of investigation for several decades. The earliest methods used to obtain knowledge about the structure and variation of the thermosphere came chiefly from two sources: (1) Sounding rockets that released vapor clouds or were equipped with mass spectrometers, and (2) analysis of the the perturbations of satellite orbits, which dominated efforts to characterize the density, beginning in 1958 (*Priester et al.* 1967). Sounding rockets saw extensive use in the 1960s and 1970s, and while they are not currently the primary method for studying the thermospheric density today, they are valued for their ability to study the lower thermosphere (between ∼90-200 km), since drag data at those altitudes is scarce, and for this reason, they are still occasionally employed (*Kurihara et al.* 2006, *Chern et al.* 2012, and *Vadas and Crowley* 2017). Many of the first satellites used to study the thermosphere were equipped with pressure gauges (*Mikhnevich et al.* 1959), but these tended to severely underestimate the densities (compared to those derived from concurrent drag data) by roughly a factor of 2 (*Newton et al.* 1965). Satellites equipped with mass spectrometers, like the pioneering *OGO*-6 satellite, saw use beginning in the late 1960s (*Nisbet et al.* 1977), though many of these satellites saw extensive technical difficulties.

At present, accelerometers on LEO satellites are routinely used to derive the thermospheric density from extremely precise measurements of non-gravitational accelerations experienced by the host satellite (*Sutton et al.* 2007, *Bruinsma et al.* 2004, and *Doornbos et al.* 2010). The level of accuracy achievable of these accelerometers is up to 10^{-9} m/s^2 for the STAR accelerometer aboard the CHAMP satellite, 10^{-10} m/s^2 for the SuperSTAR instrument aboard the GRACE satellites, and 10^{-12} m/s^2 for the GRADIO instrument aboard GOCE (*Flury et al.* 2008, *Rodrigues et al.* 2003, *Touboul* 2003a, and *Touboul et al.* 2004). The Swarm spacecraft represents the most recent of these spacecrafts to join the fold (*Siemes et al.* 2016). Given that not all thermospheric satellites are equipped with such sensitive and expensive accelerometers, and that occasionally, those spacecraft carrying them suffer from equipment malfunctions, a technique termed POD is sometimes employed. This technique involves using GPS tracking information for a satellite or Satellite Laser Ranging (SLR) signals reflected off of satellite, and performing a summation at every time step of all of the forces acting a spacecraft, and integrating equations of motion to determine the exact position of an orbiting satellite where a measurement is taken (*Hough* 2012 and *Jäggi and Arnold* 2017). The technique has not only been used to derive densities from spacecraft orbits, but also has been used to calibrate and validate the aforementioned accelerometers (*Visser and IJssel* 2016). Densities derived using POD tend to correspond extremely well with accelerometer-derived densities (Figure 1.7) over a variety of latitudes (*Yuan et al.* 2019), though the error between them can approach 10% during low density periods (*Calabia and Jin* 2017). Data assimilation techniques have also been devised that take advantage of GPS tracking of several small satellites within a constellation to develop accurate density timeseries that capture minor and moderate fluctuations in geomagnetic activity (*Sutton et al.* 2021). Orbit-propagation also can be used as a tool to derive thermospheric densities along a spacecraft trajectory, specifically by correcting density predictions from a model by

optimizing the orbit fitting of modeled trajectories with observations under different density conditions (*Bussy-Virat and Ridley* 2021).

A TLE from a spacecraft may also be used to derive the thermospheric density. A TLE is a data format which encodes orbital elements of an Earth-orbiting object at a specific point in time, referred to as its epoch. The mean motion encoded by in the TLE is particularly important, as it is the angular speed required for the object to complete a single orbit. TLE data is specific to a set of simplified perturbation models which are used to derive orbital state vectors (vectors of position and velocity) of satellites and space debris relative to the Earth-centered inertial coordinate system. These models are collectively referred to as SGP4 (*Vallada and Crawford* 2008). In the drag equation (Eq. 1.3), dividing both sides by the satellite mass yields the inverse ballistic coefficient $B = \frac{C_D A}{m}$, which when divided by a reference air density $\rho_0 = 1.00136798 \times 10^6$ kg m^{-3} and a factor of 2, yields the quantity $B^* = \frac{\rho_0 B}{2}$. This quantity is reported in a TLE, which contains orbital elements for a spacecraft for a given point in time. For LEO objects for which the inverse ballistic coefficient is known, the density can then be found from the TLEs by determining the magnitude of the solar radiation pressure relative to thermospheric drag, integrating a modified differential equation of the mean motion between TLE epochs, using SGP4 to integrate the product of the wind factor (representing the effect of wind on the drag acceleration) (*King-Hele* 1987) and cubed velocity, and taking the ratio of the two integrated equations. This process is explained in detail in *Picone et al.* 2005a. Due to the fact that drag coefficients are the greatest uncertainty in the dynamics of LEO satellites (*McLaughlin et al.* 2011), the fact that TLEs are computed over an entire orbit and thus smooth out density perturbations that occur over the entire orbit (*Vallado et al.* 2006), and the fact that TLEs are low-resolution, being reported at best once-per-day and often suffering from outages, TLE-derived densities are seldom used to study thermospheric densities during storms.

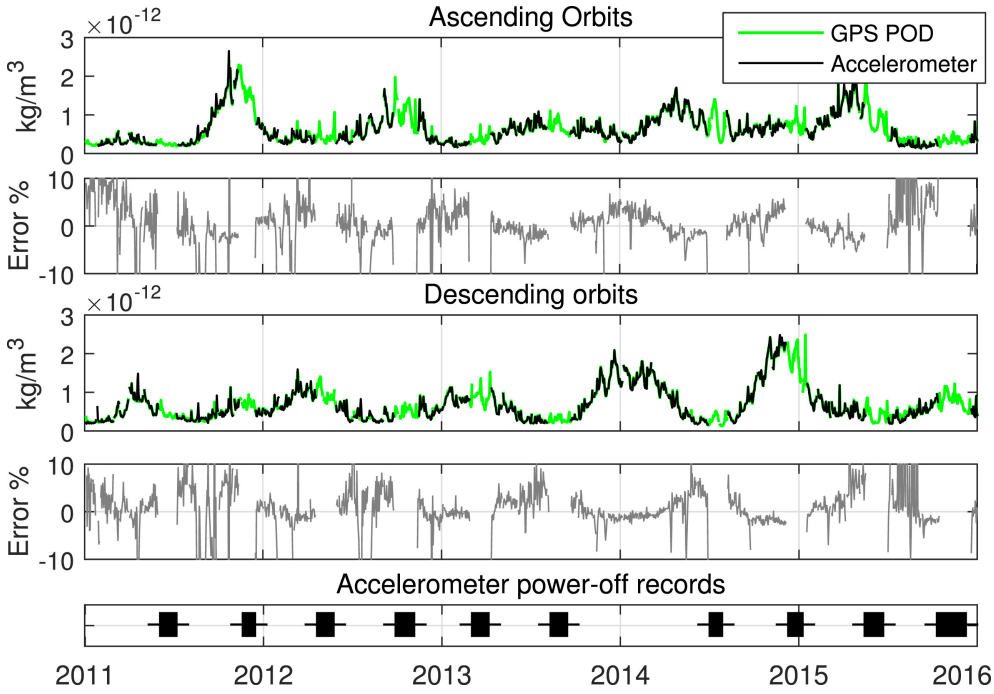

Figure 1.7: GRACE POD and accelerometer densities between 2011 and 2016 (*Calabia and Jin* 2017).

Accelerometer-derived densities have been analyzed during a variety of geomagnetic storms, most prominently using data from the CHAMP satellite, which orbited at an altitude of ∼400 km, and from the GRACE satellites, which orbited at ∼450 km (Figure 1.8). These accelerometer data consistently show that densities at LEO altitudes can be enhanced to between 200%-400% of their quiet time values during the main phase of a storm (*Lei et al.* 2010), and this can approach nearly 800% for severe storms (*Bruinsma et al.* 2006). Additionally, the density response to thermospheric energy influx is rapid at high latitudes, with enhancements routinely occurring within 1-2 hours of SSC, with it being more intense and immediate on the dayside - enhancements on the nightside can be delayed by between 1-2 hours behind their dayside counterparts (*Sutton et al.* 2009 and *Lühr and Liu* 2006). The most recent literature shows that when zero epoch time of the storm is set as either the time of CME impact or the time when the vertical component of the IMF turns southward, the high-latitude thermosphere may respond with density enhancement as rapidly as

15 minutes (*Oliveira et al.* 2017b). Density enhancements generated at high-latitudes also propagate down to equatorial latitudes as the heat generated by the energy influx redistributes itself global; this can take between 3-5 hours depending on the severity of the storm (*Lathuillére and Menville* 2010).

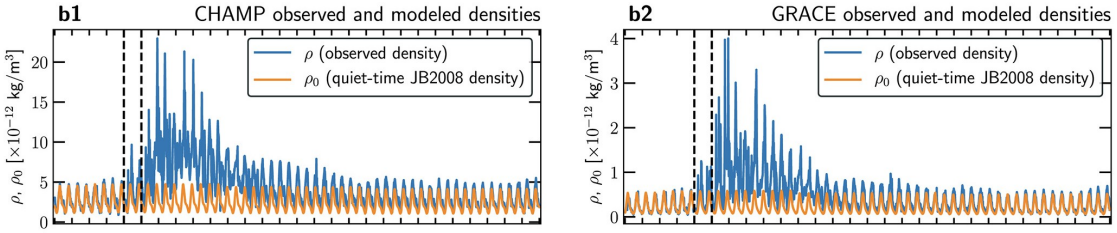

Figure 1.8: CHAMP (left, in blue) and GRACE (right, in blue) storm time densities both compared to outputs from an atmospheric model (in orange) (*Oliveira and Zesta* 2019).

The Traveling Atmospheric Disturbance (TAD) is an important mechanism by which density enhancements are propagated during atmospheric heating. During a geomagnetic storm, the Dungey cycle escalates, causing the ion flow and aurorae to intensify, driving up ion densities in the polar regions. This increases frictional (Joule) heating between the ions and the neutrals, which heats up the high latitudes dramatically, driving TADs, which are longitudinally extended wave fronts that propagate away from a heated source region, dispersing energy globally over a period of hours (*Richmond and Matsushita* 1975). During the day, TADs are thought to deposit most of their energy relatively close to the high-latitude source through Joule heating spurned by collisions between the bulk motions of ions and neutral air (*Rishbeth* 1979), while at night, TADs propagate beyond the equator before being dissipated (*Sutton et al.* 2009 and *Forbes et al.* 2005). TADs often propagate at the local speed of sound, ranging from ∼200-300 m/s below 250 km to 500-800 m/s above 300 km (*Bruinsma and Forbes* 2007). Small-to-medium-scale TADs (less than 1000 km in extent) tend to be confined to the mid and high-latitudes, dissipating well above the tropics (*Bruinsma and Forbes* 2008 and *Mayr et al.* 1990), whereas as it is the large-

scale TADs that propagate to the equator and often far into the opposite hemisphere, if their scale is at least ∼2600 km (*Bruinsma and Forbes* 2009).

After TADs have redistributed the energy globally, the thermospheric density and temperature can recover in as little time as 6-8 hours (*Sheng et al.* 2017 and *Lei et al.* 2011) or as long as 12-15 hours, depending on the severity of the storm, with longer recovery times extending up to a full day in the lower thermosphere (*Maeda et al.* 1992). Dst has been hypothesized to decay like a hyperbolic function of the form

$$Dst(t) = \frac{Dst_0}{1 + \frac{t}{\tau_h}} \tag{1.4}$$

where Dst_0 is the minimum Dst value, representing the intensity of the storm and the value of Dst when recovery begins, t is the time since recovery, and τ_h is the recovery time - the time it takes for Dst to reach a value of $Dst_0/2$. However, in reality, the length of the recovery phase is highly variable, with the decay happening within several hours (*Yermolaev et al.* 2014) up to several days (*Cid et al.* 2013b, *Hamilton et al.* 1988).

While significant density enhancements represent a major means by which incoming energy affects the dynamics of the thermosphere, winds in the thermosphere also play an important role in the global redistribution of heat and momentum. The next section explores thermospheric winds and how they are measured.

1.1.4 Thermospheric Winds

Winds in the thermosphere are driven by four factors: (1) Gradients in pressure, (2) the Coriolis force, (3) viscosity, and (4), ion drag (*Roble* 2003, *Wang et al.* 2008, and *Tsuda et al.* 2007). They are commonly described in terms of zonal flow (along latitudinal lines, or in the west-east direction) and meridional flow (along longitudinal lines, or in the north-south direction). Heating at high latitudes drives a global wind surge driven by the gradient in pressure from the newly-heated polar regions

to the still relatively cool equatorial regions. This wind surge propagates from both polar regions to low latitudes and into the opposite hemisphere (*Fuller-Rowell et al.* 1994 and *Haaser et al.* 2013). Upward motion in the thermosphere is typically accompanied by horizontal divergence of air higher in the thermosphere, and horizontal convergence of air lower in the thermosphere, with the vertical velocity being inversely proportional to the density, and directly proportional to the pressure gradient (*Rishbeth and Müller-Wodarg* 1999). There exist several methods to measure the winds in the thermosphere.

There is well-established precedent for usage of the device known as an Fabry Perot Interferometer (FPI) to measure thermospheric winds. FPIs, which are operated from the ground, are high-resolution spectrometers that monitor the wind-induced Doppler shift in light emitted by atmospheric atoms such as O and molecules such as OH (*Conde et al.* 2001 and *Xu et al.* 2019). They have also been placed on spacecraft such as Dynamics Explorer, Upper Atmospheric Research Satellite (UARS), and Thermosphere-Ionosphere-Mesosphere Energetics and Dynamics (TIMED) (*Killeen et al.* 1982, *Shepherd et al.* 1993, and *Killeen et al.* 2006). While FPIs are useful tools for capturing neutral wind velocity and temperature in the thermosphere, they suffer from limited ability to estimate the global wind distribution due to a restricted field-of-view and sparse spatial distribution of measurement stations, the limitation of only being able to take measurements during nighttime clear-sky conditions, difficulty in interpreting the connection between temperature enhancements and vertical winds, and establishing a clear baseline to the Doppler shift measurements (*Wescott et al.* 2006 and *Ishii et al.* 2001).

Satellites also have proven quite capable of taking *in-situ* thermospheric wind measurements. The Wind and Temperature Spectrometer (WATS) aboard the Dynamics Explorer 2 satellite obtained vertical and horizontal (perpendicular to the spacecraft track) neutral wind and temperature measurements. by measuring concentration, ki-

netic temperature and motion of the neutral particles, principally with its quadrupole mass spectrometer (*Spencer et al.* 1981 and *Innis and Conde* 2002a).

Incoherent Scatter Radar (ISR) observations may also be used to obtain thermospheric wind observations. The radar at Millstone Hill in Westford, MA, for example can measure the full velocity vector of ions throughout a vertical slice of the ionosphere. The plasma velocities are decomposed into components parallel and orthogonal to the geomagnetic field, and the electric field vector is computed from the orthogonal component, which is completely dependent on $\vec{E} \times \vec{B}$ plasma motion according to the following relation:

$$\vec{v}_E = \frac{\vec{E} \times \vec{B}}{B^2} \tag{1.5}$$

where $\vec{v}_E$ is the plasma velocity, $\vec{E}$ is the uniform electric field and $\vec{B}$ is the magnetic field. The plasma velocities at lower altitudes ($\sim$150 km) and up to the F-region peak ($\sim$220 km) depend on both electric fields and neutral winds in a relative amount according to the ratio of the ion gyrofrequency (the angular frequency of the circular motion of the ions in the local geomagnetic field) to the ion-neutral collision frequency (rate of collision between ions and neutrals), making it possible to calculate the neutral winds by mapping high-altitude electric fields to low-altitude and modeling the collision and gyro frequencies (*Salah and Goncharenko* 2001, *Salah et al.* 1991, and *Goncharenko and Salah* 1998). This method, however, depends on knowledge of the neutral densities in order to compute the ion-neutral collision frequencies; any uncertainties in density estimates, whether from various observation techniques or atmospheric models, thus translate into errors in wind measurements. Additionally, this method relies on low-altitude electron densities being high enough to provide measurable radar echoes, and high signal-to-noise levels, and these are only possible during the daytime, resulting in data gaps (*Zhou et al.* 1997).

Ionosondes represent another means by which thermospheric wind observations

may be made (Figure 1.9). An ionosonde is an HF radar that the HF frequency range, emitting short pulses into the ionosphere. These pulses are reflected by the various layers of the ionosphere, with their echoes being received by the ionosonde's receiver. This allows remote sensing of the plasma frequency, which thus allows one to infer the plasma density via the Bohm-Gross dispersion relation (*Bellan* 2006):

$$\omega^2 = \omega_{\mathrm{pe}}^2 + \frac{3k_{\mathrm{B}}T_{\mathrm{e}}}{m_{\mathrm{e}}}k^2$$
$$\omega_{\mathrm{pe}} = \sqrt{\frac{n_{\mathrm{e}}e^2}{m^*\epsilon_0}} \tag{1.6}$$

where ω is the frequency of the charge oscillation, ω_{pe} is the plasma frequency, k_{B} is the Boltzmann Constant, T_{e} is the electron temperature, m_{e} is the electron mass, k is the wavenumber, n_{e} is the electron number density, e is the electric charge, m^* is the effective electron mass, and ϵ_0 is the permittivity of free space. Given that there is a relationship between the height of the F_2-region and the component of the neutral wind parallel to the magnetic field of the Earth (*Rishbeth* 1972), the meridional neutral wind can therefore be deduced from measurements of the height of the F_2-region peak electron density (*Miller et al.* 1986 and *Richards* 1991). This is outlined in detail in Section 3 of *Kim et al.* 2019.

While there are many different techniques for obtaining neutral wind measurements, accelerometer-derived measurements are relatively new due to the unprecedented accuracy of recently-developed accelerometers and the number of satellites launched with these instruments on them, though one problem with accelerometer-based measurements is that only the cross-track velocity can be obtained. With these measurements of storm-time thermospheric densities prompting deeper investigation into the physics underlying storm-time thermosphere dynamics and thermospheric wind measurements being increasingly collected from LEO satellites, the space

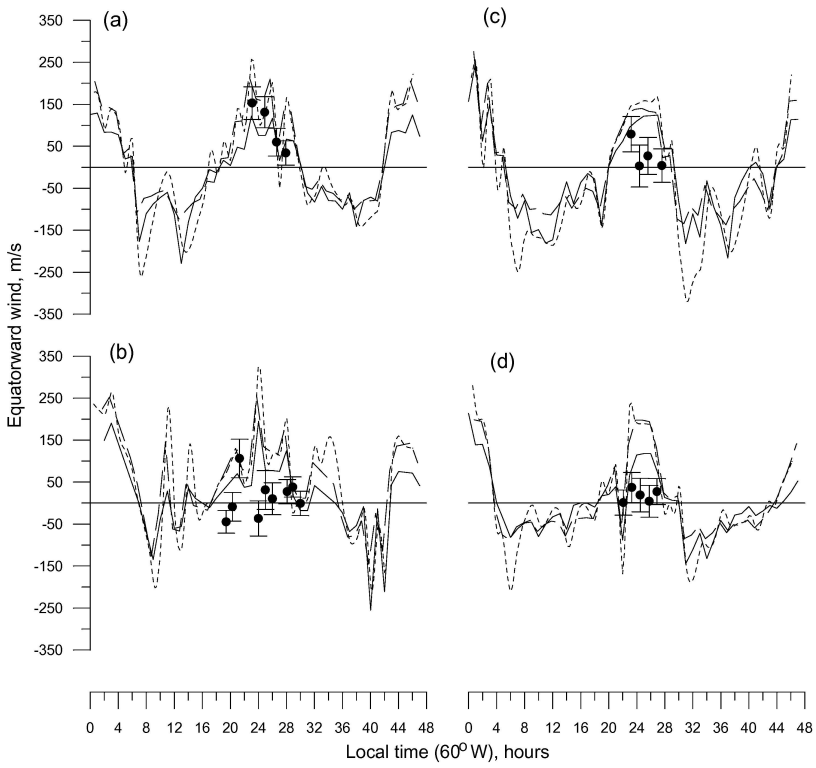

Figure 1.9: Ionosonde wind data processed using three different methods (full, dashed, and dotted lines) in (a) April, (b) June, and (c, d) September in Antarctica (*Foppiano et al.* 2016).

weather community has in response spurned the development of atmospheric models. The next section explores the development of these models, the types of models, and current challenges of storm-time density modeling and global neutral wind modeling.

1.2 Thermospheric Modeling and its Challenges

1.2.1 History of Thermospheric Modeling

Thermospheric models generally fall into two classes: (1) Empirical and (2) physics-based. The former are created by fitting a set of parametric equations to an underlying database of observations. These observations may or may not include ISR data, accelerometer-derived densities from LEO satellites, mass spectrometer data, and more. The parametric equations used differ from model to model, and the accuracy

of each model is thus dependent on the strength of the database and the ability of the parametric equations to reproduce the data for interpolation and extrapolation (*Doornbos* 2012). Physics-based models, in contrast, exclusively rely on a suite of representative equations that are numerically solved to describe changes in temperature, density, and pressure as a function of time, latitude, longitude, altitude, and solar and geomagnetic conditions (*Rees* 1985). The principal equations involved in physics-based models are invariably the continuity, momentum, and energy equations (see section 2.1 in *Ridley et al.* 2006). Physics-based models often are *coupled* by nature, meaning that they are composed of interconnected component models used to describe the geomagnetic field, the ionosphere, thermosphere, and mesosphere, with drivers to run the component models in each region obtained from outputs from the others.

The age of modern thermospheric modeling began with J65 empirical model developed by Luigi Giuseppe Jacchia (*Jacchia* 1965), the first of many models of the Jacchia family. The J65 model represented thermospheric temperature as exponentially increasing asymptotically to the temperature of the exosphere, the outermost layer of the atmosphere. The major database for generating the model consisted of densities determined from measurements of satellite drag, and it originally had a lower boundary of 120 km (*Hedin* 1988). Subsequent updates to the J65 model resulted in the Jacchia-1971 model (*Jacchia* 1971). This was followed by its association with the COSPAR International Reference Atmosphere (CIRA) series of models, most notably the CIRA-1972 model (*Blum et al.* 1972), which extended down to 90 km, and was followed by the Jacchia-1977 model (*Jacchia* 1977), which began incorporating *in-situ* measurements of thermospheric composition.

The advent of increasingly available mass spectrometer data from satellites like *OGO*-6 allowed these models to improve their performance, especially regarding predicting the densities of individual species. Additionally, a method was developed to

derive thermospheric temperatures from ISR observations of the ionosphere (*Nisbet* 1967). The ISR technique involves scattering radar waves off of the electrons in the ionosphere, with the returned power yielding the electron density. Under certain conditions, the neutral temperature can be determined in relation to the heat flow from ions to neutrals (*Marshall and Cully* 2020). This motivated the development of the MSIS family of empirical models, while the models of the Jacchia family would be followed by CIRA-1986 (*Hedin* 1988), Jacchia-2006 (*Bowman et al.*) and culminate in JB-2008, which would incorporate new exospheric temperature equations to represent EUV heating, semiannual density equations based on multiple 81-day average solar indices used to represent semiannual variations in density, and modeling of geomagnetic storm effects using the Dst index (*Bowman et al.* 2008).

The MSIS family of models began with MSIS-77, which incorporated temperature data from three incoherent scatter radars, and mass spectrometer data from five satellites (*Hedin et al.* 1977b and *Hedin et al.* 1977a). Improvements to the model which included variations with longitude and Universal Coordinated Time (UTC), representing the influence of the geomagnetic field on the thermospheric response led to the development of MSISE-83 (*Hedin* 1983) and later MSISE-90, which was extended into the mesosphere and lower atmosphere (*Hedin* 1991). The MSIS-family would culminate in the NRLMSISE-00 model, which incorporated satellite drag data and additional ISR data, and predicts anomalous oxygen above 500 km to improve high-altitude satellite drag estimation (*Picone et al.* 2002).

The DTM family of empirical models represents the third major family of atmospheric models that saw its first version released in 1978 in a version that determined total and partial (He, O, N_2) densities, and temperature relying only on satellite drag data and neutral atmospheric temperatures, but using a more generalized model formulation than the models of the Jacchia family (*Barlier et al.* 1978). DTM-78 was followed by DTM-94 (*Berger et al.* 1998), which incorporated new data for low ac-

tivity from the CACTUS accelerometer aboard the D5B spacecraft (*Beaussier et al.* 1977) and high solar activity from the mass spectrometer aboard the DE-2 spacecraft (*Trinks and von Zahn* 1975). DTM-2000 (*Bruinsma et al.* 2003) followed, removing model bias as a function of solar activity, improving oxygen and helium modeling, improving accuracy of temperature predictions at 120 km, incorporating additional satellite data from the Atmospheric Explorer satellite and CHAMP spacecraft, and usage of the Mg II index (*Heath and Schlesinger* 1986) to represent solar UV and EUV emission intensity. DTM-2009 (*Bruinsma et al.* 2012), DTM-2012 (*Bruinsma* 2013), and DTM-2013 (*Bruinsma* 2015) represent the latest iterations of the models of the DTM family, with the last of these using the F30 index, the solar radiation flux at 30 cm, a newer proxy for solar EUV activity (*de Wit and Bruinsma* 2017), high-resolution CHAMP and GRACE data, and low-altitude GOCE data.

These three empirical models comprise the dominant ones used by both the space weather community and by satellite operators to model neutral densities. NRLMSISE-00 in particular has seen extensive usage and thus has been the subject of much investigation into making various improvements (*Dai et al.* 2020, *Shi et al.* 2015, *Wang* 2010, and *Cheng et al.* 2020). A comparison of the performance of all of these models along the CHAMP and GRACE orbits can be found in Figure 1.10.

A final model of note is the GITM (*Ridley et al.* 2006). GITM is a physics-based, three-dimensional, parallel, spherical, atmospheric model that uses a suite of equations to explicitly solve for the densities of a wide variety of neutral and ion species, in addition to solving for the neutral, ion, and electron temperature, the bulk horizontal neutral winds, vertical velocity of the individual species, and the ion and electron velocities. GITM is unique from many other models in that it allows for non-hydrostatic solutions, granting it greater performance in the high-latitudes. Additionally, GITM can be driven by inputs from other models, making it versatile: it can allow for different models of high-latitude electric fields, auroral particle pre-

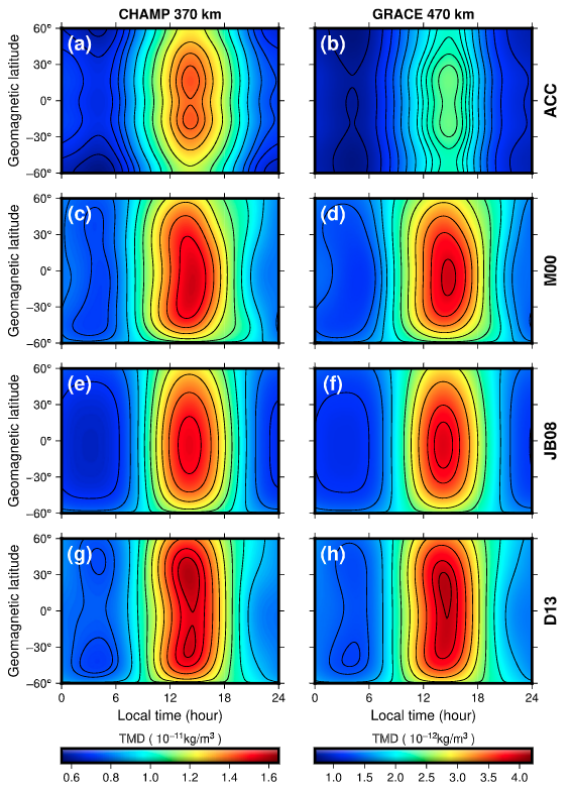

Figure 1.10: Thermospheric mass densities along CHAMP and GRACE derived from accelerometer measurements (ACC) and for NRLMSISE-00, JB-2008, and DTM-2013 (*He et al.* 2018).

cipitation, solar EUV inputs, and particle energy deposition. Among thermospheric models capable of calculating thermospheric winds, GITM shares this capability with Thermosphere-Ionosphere-Electrodynamics General Circulation Model (TIE-GCM), a simulation model of the upper atmosphere that calculates the dynamo effects of thermospheric winds, and uses the resultant electric fields and currents in calculating the neutral and plasma dynamics (*Richmond et al.* 1992). The preeminent empirical thermosphere wind model is Horizontal Wind Model (HWM), a model that describes the atmosphere's wind fields from the terrestrial surface up to ∼450 km and incorporates GOCE wind data and FPI measurements (*Hedin et al.* 1988, *Hedin et al.* 1991, *Drob et al.* 2008, *Emmert et al.* 2008, and *Drob et al.* 2015).

These models have all lead to a number of significant contributions, such as in

advancements in the areas of orbit prediction (*Nicholas et al.* 2000), investigations into the the physics of airglow emissions (*Bag et al.* 2014), probing the behaviors of TADs during geomagnetic storms (*Qian et al.* 2019), and the ionospheric response to the high-speed solar wind (*Pedatella and Forbes* 2011). While these achievements highlight the versatility and usefulness of these models, many of them still suffer from nontrivial shortcomings. These are explored in the next section.

1.2.2 Modeling Challenges

Several studies have demonstrated that regarding the neutral density, while the aforementioned thermospheric models may perform slightly differently at various altitudes and under different conditions (such as during different points of the solar cycle), overall, it can generally be said that no one model is definitively superior to the others (*Akins et al.* 2003, *Pardini and Anselmo* 2000, *Pardini et al.* 2012, and *Shim et al.* 2012). These density models, however, share common limitations that find their origins in several important sources:

1. Indices

   While several of the indices commonly used to drive thermospheric density models, like $F_{10.7}$, K_p, and a_p, have been available for several decades, some newer indices, such as F30 (*de Wit and Bruinsma* 2017), have only been investigated for incorporation into these models in the last decade. Many of the newer indices, such as Mg II (*Viereck et al.* 2001), only are available back to the late 1970s at best and late 1990s at worst, and accompanied by lack of current capacities to use them for prediction. Some indices also do not perfectly capture the phenomena they represent. $F_{10.7}$ for example, is correlated with some parts of the EUV spectrum, but less so with other parts. This means that it can sometimes be a poor proxy for the EUV. The models are therefore limited not only by the availability of the indices, but also are subject to their uncer-

tainties. These uncertainties rise when there are outages in the reporting of an index, and the gaps are smoothed over by linear interpolation of adjacent points (*Vallado and Finkleman* 2014). Additionally, the indices themselves do not perfectly capture the entirety of the physical processes they are proxies for, since they are only correlated with solar and geomagnetic activity. K_p and a_p, for example, diverge at low levels of geomagnetic disturbance, and may register zero values even when solar wind is still penetrating into the magnetosphere and thermosphere (*Moe* 1967). Geomagnetic indices in particular represents fluctuations from an assumed quiet-time curve, subjecting models that rely on them to the accuracy of that curve and being limited to the inability of an index derived from fluctuations to capture total energy input (*Moe and Moe* 2011).

2. Source and Loss Mechanisms

While the importance of Solar EUV radiation in thermospheric heating has been understood for many decades, the importance of energy input from the magnetosphere has continued to be elucidated. During times of low geomagnetic activity, thermospheric density models include too little of the energy contributed by magnetospheric sources, such as the direct flow of shocked solar wind within the magnetosheath to the thermosphere via the dayside cusps (funnel-shaped regions in the geomagnetic field that allow direct injection of solar wind plasma into the atmosphere, resulting in the aurora) (*Heikkila and Winningham* 1971), entry of shocked solar wind plasma from the tail through the polar caps (*Cole* 1966), and wave-particle interactions scattering ring current particles into the atmosphere near the South Atlantic Anomaly, a weak region in the geomagnetic field caused by its non-concentricity (*Domingos et al.* 2017). Energy in the thermosphere is also lost as it is transferred to the mesosphere below, but the fraction of energy ultimately transported is poorly understood. Describing this energy transfer is related to improving understanding in eddy diffusion, a

process by which turbulent mixing is responsible for vertical motion in the atmosphere. Eddy diffusion increasingly dominates atmospheric dynamics at lower altitudes, causing a homogeneous mixture of major atmospheric constituents, while molecular diffusion dominates at higher altitudes, separating constituents depending on their molecular (or atomic) mass. The total vertical flux due to mixing for a neutral gas can be written as the sum of the vertical flux due to eddy diffusion and the vertical flux due to molecular diffusion:

$$\Gamma_{sz}(z) = \Gamma_{\mathrm{E}sz} + \Gamma_{\mathrm{M}sz} \tag{1.7}$$

where the subscript s represents a species and the subscript z signifies the vertical direction. We may further write (*Schunk and Nagy* 2018):

$$\begin{aligned} \Gamma_{\mathrm{E}sz} &= -K_z \left(\frac{\partial n_s}{\partial z} + \frac{n_s \partial T_s}{T \partial z} + \frac{n_s}{H} \right) \\ H &= \frac{kT}{\langle m \rangle g} \end{aligned} \tag{1.8}$$

$$\begin{aligned} \Gamma_{\mathrm{M}sz} &= -D_s \left(\frac{\partial n_s}{\partial z} + \frac{n_s \partial T_s}{T_s \partial z} + \frac{n_s}{H_s} - \frac{1}{kT_s} \sum_{t \neq s} m_s n_s v_{st} u_{tz} \right) \\ H_s &= \frac{kT_s}{m_s g} \end{aligned} \tag{1.9}$$

where subscripts t and s designate different species, v_{st} is the relative speed of the species, u_{tz} is the vertical speed of species t, K_z is the eddy diffusion coefficient, D_s is the molecular diffusion coefficient, k is the Boltzmann Constant, T is the mean temperature, $\langle m \rangle$ is the mean molecular mass, g is the gravitational constant, H is the scale height, and n_s, H_s, T_s, and m_s are the number

density, scale height, temperature, and mass of species s. Historically, thermospheric models have neglected collisions (removing the last term in the first line of Eq. 1.9) and assumed diffusive equilibrium with a fixed lower boundary of the thermosphere by setting $\Gamma_{\mathrm{M}sz} = 0$. Recent studies of atomic oxygen, however, have suggested that this assumption of diffusive equilibrium should not be adopted (*Budzien et al.* 2010). Additionally atomic oxygen behaves differently in response to variations in the value of the eddy diffusion coefficient (*Moe* 1973), and eddy diffusion is also driven by atmospheric gravity waves (*Liu* 2021), and exhibits important seasonal and latitudinal variations (*Danilov and Kalgin* 1992). The inability of thermospheric models to account for these source and loss mechanisms most prominently features itself in the lower thermosphere and when model fidelity is analyzed as a function of season (*Qian et al.* 2009).

3. Drag Coefficients

Since development of density models has historically relied on drag data from satellites, the fidelity of the parametric equations of these models will be contingent on the accuracy of the densities derived from the drag data. This, in turn, means that uncertainties in the drag coefficients of spacecraft will affect the derived densities; these errors are the single largest contribution to uncertainty in orbit determination of satellites (*McLaughlin et al.* 2011) and can cause errors in excess of 15% in the density (*Moe et al.* 2004). Historically, C_D has been assumed to be constant (often at a value of 2.2). Studies in gas-surface interactions have shown, however, that satellite surfaces in LEO are contaminated by adsorption of atomic oxygen. This adsorption raises the energy accommodation coefficient α, defined as follows:

$$\alpha = \frac{E_{\mathrm{i}} - E_{\mathrm{r}}}{E_{\mathrm{i}} - E_{\mathrm{w}}} \tag{1.10}$$

where E_i is the kinetic energy of the incident molecules, E_r is the kinetic energy of the reemitted molecules, and E_w is the energy the reemitted molecules would have had if they had adjusted completely to the surface temperature before reemission (*Pardini et al.* 2010). Given that C_D can be written as a function of α (*Moe and Moe* 2005), the drag coefficient will thus change as a function of altitude and solar and geomagnetic activity.

These limitations of empirical models have lead to their habitual under-performance during geomagnetic storms, during which they generally underestimate the increase in neutral density. Comparisons with accelerometer data from CHAMP and GRACE showed that NRLMSISE-00, for example, only modeled at 200% increase in the density during a storm, compared to a 500% increase as indicated by CHAMP data (Figure 1.11), and additionally predicted the maximum density response in the high winter latitudes and smallest response in the summer polar region, in direct opposite as is indicated by GRACE measurements (*Bruinsma et al.* 2006).

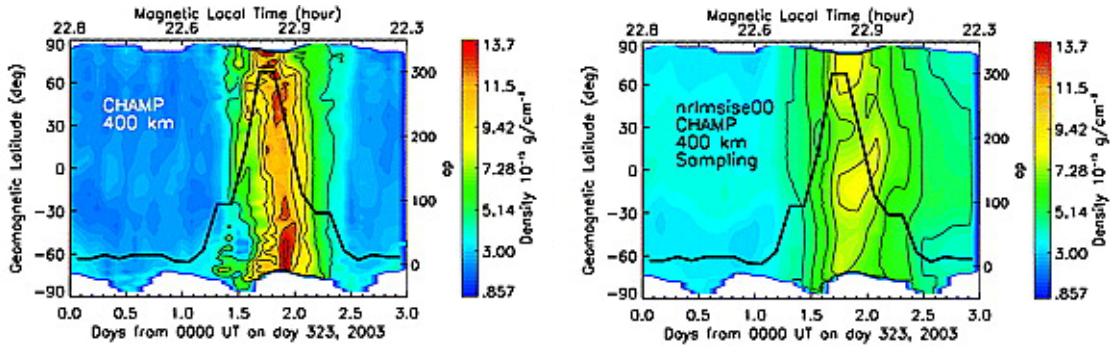

Figure 1.11: CHAMP (left) and NRLMSISE-00 densities (right) during a geomagnetic disturbance *Bruinsma et al.* 2006).

The physics-based models used to study thermospheric winds have also encountered limitations. GITM (*Ridley et al.* 2006) in particular has seen notable success in neutral wind modeling, specifically regarding modeling duskside vortex and anti-sunward polar cap neutral winds that increase with strength as a function of altitude

(*Deng and Ridley* 2006a), investigating how the magnitude and temporal variations of ion drifts affect Joule heating in relation to the vertical wind structure (*Yiğit and Ridley* 2011a), probing the effect of the electric field temporal variability, model resolution, and vertical velocity differences between ion and neutral flows on Joule heating (*Deng and Ridley* 2007), studying the effects of variations of high-latitude Joule and auroral heating with increasing spatial resolution at high latitudes (*Yiğit and Ridley* 2011b), and elucidating the influence of specifications of the electric potential on thermospheric wind patterns (*Liuzzo et al.* 2015b). GITM, however, has encountered difficulties capturing day-to-day variations in thermospheric weather, as represented by the difference between daily observations of the wind and long-term averages at the same Universal Time (UT), and in comparison to FPI data, underestimated magnitude of the weather by 65%, generally smoothing out wind speeds globally more than is seen in measurements (*Harding et al.* 2019). Issues modeling seasonal variations in density in general have also been noted in TIE-GCM, with a remedy arising in imposing seasonal variation of eddy diffusion (*Qian et al.* 2009). Additionally, GITM has demonstrated the difficulty in being used to determine ideal combinations of high-latitude drivers that result in accurate simultaneous replications of both zonal and meridional neutral winds, generally being limited to modeling one or the other for a given event (*Liuzzo et al.* 2015a). GITM's difficulties in this regard manifest not only in difficulties with replicating wind measurements, but also changes in electron density during geomagnetic storms (*Pawlowski et al.* 2008).

The impacts of these modeling challenges reveal important gaps in the current understanding of thermosphere dynamics, specifically in regards to coupling to the magnetosphere and mesosphere, proper descriptions of high-latitude drivers, capturing seasonality effectively, and improving mathematical descriptions of vertical flux. These challenges manifest their severity most intensely during geomagnetic storms, where empirical models in particular are uniquely poorly-equipped, given that their

databases contain data overwhelmingly corresponding to quiet times. These difficulties present significant hindrances to performing orbit prediction for LEO satellites (*He et al.* 2020), which can cause significant differences in the probability of collision of LEO objects (*Bussy-Virat et al.* 2018b), jeopardizing the safety of astronauts, the longevity of important satellite missions, and presenting problems estimating the time and location of reentry for de-orbiting space debris (*Bastida Virgili et al.* 2016). Given the massive amount of space debris in orbit, and the consistent increase in the number of LEO satellites, addressing these challenges is of vital importance, especially to mitigate and avoid disastrous scenarios such as a domino-effect of successive collisions in orbit, known as Kessler Syndrome (*Kessler and Cour-Palais* 1978).

1.2.3 Summary

In this chapter, four major challenges in modeling thermospheric density and wind, particularly during geomagnetic storms, have been explored. First, most thermospheric models are empirical in nature, relying on parametric equations relating global density measurements to observations of solar and geomagnetic indices. These indices do not perfectly capture the physics of energy input into the thermosphere. Secondly, the thermosphere is a complex system to model, being coupled to the lower atmosphere, ionosphere, magnetosphere, solar wind, and the Sun. For both empirical and physics-based models, it is a significant challenge to describe the source and loss mechanisms governing energy exchange between these regions, and thus it is difficult to accurately reproduce the thermospheric density and wind response in a wide variety of situations for which there is limited knowledge regarding the physics of the coupling or the inputs to the coupling systems are poorly understood. Thirdly, the density measurements many of the empirical models rely upon for parametric fits are subject to nontrivial uncertainties due to imperfect modeling of satellite drag coefficients. Fourthly, physics-based models in particular encounter difficulty capturing

weather and seasonal variations in both density and wind, and tend to smooth out features in both globally.

1.3 Contributions of the Thesis

Uncovering and developing workarounds to the shortcomings of thermospheric models is imperative to elucidating the underlying physics of thermosphere dynamics and providing tools for the space community to improve orbit prediction for objects in LEO. To that end, the Multifaceted Optimization Algorithm (MOA) was developed. Empirical thermosphere density models rely chiefly on parametric fits between solar and geomagnetic indices and a compendium of density measurements with contributions from drag-derived densities, FPI measurements, and accelerometer-derived densities from LEO satellites. These models tend to perform poorly during geomagnetic storms, generally underestimating the increase in density, which has major implications for orbit prediction and space situational awareness. Several tools, which are briefly covered in the next chapter, have been developed to address this limitation, but most of them are either computationally expensive, rely on classified satellite tracking information, or rely on high-resolution satellite tracking data that is not always available to the broader space community. The Multifaceted Optimization Algorithm (MOA) therefore was developed as a simple and effective means for achieving respectable storm time density error reduction during geomagnetic storms. MOA is a simple algorithm that relies on the Spacecraft Orbital Characterization Kit (SpOCK), an orbital propagator developed at the University of Michigan (*Bussy-Virat et al.* 2018a). SpOCK can use the NRLMSISE-00 or GITM models to derive the density at the position of the spacecraft. The geometries of the spacecraft simulated in SpOCK can either be made by a user describing the size accommodation coefficient, and orientation of each of the faces of the spacecraft, or they can be supplied by Computer-Aided Design (CAD) files. SpOCK makes use of a decomposition of spherical harmonics for the terrestrial gravitational potential, and includes contributions from solar radiation pressure, lunar gravity, and atmospheric drag. SpOCK is described in detail in *Bussy-Virat* 2017.

MOA computes adjustments to the solar and geomagnetic indices supplied to the NRLMSISE-00 model through use of SpOCK by first obtaining satellite ephemerides in the form of the TLE, which encodes orbital elements for use by Simplified Perturbation Models that can predict spacecraft trajectories, and then it proceeds with three subprocesses: (1) AROPT, which minimizes the orbit error between SpOCK and TLE-derived altitudes by adjusting the cross-sectional area of the simulated spacecraft, (2) FOPT, which minimizes orbit error solely by adjusting $F_{10.7}$, and (3) ap Optimization Subprocess (APOPT), which minimizes orbit error solely by adjusting a_p. The mean adjustments to the indices found throughout the storm across all of the satellites modeled by SpOCK are then applied to NRLMSISE-00 along the orbit of a validation satellite, such as Swarm, for direct comparison of the resulting orbit-averaged densities to those derived from accelerometer data. MOA's component subprocesses are described in detail in Chapter II.

Limitations in physics-based models similarly show difficulty in capturing the physics in the thermosphere. These limitations are further explored in several empirical models in the context of geomagnetic storms in Chapter III. NRLMSISE-00, DTM-2013, and JB-2008 are all evaluated together by comparing their performance across a wide variety of geomagnetic storms using superposed epoch analysis. This form of analysis allows the unveiling of trends and biases in the models that may appear as a function of storm intensity or season. The superposed densities generated by each model are compared to those from CHAMP.

Limitations in GITM are further explored in Chapter IV in the context of horizontal winds, which play an important role in controlling the composition of the thermosphere, driving vertical flux and heat transfer through horizontal convergence at low altitudes and horizontal divergence at high altitudes, and affecting satellite trajectories when applied nonuniformly along the orbit. Specifically, the ability of GITM to capture the behavior of the horizontal winds is studied. Histograms com-

puted from GITM winds are compared to those from winds measured by the GOCE spacecraft to characterize GITM's capacity to reproduce physic the dependencies (or lack thereof) of the horizontal wind on magnetic latitude, geomagnetic activity, and season, as observed in the GOCE data. This analysis is done for GOCE data covering January through October of 2013.

Thermospheric modeling continues to be an important and vital endeavour as the small satellite revolution contributes to the launching of numerous objects into LEO. Whether it is the orbits of these satellites contributing to improvements in density model calibration, or satellite measurements being used to improve the fidelity of physics-based models and reveal consistent patterns in the storm time performance of empirical models, the interdependency between LEO satellites and thermospheric modeling will likely only continue to increase in strength in the future, making improvements in both the success of the models and of satellite missions reliant on improvements in each. In this thesis, MOA is presented as a simple method to use publically-available TLE data to improve storm time empirical model density performance. Additionally, the GITM model is evaluated in its capacity to capture horizontal thermospheric winds in comparison to GOCE data over a 10-month period. Finally, the results of a tri-model storm time superposed epoch analysis of empirical model densities is presented. These endeavors are synthesized to emphasize the significance of the model-satellite relationship, and the advances to science and engineering made feasible by such.

CHAPTER II

Thermospheric Density Model Calibration

The Multifaceted Optimization Algorithm (MOA) is presented. MOA generates new storm-time empirical model densities by computing adjustments to solar and geomagnetic inputs to the NRLMSISE-00 model through three subprocesses. These subprocesses employ use of SpOCK, an orbital propagator developed at the University of Michigan, to minimize the orbit error between SpOCK outputs and TLE-derived altitudes for a number of a satellites, first by determining contributions to change in altitude due to the satellite cross-sectional area, and then by adjusting $F_{10.7}$ and ap. MOA is a simple algorithm that only requires four components to function: satellite TLEs, SpOCK, an empirical model, and solar ($F_{10.7}$) and geomagnetic (a_p) inputs. The algorithm, a demonstration of its capabilities, and validation with Swarm data are presented.

2.1 Introduction

Given that empirical density models exhibit difficulty adequately capturing the thermospheric density response during geomagnetic storms, calibrating these models in order to improve model fidelity has been of ongoing interest. Calibration may be achieved with a variety of methods, most notably with the use of ephemerides from LEO objects. The efficacy of a thermospheric model, and its associated calibrated form, is often characterized by the Root-mean-square (RMS) error, which is of the form:

$$\text{RMSE} = \sqrt{\frac{\sum_{t=1}^{T} (\hat{\rho}_t - \rho_t)}{T}} \tag{2.1}$$

where $\hat{\rho}_t$ and ρ_t are the predicted and modeled densities, respectively, at a given time t, and T is the total number of predictions.

The HASDM, developed by the United States Air Force Space Battlelab, is one such a notable algorithm that calibrates JB-1970 (*Storz et al.* 2005). HASDM's Dynamic Calibration Atmosphere (DCA) solves for the phases and amplitudes of the diurnal and semidiurnal variations of the thermospheric density near real-time from the observed drag effects on ∼75 LEO objects. The DCA uses high-resolution Space Surveillance Network observations directly, and estimates 13 global density correction parameters in 3-hour sub-intervals within a 1.5-day fit span interval for the state of each calibration satellite. The resulting density correction field corrects two local parameters in the vertical temperature profile: (1) an inflection point temperature T_x at 125 km and (2) an exospheric temperature T_∞. This local temperature profile leads to a local density profile through integrating the diffusion equation (Eq. 1.7) and the the hydrostatic equation, which is of the form

$$\frac{\partial p}{\partial z} = -g\rho \tag{2.2}$$

where p is atmospheric pressure, z is altitude, g is the gravitational constant, and rho is atmospheric density. The equations are integrated subject to lower boundary conditions at 90 km altitude. HASDM can predict densities 3 days into the future by using predictions of the geomagnetic indices a_p provided by National Oceanographic and Atmospheric Administration (NOAA), and $E_{10.7}$, an improved solar activity index provided by the SOLAR2000 empirical full solar spectrum model (*Tobiska et al.* 2000). The density correction coefficients from the DCA are predicted 3 days into the future using a prediction filter relating the coefficients to the time series of $E_{10.7}$, 81-day centered mean $E_{10.7}$, and a_p, as well as an extrapolation of the past time series of the coefficients themselves, allowing for a powerful density prediction for use in satellite trajectory prediction. HASDM has shown great success in reducing the RMS error (Eq. 2.1) in the density at epoch by ∼32% and reducing the error for a 1-day prediction in the density by ∼25% on average (*Casali and Barker* 2002).

Doornbos et al. 2008 presented a calibration method that involved the conversion of TLE data to drag data used in the daily adjustment of model calibration parameters. In this method, the atmospheric density is directly calculated from individual TLEs in a process involving several steps that involves estimating satellite inverse ballistic coefficients and integrating differential equations for the mean motion and for the product of cubed velocity and a wind factor (*Picone et al.* 2005b). After these densities have been computed, a set of calibration parameters to the CIRA-1972 atmospheric model (based on those of the Jacchia family) (*Jacchia* 1979) are estimated using a least-squares adjustment in order to minimize the difference between the TLE-derived densities and the model densities. The calibration parameters include height-dependent model density scale factors expanded in a series of spherical harmonics in latitude and local solar time, and spherical harmonic coefficients of temperature corrections to the inflection point temperature at 125 km and exospheric temperature (*Doornbos et al.* 2005). In this way, the calibration is similar

to the DCA of HASDM, excepting that in this case, depending on TLE availability, either 48 or 49 objects were used for calibration. This method has shown success in reducing the RMS error in the density from around 30% to below 16%, with the greatest improvements down to the 5-10% level by estimating more parameters at an additional height level (Fig. 2.1).

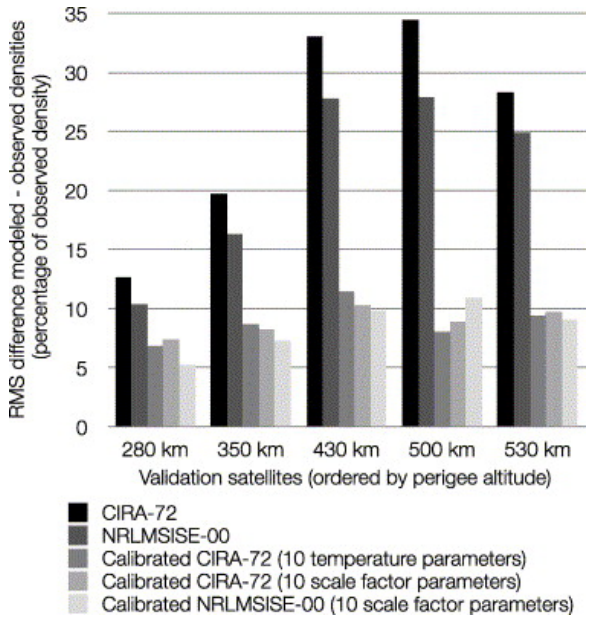

Figure 2.1: *Doornbos et al.* 2008 results showing increased accuracy for CIRA-1972 and NRLMSISE-00.

The Dragster model, developed and presented by *Pilinski et al.* 2016 achieves calibration by modifying the drag effects on spacecraft to minimize orbit error, and uses three-full physics atmospheric models in tandem in an assimilative architecture. Dragster first collects and supplies atmospheric model forcings to a super ensemble of full-physics models that include TIE-GCM (*Richmond et al.* 1992), Thermosphere-Ionosphere-Mesosphere-Electrodynamics General Circulation Model (TIME-GCM) (*Roble and Ridley* 1994a), and Coupled Thermosphere Ionosphere Plasmasphere electrodynamics Model (CTIPe) (*Fuller-Rowell and Rees* 1980 and *Fuller-Rowell*). The model forcings are of two kinds: (1) High Latitude Forcings including but not limited to measurements from ground magnetometers, a_p, K_p, and Dst, and (2) Solar Forc-

ings including but not limited to $F_{10.7}$, measurements from the Extreme Ultraviolet Variability Experiment (EVE) aboard the National Aeronautics and Space Administration (NASA) Solar Dynamics Observatory (SDO) satellite (*Woods et al.* 2012), and Flare Irradiance Spectrum Model (FISM) outputs (*Chamberlin et al.* 2007a). Accelerometer or TLE data, where and when available, is also supplied along with these forcings to the super ensemble of full-physics models, after which an ensemble Kalman filter is applied to estimate geomagnetic forcing parameters and density corrections. Dragster is capable of nowcasting and forecasting densities, and using ∼75 calibration satellites, achieved levels of error reduction roughly on par with HASDM, despite the latter being driven by high-resolution Space Surveillance Network data, and the former TLEs only (Fig. 2.2).

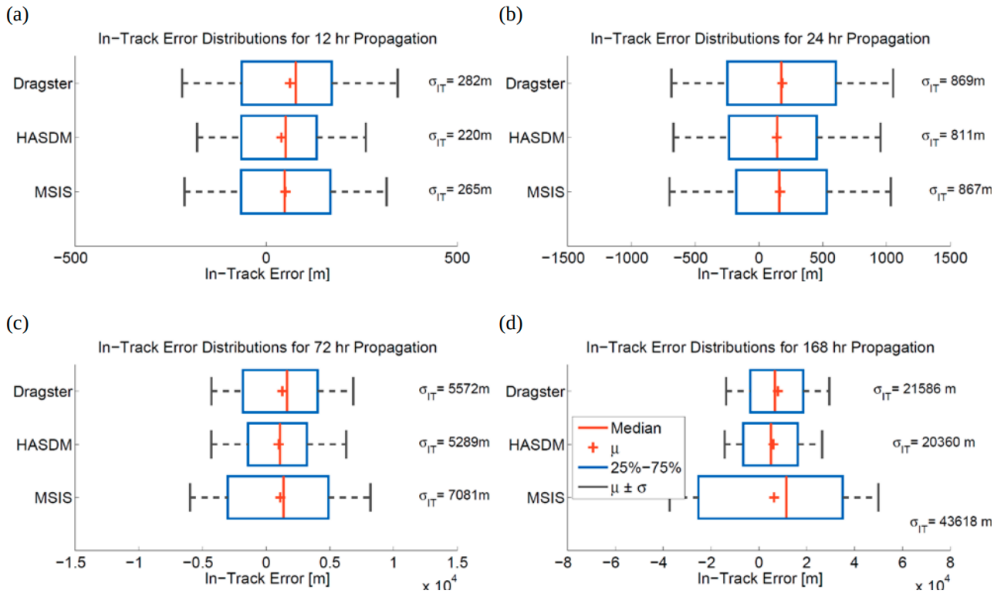

Figure 2.2: Dragster in-track error compared to HASDM and NRLMSISE-00 in-track error for different propagation durations (*Pilinski et al.* 2016).

Model order reduction has also been used to estimate the thermospheric density, receiving particular interest as a way to overcome the high-dimensionality problem of physics-based models (*Mehta and Linares* 2017). A ROM represents a high-dimensional system using a smaller number of parameters. *Gondelach and Linares*

2020 presented a ROM that combines the predictive capabilities of physics-based models with the computational speed of empirical models of estimating the global thermospheric density. This ROM first assimilates nonlinear space weather inputs supplied to NRLMSISE-00, JB-2008, and TIE-GCM, outputs from the aforementioned models for initialization, modified equinoctial elements that express object orbits, TLE data (Keplerian orbital elements), stable ballistic coefficients for each object, and accelerometer densities. After this is done, density training data is generated using any of the aforementioned thermospheric models driven by the assimilated inputs, as well as the accelerometer data and TLE-derived densities, a reduced order is found, the ROM proper is computed by taking snapshots of the density training data and performing Singular Value Decomposition (SVD), Dynamic Mode Decomposition with control (DMDc) is performed for the reduced-order training data (*Proctor et al.* 2016), and the ROM modes are then estimated with a Kalman filter, yielding density predictions. This method is capable of powerful nowcasting and forecasting, and when trained on JB-2008, showed RMS error in orbit-averaged density at $\sim 11\%$ compared to $\sim$17 for uncalibrated JB-2008 for all of 2007 in reference to CHAMP accelerometer-derived densities. It also exhibits impressive performance during geomagnetic storms, outperforming NRLMSISE-00 and JB-2008 throughout the entirety of a storm (Fig. 2.3).

While the aforementioned methods all represent unique and powerful ways of rectifying the limitations of empirical thermosphere models during geomagnetic storms, presented herein is a new method, the Multifaceted Optimization Algorithm (MOA). This method estimates the neutral density by minimizing the orbit error between several modeled spacecraft and a set of TLEs corresponding to each. MOA first estimates a representative cross-sectional area for each spacecraft during the geomagnetically quiet 3 weeks preceding a storm, and then estimates modifications to $F_{10.7}$ and $a_p$inputs to NRLMSISE-00 in order to minimize the RMS error between the mod-

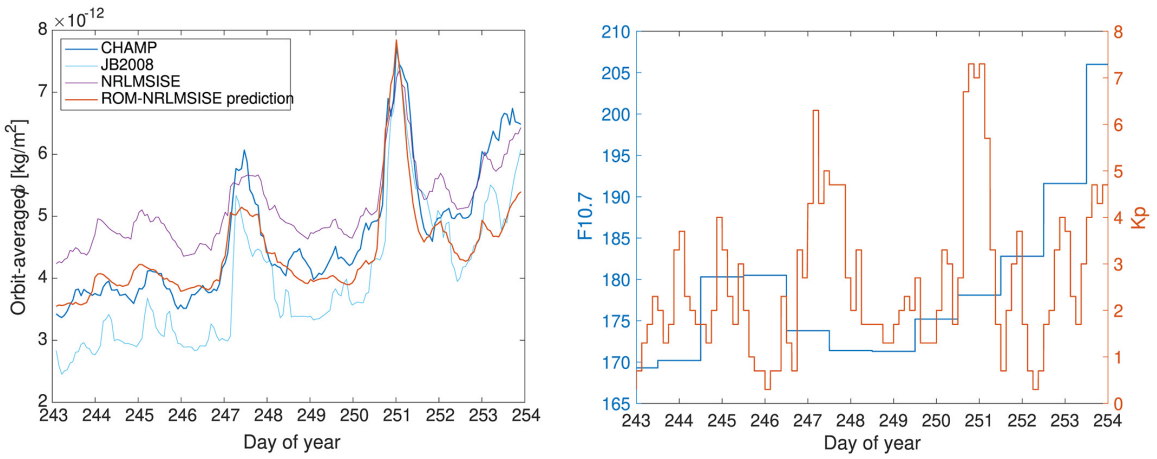

Figure 2.3: *Gondelach and Linares* (2020)'s ROM predicting densities for two geomagnetic storms.

eled and TLE-provided semimajor axis of each spacecraft. The mean values of the adjusted $F_{10.7}$ and $a_p$calculated across all modeled spacecraft are then used to obtain corrected densities by using them to drive NRLMSISE-00.

MOA differs most from HASDM in that the former does not require nearly as many calibration satellites to function, does not solve for a global density correction field in terms of coefficients related to thermospheric temperatures, and does not rely on high temporal and spatial resolution data from the Space Surveillance Network that is classified and inaccessible to the public. MOA differs most from *Doornbos et al.* 2008 in that it does not adjust temperature or scale factors to the density to generate new density estimations, and is not validated by comparing its densities to TLE-derived densities. MOA differs most from *Pilinski et al.* 2016 in that it does not use a Kalman filter, is not assimilative, does not rely on a comprehensive array of high-latitude geomagnetic and solar indices, and doesn't utilize a super ensemble of physics-based models. Lastly, MOA differs from *Gondelach and Linares* 2020 in that it does not involve the creation of a reduced-order model, is not assimilative, and is not predictive. In contrast to every technique mentioned henceforth, MOA is much more simple, and does not involve the calculation of ballistic coefficients for

any of its calibration satellites (as is detailed in *Emmert et al.* 2006), using instead a binary search algorithm to determine each satellite's cross-sectional area before modifying geomagnetic indices. Neither does MOA determine corrected densities by first calculating density ratios and applying them to NRLMSISE-00. Contained herein is a description of MOA, and an overview of its performance, where it is used to compute new densities during the May 2017 geomagnetic storm, using 10 3U CubeSats launched by PlanetLabs, Inc. as calibration satellites. The new densities are computed along the orbits of the Swarm spacecrafts for validation to GPS-derived densities.

2.2 Multifacated Optimization Algorithm

In this section, the structure and functionality of MOA is presented. Sources of data, MOA's different features, and implementation are described.

2.2.1 Methodology

MOA's approach to thermospheric density model calibration lies in the use of orbit propagation as the primary tool. SpOCK is used as the orbit propagator, and driven by TLEs, the primary data source MOA uses. Each of MOA's subprocesses uses SpOCK to estimate the cross-sectional area of modeled spacecraft and adjustments to $F_{10.7}$ and a_p, before corrected model densities are found.

2.2.1.1 SpOCK

SpOCK simulates a satellite's location given a series of inputs that may either be entirely user-supplied or provided by various scientific databases. SpOCK is comprised of a suite of C functions that require the user to supply a geometry file and a main input file. The former describes each face of the spacecraft, including a unit vector describing the orientation, the surface area, the total surface area of any solar cells

on that face, either the drag coefficient or accommodation coefficient, and the solar radiation coefficient. The latter contains an initial position and velocity of the satellite, the name of the geometry file, a description of the spacecraft's attitude, and which forces to include in the dynamics (explained below). SpOCK additionally requires specification of the solar irradiance, which is proxied by $F_{10.7}$, and geomagnetic activity as specified by a_p. Both of these indices are available through either NASA OMNIWeb (https://omniweb.gsfc.nasa.gov/html/omni_source.html#ind) or NOAA's SWPC (ftp://ftp.swpc.noaa.gov/pub/indices/old_indices/), and are used as inputs by NRLMSISE-00 to specify the thermospheric mass density. OMNIWeb gives static daily $F_{10.7}$, and SWPC gives a linear interpolation between daily values of $F_{10.7}$ (Fig. 2.4). MOA defaults to using OMNIWeb as its source for base values of indices.

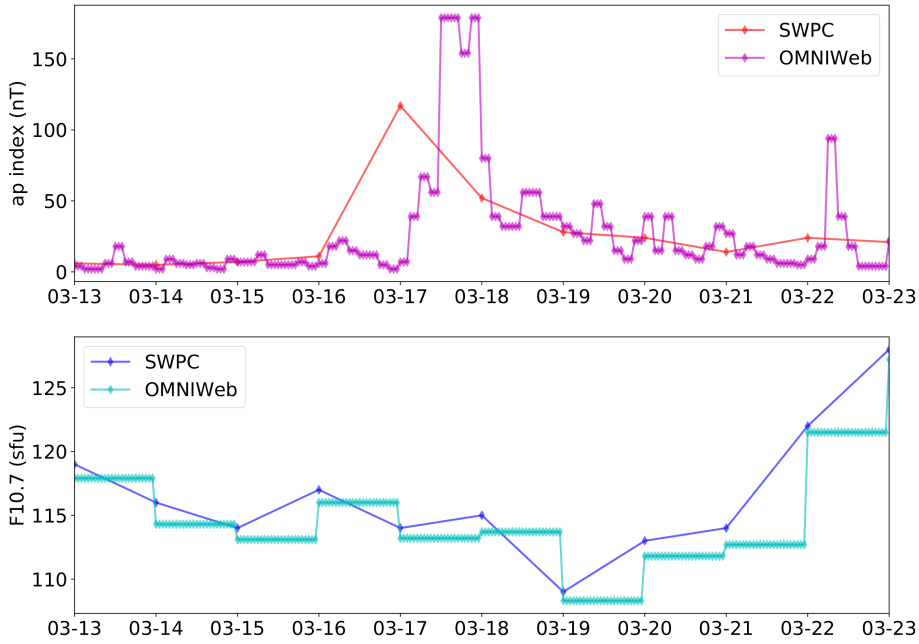

Figure 2.4: OMNIWeb and SWPC a_p(top) and $F_{10.7}$ (bottom) during the 2015 St. Patrick's Day Storm.

As explained in *Bussy-Virat* 2017, SpOCK's dynamic model sums the perturbing forces on the satellite due to four sources. The first of these is gravity, in which the gravitational potential U is decomposed into spherical harmonics to account for the

deviation of Earth from a perfect sphere (*Vallado and McClain* 2007):

$$U = \frac{\mu}{r}\left[1 + \sum_{l=1}^{\infty}\sum_{m=0}^{l}\left(\frac{R_{\otimes}}{r}\right)^{l} P_{l,m}\left[\sin\left(\phi_{gc_{sat}}\right)\right]\left\{C_{l,m}\cos\left(m\lambda_{sat}\right) + S_{l,m}\sin m\lambda_{sat}\right\}\right] \tag{2.3}$$

where r is the distance of the satellite from Earth's center, λ_{sat} and $\phi_{gc_{sat}}$ are the longitude and latitude of the satellite, $P_{l,m}$ and the Legendre functions, $C_{l,m}$ and $S_{l,m}$ are the gravitational coefficients, l and m are the degree and order of the decomposition, and μ and $R_{\otimes}$ are the gravitational parameter ($\mu = 398{,}600.442$ km^{3}s^{-2}) and mean equatorial radius of the Earth (6,378.137 km), as defined in the Word Geodetic System 1984 (WGS84) (*NIMA* 2000). The coefficients $C_{l,m}$ and $S_{l,m}$ are taken from the Earth Gravitational Model 1996 (EGM96) (*Lemoine et al.* 1997).

In SpOCK, as in Equation 1.3 the acceleration due to drag $\mathbf{a}_D$ is computed as:

$$\mathbf{a}_D = -\frac{1}{2}\frac{C_D A}{m}\rho v^2 \frac{\mathbf{v_{rel}}}{v_{rel}} \tag{2.4}$$

where C_D, A, and m are the drag coefficient, cross-sectional area (viewed in the direction the velocity vector), m is the mass of the satellite, and $\mathbf{v_{rel}}$ is the velocity of the satellite relative to the local atmosphere with density ρ. The value of ρ can be supplied by either NRLMSISE-00 or GITM; in MOA, SpOCK is driven by the former.

SpOCK also models gravitational perturbations by a third body, from both the Sun and Moon, written in the following general form:

$$\mathbf{a}_{\gamma} = \mu_{\gamma}\left(\frac{\mathbf{r}_{\alpha,\gamma}}{r^3_{\alpha,\gamma}} - \frac{\mathbf{r}_{\beta,\gamma}}{r^3_{\beta,\gamma}}\right) \tag{2.5}$$

where μ_{γ} is the gravitational parameter of the third body, $\mathbf{r}_{\alpha,\gamma}$ is the vector from the satellite to the third body, and $\mathbf{r}_{\beta,\gamma}$ is the vector from the Earth to the third body.

SpOCK makes use of NASA's SPICE Toolkit (naif.jpl.nasa.gov) to calculate the positions of the Sun and Moon at each time step of the propagation.

Lastly, SpOCK models the solar radiation according to the following (*Wyatt* 1961):

$$\mathbf{a}_{\text{srp}} = -\frac{C_r A}{m}\frac{L_\gamma}{4\pi c r_{\alpha,\gamma}^3}\mathbf{r}_{\alpha,\gamma} \tag{2.6}$$

where A is the cross-sectional area as seen by the Sun, m is the mass of the satellite, C_r is the solar radiation coefficient, L_γ the luminosity of the Sun ($L_\gamma = 3.823 \times 10^{26}$ W), c is the speed of light (c=299,792.458 km/s) and $\mathbf{r}_{\alpha,\gamma}$ the vector from the satellite to the Sun.

Within MOA, each time SpOCK is run, it is initialized with TLEs, rather than the user needing to specify an initial position, and all of the perturbing forces available are applied, along with a degree and order of 20 for the gravitational potential. While selecting a higher degree and order (maximum of 360) grants greater accuracy, these returns generally cease being significant after 20, especially for propagations of short duration, and computation time begins to lengthen considerably. SpOCK contains additional features such as the ability to compute solar power, predict specular points (locations on Earth's surface where signals may be reflected from one satellite to another), simulate ground station coverage, and perform collision risk assessment. These features are detailed in *Bussy-Virat* 2017, and are not used in MOA.

2.2.1.2 MOA Architecture

MOA operates sequentially, beginning by collecting TLEs for a specific satellite for a user-specified interval of time. The first TLE is used to initialize SpOCK. Later semimajor axis predictions from SpOCK are compared to the subsequent TLEs, before the RMS error is calculated in the process of orbit error reduction. In MOA's use of SpOCK, the geometry of each satellite is approximated as a flat plate with an estimated cross-sectional area, and the object's known mass is used. This framework

is used in three subprocesses that use the TLEs for each satellite to obtain corrected model densities (Fig. 2.5).

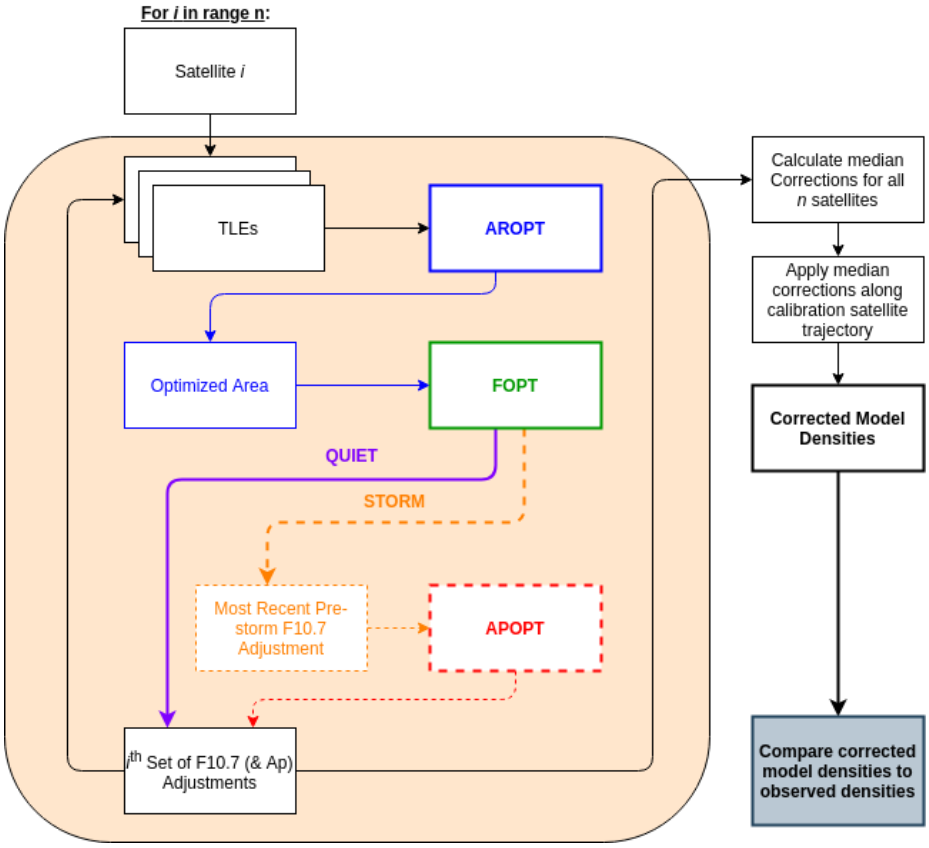

Figure 2.5: A flow-diagram of MOA's processes (*Brandt et al.* 2020).

Area Optimization Algorithm (AROPT)

AROPT is a binary search algorithm that orbits a flat plate for the geomagnetic quiet period of 3 weeks prior to the user-defined time-interval (typically set at the start of a geomagnetic storm), varying the area of the flat plate in each iteration, and thereby searching for the orbit trajectory that best matches the behavior of the altitude specified by the TLEs for the given satellite being simulated. AROPT begins by computing the RMS orbit error for an upper boundary cross-sectional area (A_U), then does for a lower boundary cross-sectional area (A_L), and finally the mean of both (A_M). These initial runs allow AROPT to decide between which two values the optimize area lies (Figure 2.6).

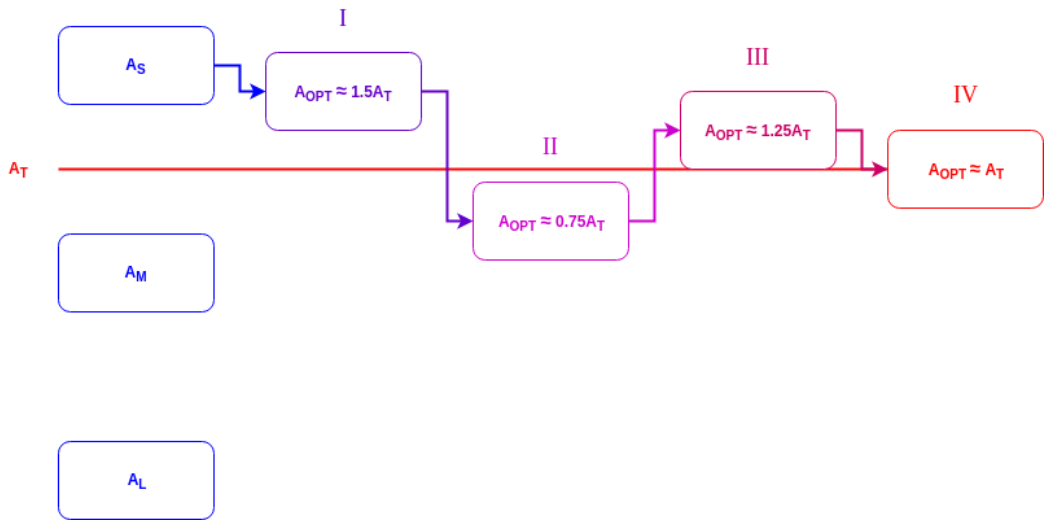

Figure 2.6: A schematic of AROPT's binary search algorithm.

The limits of the area search algorithm are twice the maximum possible projected area of the satellite and half the minimum possible projected area of the satellite, with the projected area estimates obtained not from TLE information but from the user-defined geometry file. Since the ballistic coefficients $B = \left(\frac{C_D A}{m}\right)$ of the satellites are unknown to MOA, and this is crucial to determining density, especially when parsing out influence in the thermosphere due to solar and geomagnetic effects (*Bhatnagar et al.* 2005), AROPT circumvents the difficulty of determining B by iteratively finding a cross-sectional area, with a known mass of the satellite and Drag accommodation derived from a known accommodation coefficient. Schamberg's model of the drag coefficient allows its determination from the accommodation coefficient. In this model, the drag force F_D contributed by molecules incident on an area of the satellite surface dA, at an angle, θ_i, is given by:

$$F_D = \rho v_i^2 dA \sin\theta_i \tag{2.7}$$

where ρ is the local air density and v_i is the velocity of the incident airstream relative to the satellite. The drag force contributed by the molecules reflected from dA is given by:

$$F_D = -\rho v_i dA \sin\theta_i v_r \Phi(\phi_0) \cos(\theta_i + \theta_r) \tag{2.8}$$

where $\Phi(\phi_0)$ takes into account the angular distribution of the reemitted molecules, θ_r is the angle of the reemitted molecules with respect to the satellite surface, and v_r is the velocity of the reemitted molecules, related to the accommodation coefficient, α, by

$$v_r = v_i \left[1 + \alpha \left(\frac{T_w}{T_i - 1}\right)\right]^{1/2} \tag{2.9}$$

where T_w is the temperature of the absolute temperature of the reflected molecules perfectly adjusted to the satellite surface before reemission, and T_i is the absolute temperature of the incident molecules (*Moe et al.*). When substituted into the form of Eq. 1.3, the comprehensive expression of the drag force in terms of α is determined. Integration over the entire satellite surface gives the total drag force on the satellite, but for AROPT, the area is held constant and adjusted at the beginning of each iteration as the orbit error is minimized, and $\theta_i = \pi/2$ since the flat plate is held in perfect incidence to the direction of motion. This yields the resulting expression of the drag force:

$$F_D = \rho v_i^2 A \left\{1 - \Phi(\phi_0) \sin(\theta_r) \left[1 + \alpha \left(\frac{T_W}{T_i - 1}\right)\right]^{1/2}\right\} \tag{2.10}$$

AROPT iteratively finds the optimized cross sectional area (A_{OPT}) over the course of 2 to 3 days of propagation (Fig. 2.7). This does have the caveat of assuming that the projected area is constant over that period of time, but this is permissible for objects that either have attitude control that keeps their cross-sectional area relatively constant (such as a for a nadir-pointing sun-synchronous satellite), or if the behavior of the object is repeating much faster than the minimization time period (such as for a tumbling object).

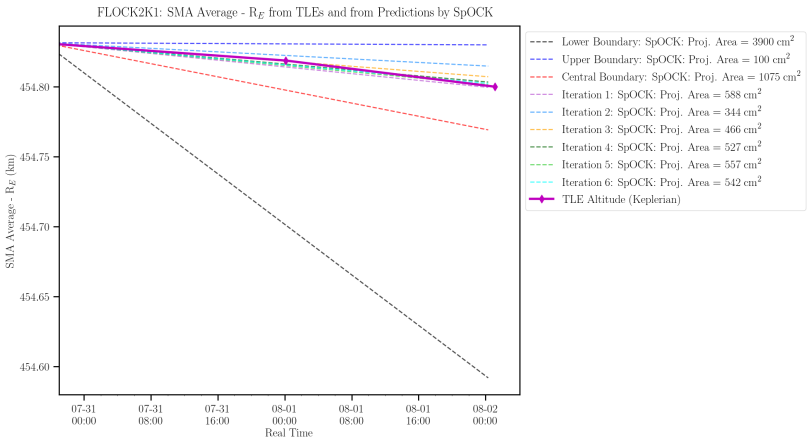

Figure 2.7: AROPT running for the Flock 2K-1 CubeSat.

For objects that systemically change attitude for extended periods of time, this assumption fails. The Cyclone Global Navigation Satellite System (CYGNSS) satellites (*Ruf et al.* 2013), for example, routinely pitch forward in attitude to a high-drag mode for several days to reduce the semimajor axis (*Bussy-Virat et al.* 2019). AROPT's optimization would be most effective during low-drag time and high-drag time, but would not come up with a proper area during the transition. Even though this is a difficulty for AROPT, the method is still able to coarsely show this transition as shown in Fig. 2.8. When pointing nominally, CYGNSS satellites have a projected area of 1,190.35 cm^2, but this increases to ∼7,784.58 cm^2 during high-drag mode. AROPT is able to show the initiation of the high-drag mode on 27-28 July 2017 for CYGFM08, calculating a rise in A_{OPT} to over 6,000 cm^2 during the time of interest. Though this is lower than the true high-drag projected area, it demonstrates that AROPT is capable of approximating changes in area. In addition to that limitation, the areas returned by AROPT preserve the quiet-time bias of the density model SpOCK is using, as those areas correspond to orbit error reduction only for that model.

As AROPT runs for the 3 weeks prior to the geomagnetic storm, it performs optimization in sequential intervals of time, spaced by 1 day, thus creating a time series of optimized areas. It then takes the 75th-percentile of the distribution formed

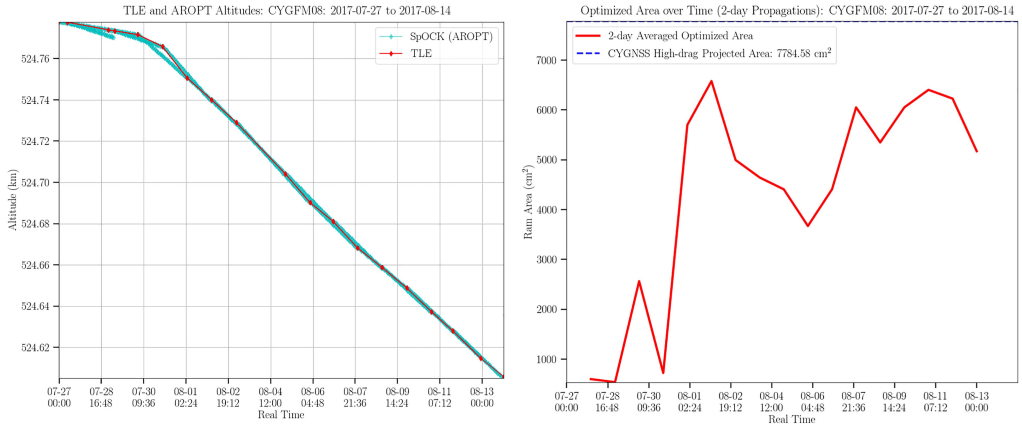

Figure 2.8: AROPT mirroring TLE altitudes for the CYGFM08 CubeSat during one of its high-drag periods (left) with estimates of the projected cross-sectional area (right) (*Brandt et al.* 2020).

from that time series of areas obtained for that satellite, and holds that area constant throughout the remaining subprocesses (Fig. 2.9). The rationale behind the selection of a specific quartile assumes the rate of de-orbit of the satellite in question will mostly attributable to changes in the space environment captured by the behavior of geomagnetic indices. MOA may or may not be set to use other percentiles of the optimized area distribution, but it should be noted that changing this value strongly influences the $F_{10.7}$ and $a_p$adjustments found downstream.

The optimized areas found by AROPT are inextricably tied to the density model SpOCK uses for density estimation, since AROPT's finding of these areas compensates for the bias in that model, though it is important to note that the holding of A_{OPT} constant will contribute to bias in the adjustments to $F_{10.7}$ and $a_p$found by the later subprocesses, since that area will remain unchanged while they are executed. AROPT assumes that during the 3-week quiet time prior to the storm, SpOCK's density model predicts the correct mass density on average; density values at time scales smaller than a couple of weeks may be incorrect. Additionally, this technique assumes that on average, the density model, the TLEs, and the sources of $F_{10.7}$ and $a_p$are unbiased such that the average of each of those errors over the 3-week long

period is minimal. If this is not the case, then the model bias extends into the storm period, with the area bias compensating for the model bias during that time. AROPT is not a tool for high-fidelity geometry modeling, which must be contended with for generating accelerometer-derived densities at high temporal resolution down to several seconds (*Mehta et al.* 2014, *Mehta et al.* 2017, and *Bernstein et al.* 2020), but rather for coarsely removing contributions to changes in spacecraft altitude due to drag only before focusing on contributions from solar and geomagnetic indices. This is a method that can be used for objects that lack CAD models or for objects that are rotating.

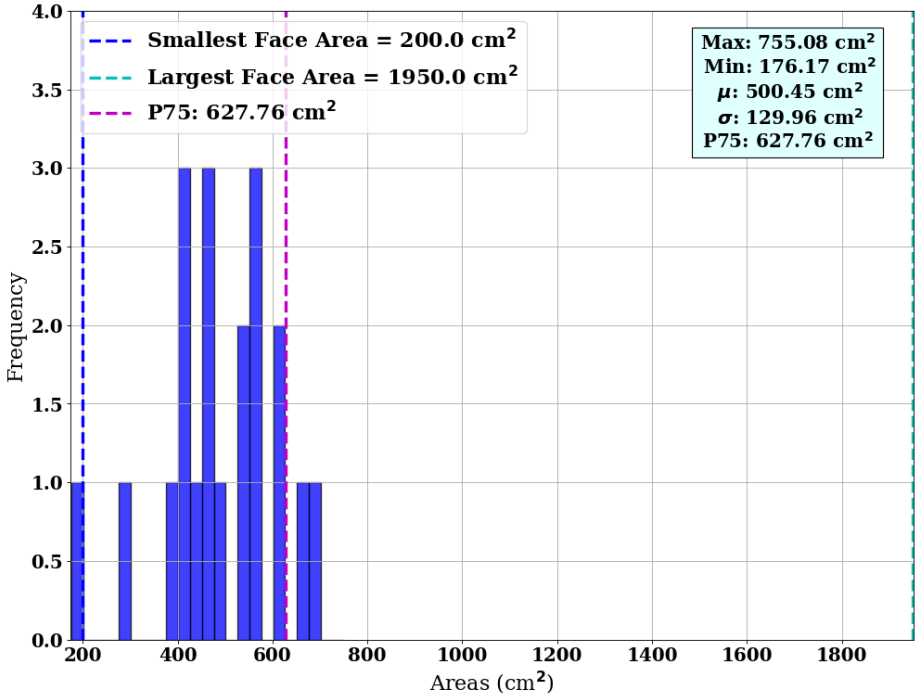

Figure 2.9: An AROPT area distribution for the Flock 2K-1 satellite.

$F_{10.7}$ Optimization Algorithm (FOPT)

The FOPT subprocesses runs immediately after the AROPT subprocesses is complete. It is a binary search algorithm, just as AROPT is, and focuses on adjusting the value of $F_{10.7}$ input to SpOCK's density model in order to minimize RMS orbit error. The upper boundary in FOPT is set to 200 sfu, the standard maximum reference

value in the literature (*Tapping and DeTracey* 1990, *Häusler et al.* 2010, and *Zhou et al.* 2016), while its lower boundary is set to 80% of the value of the minimum $F_{10.7}$ in the interval selected by the user. The lower boundary thus changes as $F_{10.7}$ adjustments are calculated throughout the interval. FOPT runs throughout the entire interval selected by the user, and not just during couple of days surrounding when the minimum Dst of the storm.

a_p Optimization Algorithm (APOPT)

After the FOPT subproccess is complete, MOA determines if APOPT needs to be run. It achieves this by determining if geomagnetic activity is severe enough during the interval to be considered a storm, by determining if Dst (collected from the World Data Center for Geomagnetism (WDCG)) passes below -50 nT (*Akasofu* 2018). If this condition is met, APOPT will run for the 2 days following the initial storm onset. During this time, the $F_{10.7}$ adjustment found by FOPT just prior to the initial storm onset is held constant, as $F_{10.7}$ varies on timescales on the order of days and is reported once per day (*Wang et al.* 2018), compared to a_p, which varies on much shorter timescales on the order of hours (*Wrenn* 1987, *Coffey and Erwin* 2001, and *De Franceschi et al.* 2001). This difference in temporal variation means that any rapid changes in density during the storm will most strongly be related to fluctuations in $a_p$and not nearly at all from $F_{10.7}$.

2.3 Capabilities

In this section, MOA's capacity for storm-time density model calibration is explored with a published example (*Brandt et al.* 2020) corresponding to a geomagnetic storm that occurred between 23 May 2017 and 6 June 2017. For this example case, 10 identical 3U CubeSats in sun-synchronous orbit were used as calibration satellites, and corrected orbit-averaged densities were computed along the orbits of the Swarm-A and Swarm-B spacecrafts, for direct comparison to GPS-derived densities.

Corrections are found corresponding to runs with the 25th, 50th, and 75th percentiles of optimized areas, in order to demonstrate the sensitivity of the corrected densities to the selected percentile, though particular focus is given to results corresponding to the 75th percentile. The average altitudes of Swarm-A and Swarm-B during the time chosen were ∼452 and ∼515 km, respectively, corresponding to a time resolution for the orbit-averaged densities of ∼93.6 and ∼94.9 min for each satellite, respectively.

2.3.1 Storm-time Density Model Calibration

Calibration of the NRLMSISE-00 model between 23 May 2017 and 6 June 2017 follows. During this interval, a geomagnetic storm occurred, reaching peak intensity on 28 May (Fig. 2.3.1).

(a) Dst from the WDCG.

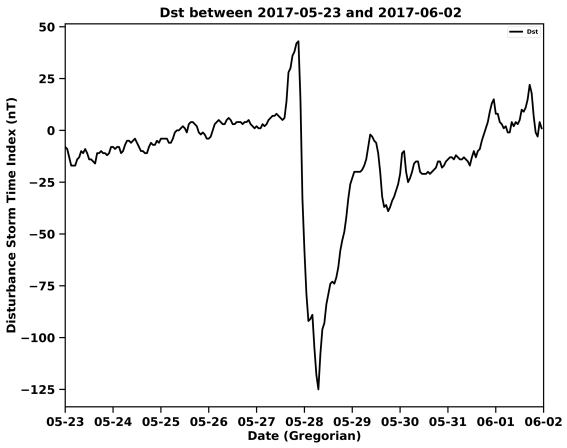

(b) OMNIWeb and SWPC $a_p$and $F_{10.7}$.

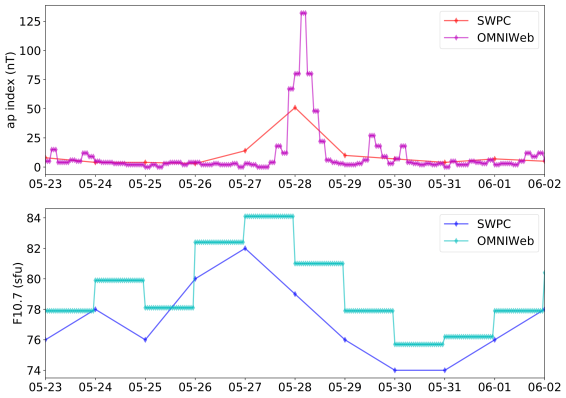

Figure 2.10: Geomagnetic and solar indices between 23 May 2017 and 2 June 2017.

A total of 10 identical 3U CubeSats of the Flock 3P constellation were selected as calibration satellites. These satellites, consisting of 88 total, were designed and manufactured by Planet Labs, Inc., were launched by the Indian Space Research Organization (ISRO) 15 February 2017, and are sun-synchronous and nadir-pointing, orbiting at altitudes between 490 and 500 km. Each satellite has a mass of 5 kg. The satellites are all equipped with a 9-mm diameter telescopic imager capable of

collecting panchromatic, color, and near-infrared imagery at a resolution of up to 3 m. As shown in Fig. 2.11 satellites have extendable solar panels that deploy from opposite sides, resulting in a maximum projected area of 1,950 cm^2 in one plane (*Foster et al.* 2015 and *Safyan* 2015). TLEs from the first 10 of these satellites (Flock 3P-1 through Flock 3P-10) were obtained from Spacetrack, and used by MOA to generate adjustments to solar and geomagnetic model inputs to NRLMSISE-00.

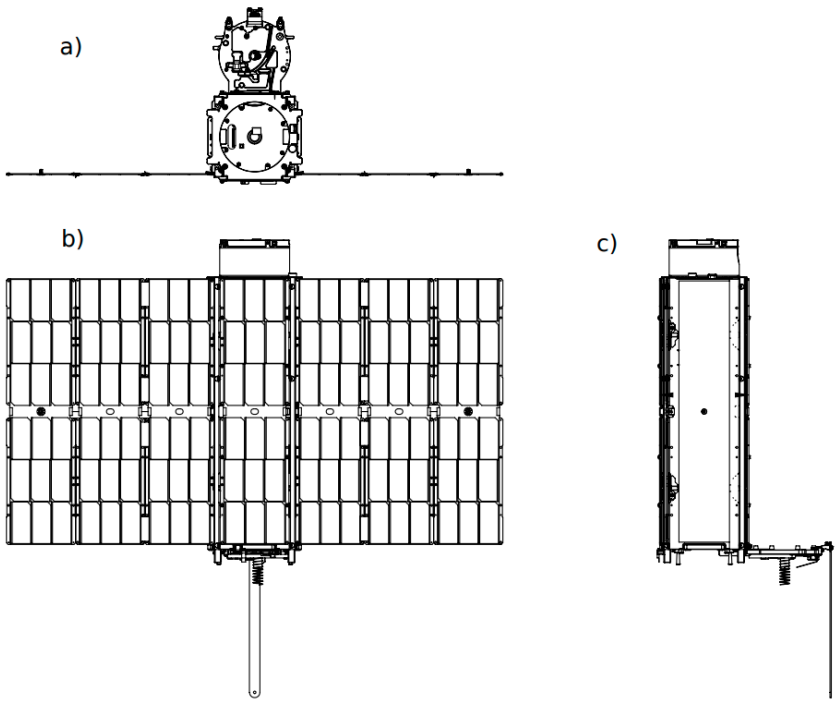

Figure 2.11: Different faces of the Flock 3P CubeSat (*Foster et al.* 2015).

In order to assess MOA's storm-time performance, new models densities computed between 23 May 2017 and 6 June 2017 were compared to GPS-derived densities along the orbits of two of the Swarm spacecrafts. Swarm is a European Space Agency (ESA) mission tasked with the primary mission of studying Earth's magnetic field. It consists of three satellites (A, B, and C), placed in two different orbits: Swarm-A and Swarm-C orbit at ∼450 km in altitude at 87.4° inclination, and Swarm-B at an altitude of ∼530 km at 88° inclination (*Dunlop et al.* 2015). The Swarm spacecrafts were manufactured by the aerospace company Astrium (now part of Airbus Defence and Space since a

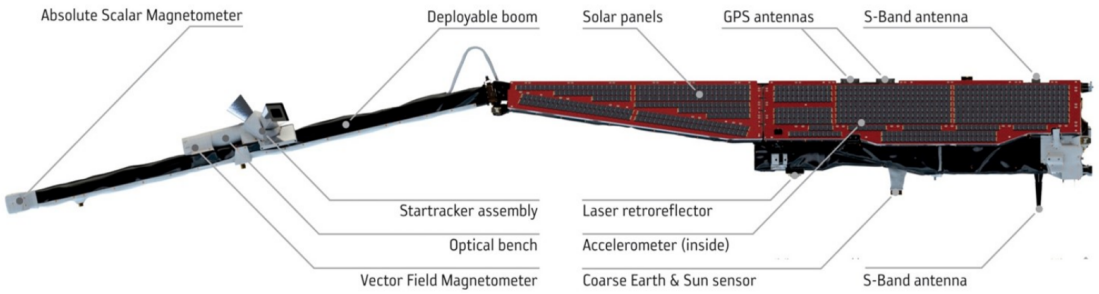

Figure 2.12: Components of the Swarm spacecrafts (source: ESA)

merger in 2013), are identical, and carry onboard a suite of instruments that include a vector field magnetometer, absolute scalar magnetometer, electric field instrument, accelerometer, and laser range reflector (Fig. 2.12, details in *Siemes* 2020). The Swarm spacecrafts were launched 22 November 2013 from Plesetsk Cosmodrome in Akrhangelsk Oblast, Russia on a Rockot vehicle. Swarm offers coverage through the auroral regions and across the high-latitude polar cap at a variety of local times similar to the CHAMP spacecraft (*Reigber et al.* 2002), and through GPS-tracking, provides a source of thermospheric densities generated via POD.

The orientation of the orbit tracks of Swarm-A, Swarm-B, Swarm-C, and the Flock 3P satellites on 26 May 2017 can be found in Fig. 2.13. As the Swarm-A and Swarm-C have orbits that are coincident with each other, density comparisons between MOA's results and Swarm GPS-derived densities is presented using densities from Swarm-A and Swarm-B only.

2.3.1.1 TLE-derived Altitudes

Each individual TLE reports the value of the satellites mean motion, n, at epoch, in units of revolutions per day. As the mean motion is simply one revolution divided by the orbital period, it may be written as (*Lissauer and de Pater* 2019):

$$n = \frac{2\pi}{\tau} \tag{2.11}$$

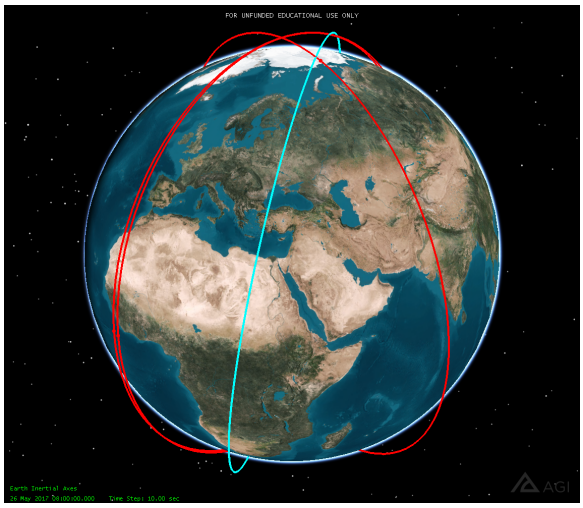

Figure 2.13: Swarm (red) and Flock 3P (cyan) orbits in AGI's STK software.

where τ is the orbital period, and n has units of radians per unit time. Given that the orbital period of a small body orbiting a central body in an elliptical orbit (from Kepler's Third Law), is given as (*Roy* 1988):

$$\tau = 2\pi\sqrt{\frac{a^3}{\mu}} \tag{2.12}$$

where a is the semi-major axis (the longest semidiameter of an orbital ellipse) and μ is the standard gravitational parameter, equating and rearranging Eq. 2.11 and Eq. 2.12 yields an expression for semi-major axis terms of TLE-provided n:

$$a = \left(\frac{\mu}{n^2}\right)^{\frac{1}{3}} \tag{2.13}$$

where the satellite altitude is found by subtracting the mean Earth radius, R_E from this quantity.

Taking the difference between subsequent TLEs and dividing them by the time spanning each yields a deorbit rate (*dSMA*), which can be expressed in units of km/year. Doing so for each Flock 3P satellite shows a spike in deorbit rate across all satellites immediately following the onset of peak of the geomagnetic storm on

28 May (Fig. 2.14). The average maximum rate of change during the storm main phase exceeded 20 km/year, occurring between 29 and 30 May, roughly one day after the storm reached peak intensity on the 28th, as indicated by a_p(2.9(b)). This delay is likely related to the fact the thermospheric density response during geomagnetic storms takes several hours to propagate from high-latitudes to the rest of the globe (*Guo et al.* 2010 and *Oliveira et al.* 2017b), and thus TLEs, which are reported at best once a day, will only show notable decreases in altitude a day after the onset of major energy deposition into the thermosphere.

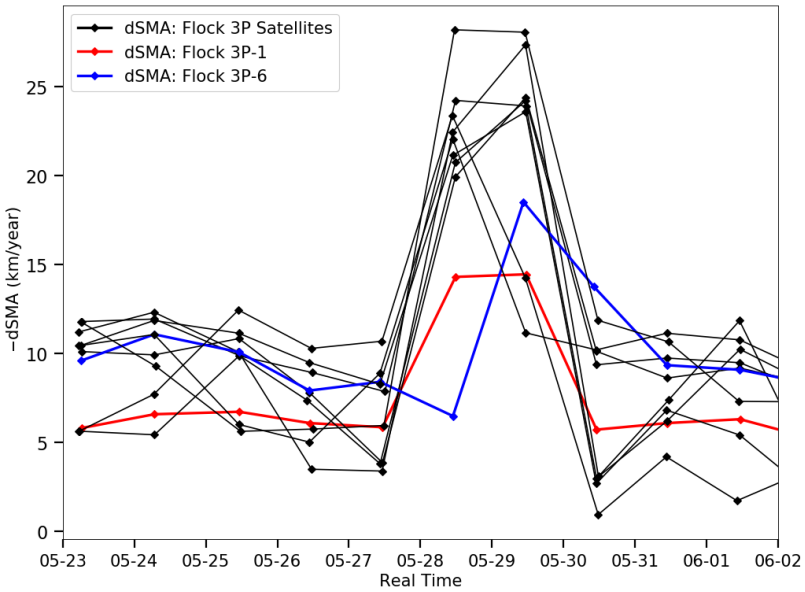

Figure 2.14: Flock 3P deorbit rates derived from TLEs.

It should be noted that as TLEs encode mean orbital elements calculated over intervals with duration of an orbit or more (*Brouwer* 1959, *Kozai* 1959, *Lyddane* 1963 and *Vallado et al.* 2006), any changes in a ($dSMA$) are due to the integral of the density in the time prior to the measurement, such changes do not therefore represent instantaneous changes in density.

2.3.1.2 Optimized Areas and Adjustments to $F_{10.7}$ and ap

Due to the identical construction of all of the Flock 3P calibration satellites, the same geometry file was used by MOA for each Flock 3P satellite during execution, with the dimensions and solar panel areas set to those specified in *Foster et al.* 2015, and the mass of each spacecraft was held constant at 5 kg (*Labs* 2015). The geometry file was constructed with the nadir-pointing attitude of each satellite kept in mind, making it so that the largest face of the spacecraft was normal to the direction of travel. Given that the calibration satellites are sun-synchronous and nadir-pointing, the solar panels are always angled sunward, resulting a cross-sectional area that is expected to vary around 1,000 cm^2.

Table 2.1 shows the 25th, 50th, and 75th percentiles of the A_{OPT} distributions corresponding to each calibration satellite collected 3 weeks prior to the storm, along with the standard deviations for each distribution.

Name	**NORAD ID**	**P25** (cm^2)	**P50** (cm^2)	**P75** (cm^2)	σ (cm^2)
Flock 3P-1	41967	581.70	697.77	817.83	96.40
Flock 3P-2	41966	510.97	800.06	937.53	177.77
Flock 3P-3	41968	735.13	928.46	1,0001.73	112.46
Flock 3P-4	41965	514.59	792.08	933.54	174.01
Flock 3P-5	41971	541.07	845.03	960.02	176.74
Flock 3P-6	41969	740.21	938.62	1,006.81	113.08
Flock 3P-7	41970	748.55	909.60	992.30	101.21
Flock 3P-8	41951	582.06	820.37	947.68	151.54
Flock 3P-9	41973	716.27	921.21	998.10	118.95
Flock 3P-10	41974	660.04	839.23	957.11	122.14
Mean	-	633.06	849.24	955.27	134.43

Table 2.1: AROPT quartiles for Flock 3P calibration satellites between 23 May 2017 and 2 June 2017 (*Brandt et al.* 2020).

Figure 2.15 shows a superimposition of all of the A_{OPT} distributions for each Flock 3P satellite. The peaks of each distribution clustered around 800 cm^2, with the 75th percentiles attaining at mean of 955.27 cm^2, which is close to the expected value of 1,000 cm^2. If 0° is considered to be coincident with the satellite's direction of

travel (the ram direction), the values of A_{OPT} found for each satellite suggest that the largest face of the spacecraft was at an orbit-averaged angle of $\sim 20°$. The high degree of overlap of the distributions suggests that the orientations of each spacecraft were likely quite uniform during the time period, with the possible exception of Flock 3P-1, which perhaps may have had its solar panels either slightly closer to parallel or incompletely deployed, given its high counts around 600 cm^2.

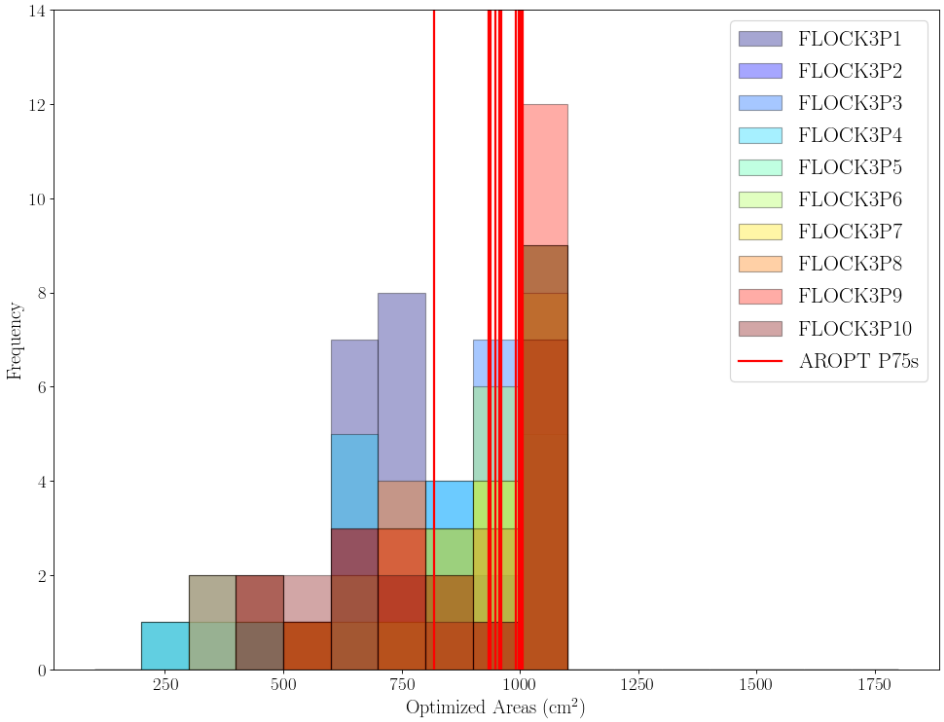

Figure 2.15: Overlapping histograms for Flock 3P (*Brandt et al.* 2020).

The $F_{10.7}$ adjustments corresponding to the 25th percentile of the optimized areas for each satellite all exhibit a characteristic pattern of decreasing to negative adjustments around 26 May, before increasing and peaking during the storm between 28 and 29 May, decreasing thereafter (Fig. 2.3.1.2). It is possible that the pre-storm drop in the value of the $F_{10.7}$ corrections may be due to FOPT responding to the peak in $F_{10.7}$ that occurred on 28 May (2.9(b)). There is a general trend of $F_{10.7}$ adjustments becoming less positive as a function of increasing percentile in response to more of the changes in altitude being dependent on changes in cross-sectional area, through

the overall monotonic behavior is preserved. The closeness of the lines corresponding the 50th and 75th percentiles suggests that this behavior tapers with the increase of percentile, rather than showing an exponential or linear dependence. This is mirrored in the mean difference between the 75th and 50th percentile areas (∼106.63 cm^2) compared to between the 50th and 25th percentile areas (∼216.18 cm^2).

(a) $F_{10.7}$ corrections for all percentiles.

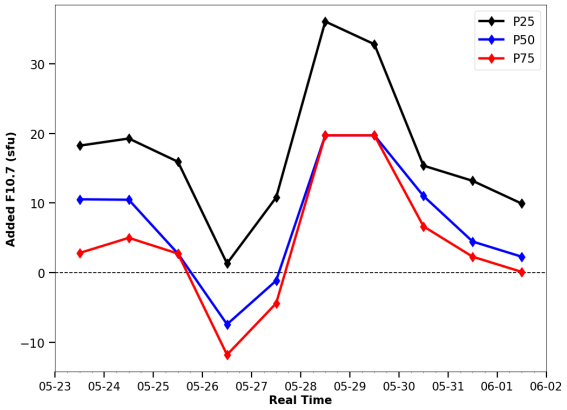

(b) Static and linearly-interpolated $F_{10.7}$ corrections.

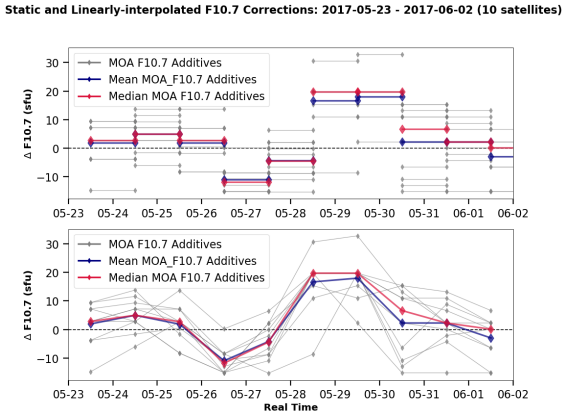

Figure 2.16: FOPT's $F_{10.7}$ adjustments for different percentiles (a) and for the 75th-percentile, shown for each day individually (top) and with linear-interpolation (bottom) (*Brandt et al.* 2020).

MOA's $a_p$adjustments found via APOPT also exhibit an increase during the peak of the storm similar to the F10.7 corrections, but this increase is significantly sharper, jumping from -5 nT on the 28th to +80 nT on the 29th. This kept the $a_p$supplied to NRLMSISE-00 at a much higher level for a longer period of time after the peak of storm, where $a_p$reached its zenith of ∼150 nT, before exhibiting a sharp drop on the 29th (Fig. 2.17). The adjustments to $F_{10.7}$ were rather marginal compared to those for a_p, with the former never exceeding ∼ |17| sfu.

MOA's median index adjustments found across all satellites for $F_{10.7}$ found via FOPT and for $a_p$found via APOPT were used to drive NRLMSISE-00 along the orbits of Swarm-A and Swarm-B during the storm, with the $a_p$adjustments specifically being applied from 28 May to 29 May. It should be noted that as $F_{10.7}$ and $a_p$are global

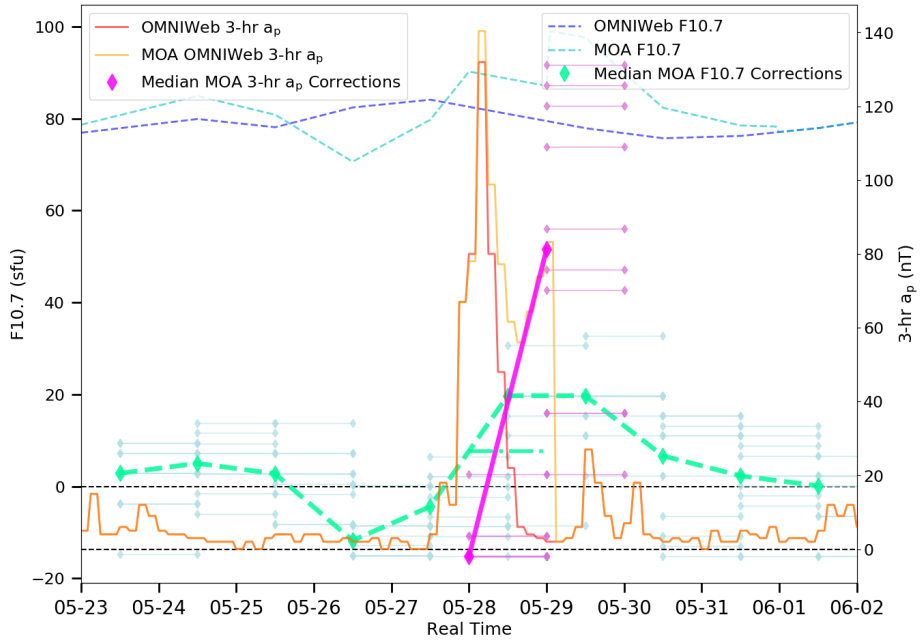

Figure 2.17: All of MOA's solar and geomagnetic index adjustments corresponding to the 75th-percentile optimized area (*Brandt et al.* 2020).

drivers for NRLMSISE-00, the adjustments found by MOA can be applied to any other location in the thermosphere, allowing for improvement of densities for orbit propagation, and also in order to reveal density model biases.

2.3.1.3 Metrics for Validation

All density comparisons are in terms of their orbit-average, which is both most relevant with respect to the driving TLEs that are computed over time intervals on the order of an orbital period or more. Four major metrics for validation are used to validate the efficacy of MOA in comparison to GPS-derived densities from Swarm-A and Swarm-B.

1. $\boldsymbol{\delta_P}$: The percent difference between the peak orbit-averaged density of NRLMSISE-00, and that of either MOA or Swarm:

$$\boldsymbol{\delta_P} = \frac{|\boldsymbol{\rho_N} - \boldsymbol{\rho_S}|}{\left[\frac{\boldsymbol{\rho_N}+\boldsymbol{\rho_S}}{\mathbf{2}}\right]} \times \mathbf{100\%} \tag{2.14}$$

where $\boldsymbol{\rho}$ is either the NRLMSISE-00 or MOA orbit-averaged density, and $\boldsymbol{\rho_S}$ is the Swarm GPS-derived orbit-averaged density.

2. $\boldsymbol{\eta}$: The ratio of the peak orbit-averaged density magnitude to the 24-hr-averaged orbit-averaged density prior to the peak orbit-averaged density within the 24 hours immediately preceding the peak orbit-averaged density.

3. $\boldsymbol{\rho_T}$: Total-time integrated density in kg·s·km$^{\mathbf{3}}$ during the main phase of the storm. In order to set the boundaries for computing this integral, the following means are employed: (a) For each point, the arithmetic mean density and standard deviation of the density for the Swarm orbit-averaged density is calculated for the preceding 12 hours. (b) The lower bound of the integral is set as when the density exceeds the sum of the mean and standard deviation at the associated time, and all of the density values for the next 12 hours also satisfy that condition. (c) The upper bound of the integral is found using identical methods as the lower bound, but proceeding backwards from the density values at the end of the chosen time period.

4. $\boldsymbol{t_l}$: The time difference in hours between the peak in either the NRLMSISE-00 or MOA orbit-averaged densities, and the peak in the Swarm GPS-derived orbit-averaged densities.

2.3.1.4 Swarm Density Comparisons

Orbit-averaged densities found by MOA for the geomagnetic storm between 23 May 2017 and 2 June 2017 are presented, and compared with orbit-averaged GPS-derived densities from Swarm-A and Swarm-B. First, effects of different selections

(a) MOA densities by percentile for Swarm-A. (b) MOA densities by percentile for Swarm-B.

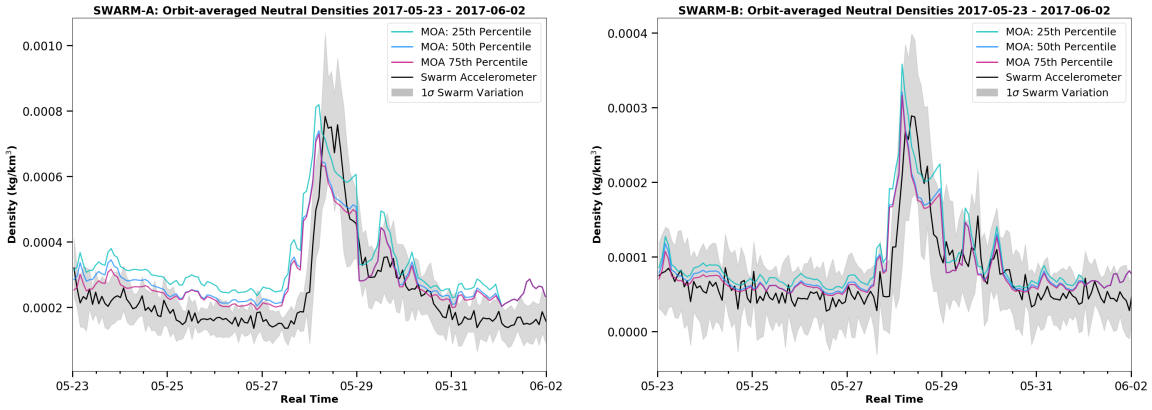

Figure 2.18: MOA densities by percentile for Swarm-A (left) and Swarm-B (right) (*Brandt et al.* 2020).

of AROPT's A_{OPT} percentile on results are explained, and second, the results corresponding to the 75th percentile are compared and analyzed, with MOA's performance contrasted with that of uncalibrated NRLMSISE-00 in reference to the Swarm data.

Percentile Effects

Selection of a percentile for A_{OPT} from AROPTs distributions affects the magnitude of the index adjustments downstream, changing the magnitude of orbit-averaged densities that are later found when the new indices are used to drive NRLMSISE-00. This can be seen clearly in Fig. 2.3.1.4, which shows a comparison between Swarm-derived and MOA-derived orbit-averaged densities corresponding to different AROPT percentiles.

During the main phase of the storm, the peak orbit-averaged densities corresponding to each of MOA's percentiles were very close to the peak orbit-average densities for Swarm, with those corresponding to the 50th and 75th percentile cases being closest to each other. For Swarm-A, the values of δ_P for MOA were ∼4.5%, ∼5.8%, and ∼7.2% for the 25th, 50th, and 75th percentile, respectively. Along Swarm-A, increasing the percentile of the optimized area slightly reduced the accuracy in the peak orbit-averaged density. Along Swarm-B this trend was reversed, with values

(a) MOA, NRLMSISE-00, and GPS-POD densities for Swarm-A.

(b) MOA, NRLMSISE-00 and GPS-POD densities for Swarm-B.

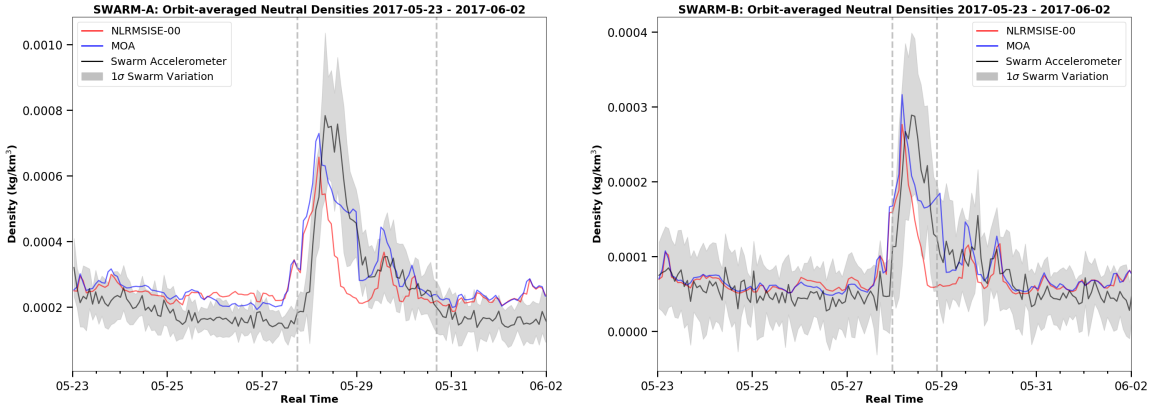

Figure 2.19: MOA, NRLMSISE-00, and GPS-POD densities along Swarm-A (left) and Swarm-B (right) (*Brandt et al.* 2020).

of δ_P being ∼21.4%, ∼10.4%, and ∼9.1% for the 25th, 50th, and 75th percentile cases, respectively. Comparison to the 75th percentile MOA results to Swarm and NRLMSISE-00 follows.

Main Results

Comparison of the 75th percentile MOA results to NRLMSISE-00 and Swarm orbit-averaged densities immediately shows that MOA exceeds NRLMSISE-00 in maintaining higher values of the density for a longer duration during the main phase of the storm, as evidenced by an increase in the width of the peak (Fig. 2.3.1.4). Along both Swarm-A and Swarm-B, MOA attempted to recreate the second peak in the density occurring just before 29 May, but was unable to reach the necessary amplitude to do so most accurately, this being most obvious along Swarm-B. Additionally, along both orbits, MOA's values for t_l were identical to that of NRLMSISE-00, which is likely due the fact that NRLMSISE-00 (and therefore MOA by proxy) is unable to account for the time delay between when $a_p$peaks and the when the local density at the spacecraft peaks. As NRLMSISE-00 applies indices instantaneously, this delay, which can be up to 4 hours in duration (*Bruinsma et al.* 2006), is not captured.

Table 2.2 displays the values of the peak orbit-averaged density (maxρ), δ_P, t_l, η, and ρ_T along Swarm-A. Values of maxρ, δ_P, t_l, η, and ρ for MOA were all closer to those of Swarm compared to uncalibrated NRLMSISE-00. The integrated effect of the increased width of the storm can be quantified by the percent difference between MOA ρ_T and Swarm ρ_T, which was ∼4.0%, compared to a percent difference in the integrated densities of ∼25 for NRLMSISE-00.

Swarm-A Orbit-averaged Density Metrics					
Source	**maxρ** $\left(\frac{\mathbf{kg}}{\mathbf{km^3}}\right)$	**δ_P**	**t_l (hours)**	**η**	**ρ_T** $\left(\frac{\mathbf{kg \cdot s}}{\mathbf{km^3}}\right)$
Swarm	7.8×10^{-4}	-	-	2.6	98.3
NRLMSISE-00	6.6×10^{-4}	17.6	3.1	1.8	79.8
MOA	7.3×10^{-4}	7.2	3.1	1.9	102.3

Table 2.2: Tabulated values of maxρ, δ_P t_l, η, and ρ_T along Swarm-A (*Brandt et al. 2020*).

Table 2.3 displays the values of the peak orbit-averaged density (maxρ), δ_P, t_l, η, and ρ_T along Swarm-B. Here, the MOA overestimates the value of maxρ by ∼10.1%, resulting in a value of η different from that of Swarm by 11% compared to 4% for NRLMSISE-00, which is the converse of the Swarm-A case, where MOA's value of maxρ only shows 6.6% difference from Swarm compared to 17% for NRLMSISE-00. Additionally, the percent difference between MOA ρ_T and Swarm ρ_T, which was ∼3.7%, compared to a percent difference in the integrated densities of ∼34.6 for NRLMSISE-00. In contrast to Swarm-A, MOA performs worse than NRLMSISE-00 regarding δ_P, where it gives a greater value of 7.6 compared to NRLMSISE-00's 4.4, in comparison to 7.2 vs. 17.6 in the former case.

Outside of the main phase, where only the $F_{10.7}$ adjustments were applied, MOA, MOA performed marginally better than NRLMSISE-00, specifically just prior to initial storm onset along Swarm-A and during the recovery phase along Swarm-B. This improvement in performance is related to adjusting $F_{10.7}$ downwards just before the main phase of the storm, and adjusting it upwards during the recovery phase. Both

Swarm-B Orbit-averaged Density Metrics					
Source	**maxρ** $\left(\frac{\text{kg}}{\text{km}^3}\right)$	**δ_P**	**t_l (hours)**	**η**	**ρ_T** $\left(\frac{\text{kg·s}}{\text{km}^3}\right)$
Swarm	2.9×10^{-4}	-	-	2.5	16.6
NRLMSISE-00	2.8×10^{-4}	4.4	4.8	2.6	11.7
MOA	3.1×10^{-4}	7.6	4.8	2.8	16.0

Table 2.3: Tabulated values of maxρ, δ_P t_l, η, and ρ_T along Swarm-A (*Brandt et al.* 2020).

NRLMSISE-00 and MOA overestimated the density prior to the initial storm onset and during the tail end of the recovery phase, with this being most prominent along Swarm-A, as along Swarm-B, both MOA and NRLMSISE-00 densities never departed the Swarm 1σ boundaries during those times.

2.4 Summary

The challenges involved in thermospheric density modeling during geomagnetic storms have led to the development of various methods as solutions. These include HASDM (*Storz et al.* 2005), TLE-based least-squares optimization (*Doornbos et al.* 2008), multi-model assimilative algorithms like Dragster (*Pilinski et al.* 2016), and reduced-order modeling (*Gondelach and Linares* 2020). Each of these methods has their benefits, but many exhibit drawbacks such as requiring access to classified satellite tracking data, being computationally extensive, and mathematical complexity. The Multifaceted Optimization Algorithm (MOA) has been presented and results for its application during the geomagnetic storm of May 2017 analyzed. MOA operates using simple methods that move from satellite TLEs to new model densities:

1. Gather TLEs from calibration satellites.
2. Employ SpOCK to compute A_{OPT} for each modeled satellite using AROPT.
3. Holding A_{OPT} for each modeled satellite constant, employ FOPT for each modeled satellite to find $\text{F}_{10.7}$ adjustments for each.

4. Holding the most-recent pre-storm $F_{10.7}$ adjustment constant for each modeled satellite, employ SpOCK to find adjustments to $a_p$using APOPT.

5. Calculate the median $F_{10.7}$ and $a_p$adjustments across all modeled satellites.

6. Apply the $F_{10.7}$ and $a_p$adjustments along the orbit of a validation satellite (such as Swarm, CHAMP, GRACE, or GOCE) for validation, using GPS-derived (POD) or accelerometer-derived orbit-averaged densities.

MOA does not rely on classified high temporal/spatial-resolution satellite tracking data like HASDM, does not compute model driver corrections by comparing model densities to TLE-derived densities as in *Doornbos et al.* 2008, rely on a suite of full physics models and extensive high-latitude and solar drivers such as in Dragster, or require mathematically-intensive construction of a ROM driven by data assimilation and usage of modified equinoctial elements. Additionally, it is capable of demonstrating appreciable improvements in storm-time density modeling with the usage of as few as 10 calibration satellites, showing that only is it possible to achieve improvements in storm-time density modeling with simple methods, but that a large number of calibration satellites may not be needed to generate statistically significant improvements.

MOA does, however, display an important limitation. It's sole reliance on orbit propagation limited by TLEs places a lower limit on the power of the obtained solar and geomagnetic index adjustments due to the fact that the temporal resolution of TLEs rarely is better than 1 or 2 days. Therefore, the obtained global index adjustments run the risk of smoothing over rapid density changes, which may manifest as differences in MOA's performance during CIR-driven vs. CME-driven storms, or during double- or triple-peaked geomagnetic storms. The minor difficulty MOA displayed in capturing the second orbit-averaged density peak during May 2017 is one such example of this limitation.

This limitation may be circumvented by drastically increase the number of calibration satellites from which TLEs are obtained. This would serve to aid in filling in the gaps regarding the issue of temporal resolution, since TLEs are not reported at the same time each day for each satellite. Additionally, as the density response of MOA is limited by this issue of temporal resolution, which may only be partially remedied by the inclusion of many more calibration satellites, this issue may further be addressed by the usage of index corrections that vary according to a univariate spline rather than the linear interpolation that is currently the case.

Additional future work may involve a multi-storm assessment of MOA to determine its performance as a function of storm intensity, as well as a multi-model study to determine how efficacious MOA's methods are when adjusting densities from different empirical and physical models during geomagnetic storms. Given that different thermospheric models exhibit different biases and tend to display varying levels of performance as a function of altitude and latitude, MOA may also serve as a way to further probe the biases of these models, in addition to demonstrating how its methods may or may not be more efficacious under certain solar and geomagnetic conditions or at certain latitudes and altitudes.

CHAPTER III

Thermospheric Model Storm-time Superposed Epoch Analysis

3.1 Introduction

Empirical models, as described in Section 1.2.2, tend to perform poorly during geomagnetic storms, but as each empirical model is parameterized differently, the nature of their performance during storms will differ. A superposed epoch analysis of storm-time neutral densities across three different empirical thermosphere models is presented. In Section 3.1, the nature, use, and function of superposed epoch analysis in the context of thermospheric research is elaborated upon, including notable approaches from the relevant literature are covered, followed by a brief description of the three models involved: MSIS-00, JB-2008, and DTM-2013. The goal of the superposed epoch analysis is to highlight characteristic differences in the performance of those different empirical thermospheric density models as a function of altitude, storm intensity, and F10.7 for the purposes of model calibration. Model densities are all compared to accelerometer-derived densities from the CHAMP satellite, as described in Section 3.2, which contains a description of the methods involved in the analysis. Results are presented in Section 3.3. The conclusion and future work follows in Section 3.4.

3.2 Methodology

In this study, Superposed Epoch Analysis (SEA) was used to study the behavior of three empirical thermosphere density models during geomagnetic storms. The models considered include MSIS-00, JB-2008, and DTM-2013. Storms were selected based on intensity, and combined atop a normalized epoch timeline to show their overall behavior across multiple storms. Peaks model densities across the storms are plotted against peak Dst and peak satellite densities in order to compare the responsiveness of each model to Dst and the performance of each model in comparison to satellite data from CHAMP.

3.2.1 Superposed Epoch Analysis

SEA is a statistical tool used in data analysis to uncover periodicities, persistent morphological features, or correlations in several sequences of time-sequenced data (*Singh and Badruddin* 2006). The original method of analysis was proposed by Charles Chree in his study of sunspots, where he revealed a 27-28 day period relating sunspot activity to magnetic perturbations observed on Earth (*Chree* 1912 and *Chree* 1913). Since then, the method has been used in a variety of diverse ways, including searching for weak signals in solar flare data to improve forecasting capabilities (*Mason and Hoeksema* 2010), investigating the thermosphere response to substorms caused by energy released from the magnetic tail into the high-latitude ionosphere (*Clausen et al.* 2014), investigating the global ionosphere-thermosphere response to CME-driven geomagnetic storms (*Oliveira et al.* 2017a), studying variations in energetic electron flux during CIRs (*Yin et al.* 2019), studying the time-evolution of geomagnetic disturbances caused by high-speed streams from coronal holes (*Kumar and Badruddin* 2021), and even studying the relationship between satellite anomalies and galactic cosmic rays (*Shen et al.* 2021).

SEA is generally performed in the following series of steps:

1. For the phenomenon being studied, define a data sequence encapsulating a single occurrence of such as a **key time** or basis by which to form an **epoch time** over which all data sequences will be superposed.

2. For all other data sequences encompassing the occurrence of the phenomenon at different times, extract those data sequences, taking care to ensure their durations coincide with that of the key time.

3. Superpose all extracted subsets with the original subset, by averaging them together.

For time series that do not have the same lengths or contain data recorded at different or irregular intervals, some studies to use data binning across each data sequence (involving calculating the average value in each bin) or to segment each data sequence into constituent sections/phases, calculate the average duration of each section or phase, and stretch or compress each phase in each data sequence to conform to the average durations before performing the superposition (Figure 3.8(a)). The latter method is featured in *Katus et al.* 2013, where it was used to superposed Dst for the purpose of studying convection during geomagnetic storms; this procedure was used for the analysis of this study, and is described in detail in Section 3.2.4.

3.2.2 NRLMSISE-00, JB-2008, and DTM-2013

While a general overview of thermospheric models, including those of the MSIS, JB, and DTM families can be found in Section 1.2.1, there are some important distinctions to be made between the three empirical models from each family used in the following SEA study: MSIS-00, JB-2008, and DTM-2013.

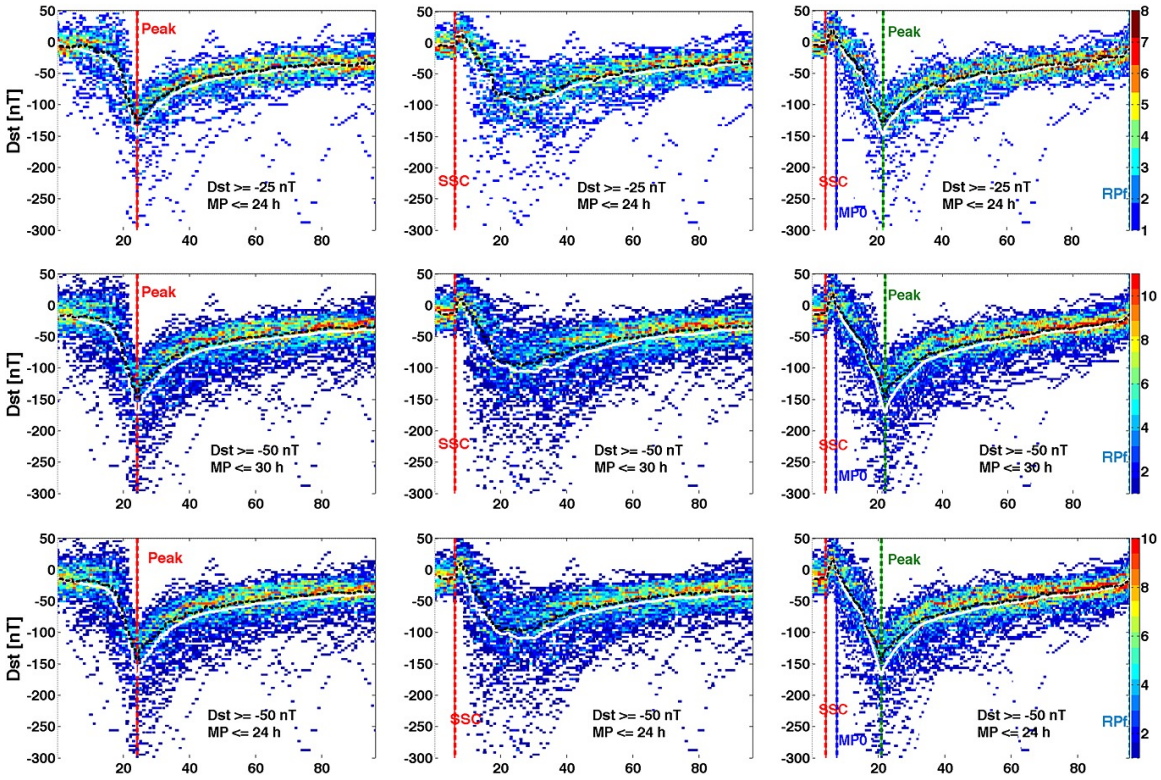

Figure 3.1: Superposed Dst from *Katus et al.* 2013 for intense geomagnetic storms.

3.2.2.1 NLRMSISE-00

The MSIS-00 model (*Picone et al.* 2002) is an empirical atmospheric model extending from the Earth's surface to the exobase (1,000 km). The model relies on data from ground-based Fabry-Perot Interferometer (FPI) and Incoherent Scatter Radar (ISR) observations, rocket-based measurements, and satellite-based measurements, including data derived from drag measurements and accelerometers, as well as solar UV occultation measurements from the Solar Maximum Mission. It takes as inputs the following parameters:

- Date and time
- Geodetic altitude
- Latitude and longitude
- 81-day average of F10.7

- Daily F10.7 solar flux
- a_p (can either be daily, or an array of seven values that includes: (1) daily a_p, (2) ap at the current time, (3) a_p 3 hours prior, (4) a_p 6 hours prior, (5) a_p 9 hours prior, (6) the average of a_p between 12 and 33 hours prior, and (7) the average of a_p between 36 and 57 hours prior)

MSIS-00 functions through fitting a set of parametric equations to this data in order to approximate the vertical structure of the atmosphere as a function of location, time, solar activity (F10.7), and geomagnetic activity (a_p). From the ground to the exobase, the model provides altitude profiles of temperature $T(z)$, number densities of various neutral species (He, O, N_2, O_2, Ar, H, and N) in thermal equilibrium at the temperature $T(z)$, and total mass density $\rho(z)$. The expression for temperature is written as follows (*Walker* 1965):

$$T(z) = T_\infty - (T_\infty - T_{120}) \exp\left[-\sigma\zeta\right], \tag{3.1}$$

where the geopotential altitude ζ is given as

$$\zeta = \frac{(z - 120)\,(R + 120)}{R + z}, R = 6356.77 \text{ km}, \tag{3.2}$$

where T_{120} is the temperature at 120 km, T_∞ is the exospheric temperature, z is the altitude in km, and σ is given as

$$\sigma = s + \frac{1}{R + 120} = s + 0.00015, \tag{3.3}$$

where s is an analytic function of T_∞ representing the solar cycle, short period solar activity, variations of solar activity, semiannual, diurnal, and geomagnetic activity variations of atmospheric density (*Jacchia and Slowey* 1963).

Above 500 km, the number density of a high-altitude 'anomalous oxygen' not in

thermal equilibrium with $T(z)$ is calculated, and combined with the estimated mass densities of the other species or the total 'effective' mass density. This allows for the accounting for possible hot atomic and singly ionized oxygen thought to be present in the polar exosphere during their respective summers (*Hedin* 1989 and *Keating et al.* 1998).

MSIS-00 employs its GTD7 standard model subroutine below 500 km, and its GTD7D routine above 500 km to incorporate contributions from anomalous oxygen. It uses a latitude-dependent gravity field and effective radius, and uses spherical harmonics to represent spatial variability of parameters depending on temperature and species number density. Details can be found in Appendix A of *Picone et al.* 2002, and furthermore in *Hedin* 1987.

3.2.2.2 JB-2008

The JB-2008 model (*Bowman et al.* 2008) is an empirical atmospheric model extending from 90 km to 2500 km in altitude that computes total atmospheric mass density through temperature calculations related to solar input (F10.7) and geomagnetic activity (K_p). The core formulae for thermospheric and exospheric temperatures appearing in the original iteration of the model, respectively, are (*Jacchia* 1971):

$$T(z) = T_\infty - (T_\infty - T_0) \exp\left[-\sigma\left(z - z_0\right)\right], \tag{3.4}$$

$$T_\infty = 379 + 3.24\overline{F_{10.7}} + 1.3\left(F_{10.7} - \overline{F_{10.7}}\right), K_p = 0, \tag{3.5}$$

where z is the altitude above the Earth's surface in km, z_0 the reference altitude (typically the mean Earth radius), T_∞ is the exospheric temperature, $T_0 = 183$ K is the temperature at z_0=90 km, and σ is the relative vertical temperature gradient $\mathrm{d}T_{120}/\left(T_\infty - T_{120}\right)$. The equation for the change in temperature due to geomagnetic activity appearing in the first iteration of the model is:

$$\Delta T_\infty = (21.4 \sin\phi + 17.9)\,\overline{\mathrm{K_p}} + 0.03 \exp\left(\overline{\mathrm{K_p}}\right), \tag{3.6}$$

where $\overline{\mathrm{K_p}}$ is the 9-hour mean of the original 3-hourly planetary $\mathrm{K_p}$ index (the mean of the 3-hourly magnetic activity relative to a quiet-day curve obtained from 13 geomagnetic observatories between 44° and 60° northern or southern latitude) and ϕ is the latitude in degrees.

Similar to MSIS-00, the equations of JB-2008 are parametric fits to data; specifically, daily density values from drag analysis of numerous satellites between 175 and 1000 km, satellite-derived thermospheric temperature measurements, temperature coefficients computed by HASDM, accelerometer-derived densities from the CHAMP and GRACE satellites, solar indices in the EUV and Far-Ultraviolet (FUV) range computed from on-orbit sensor data, and Dst. Incorporation of additional solar indices modifies Equation 3.5 to have six terms due to contributions from 26-34 nm solar EUV emission, solar Mg II emission near 280 nm, and 0.1-0.8 nm solar X-ray emission. In JB-2008, semiannual density variation is captured by a linear relation between a change in logarithmic neutral density and the product of a height-dependent amplitude and the averaged density variation over time in which the amplitude is normalized to 1. Equation 3.6 was recast as a function of Dst instead of $\bar{\mathrm{K}}_\mathrm{p}$, and was modified for each individual storm phase. Further details can be found Section III of *Bowman et al.* 2008. Unlike MSIS-00, JB-2008 does not estimate temperatures of individual neutral species or number of densities of individual neutral species. Due to the fact that JB-2008 has its own underlying geophysical database that supplies F10.7 and Dst, it requires fewer inputs than the other models. JB-2008 also does not employ different density algorithms based on altitude, as MSIS-00.

- Date and time
- Geodetic altitude

- Geodetic latitude and longitude

3.2.2.3 DTM-2013

The DTM-2013 model (*Bruinsma* 2015) is an semi-empirical model describing the temperature, density, and composition of the thermosphere. It is valid between 120 and 1500 km, and computes a representation of the total density by summing the contributions of N_2, O_2, O, He, and H under the assumption of static diffuse equilibrium according to the following formula:

$$\rho(z) = \sum_i \rho_i \left(z_{120}\right) f_i(z) \exp\left[G_i\left(L\right)\right], \tag{3.7}$$

where $\rho_i\left(z_{120}\right)$ is the partial density of neutral species i at 120 km altitude, and $f_i(z)$ is a temperature-dependent height function for that particular species with the following form (*Bruinsma et al.* 2012):

$$f_i(z) = \left[\frac{T_{120}}{T(z)}\right]^{1-\alpha+\gamma_i} \exp\left(-\sigma\gamma_i\eta\right), \tag{3.8}$$

with (as in both MSIS-00 and JB-2008 in Equations 3.1 and 3.9, respectively)

$$T(z) = T_\infty - \left(T_\infty - T_{120}\right) \exp\left[-\sigma\zeta\right], \tag{3.9}$$

where in Equation 3.8, α, T_∞ is the exospheric temperature, is the thermal diffusion coefficient for He and H (-0.38), $\gamma_i = m_i g(120 \text{ km})/\sigma k T_\infty$, m_i is the mass of species i, $g(120\ \text{km})$ is the gravitational acceleration at 120 km altitude, σ is the relative vertical temperature gradient $\mathrm{d}T_{120}/\left(T_\infty - T_{120}\right)$, k is the Boltzmann constant, and ζ is the geopotential altitude, as in Equation 3.2.

$G_i(L)$ is a spherical harmonic function of exospheric temperature and partial density variations dependent on the environmental parameters L (latitude, local solar time, solar flux, and geomagnetic activity). DTM-2013 models the exospheric tem-

perature and the atmospheric constituents each with up to 50 coefficients, which are estimated together with the concentrations at 120 km in a least-squares adjustment. The function G is used to model periodic (annual and semi-annual terms, diurnal, semidiurnal, and terdiurnal terms) and non-periodic variations (constant zonal latitude coefficients, and coefficients relating solar and geomagnetic activity to temperature and density), similar to but more comprehensive than the individual formula in JB-2008 that captures the semiannual density variation.

DTM-2013 models temperature as well as major and minor constituents using either F10.7 or the F30 index, the solar radiation at 30 cm (*de Wit et al.* 2014), which must be rescaled to F10.7 via the equation below before the algorithm is executed (Bruinsma 2020, private communication):

$$\mathrm{F30}_s = -1.5998 + 1.553755 \cdot \mathrm{F30} \tag{3.10}$$

DTM-2013 uses the $\mathrm{K_p}$ index to model the temperature effects of geomagnetic activity, similar JB-2008, but it is also capable of using the $\mathrm{K_m}$ index (derived from the $\mathrm{a_m}$ Index, and described in Section 8.5.2 of *Menvielle et al.* 2011).

The table of coefficients underlying DTM-2013 owes its creation to parametric fits of assimilated data from CHAMP, GRACE, GOCE, Starlette and Stella (*Sośnica et al.* 2014), Deimos-1 (`http://www.deimos-imaging.com`), and Cactus (*Beaussier et al.* 1977) satellite accelerometer-derived densities, temperatures from the OGO-6 satellite (*Donahue et al.* 1972), temperatures, He, O, and $\mathrm{N_2}$ measured by DE-2 (HOF 1981), $\mathrm{N_2}$ measured by the AE-C satellite, and temperatures, He, and O measured by the AE-E satellite (*Dalgarno et al.* 1973, *Spencer et al.* 1973, *Brinton et al.* 1973, and *Nier et al.* 1973). The inputs to DTM-2013 are as follows:

- Local time
- Day of the year

- Geodetic altitude
- Longitude
- K_p 3 hours prior
- K_p 24 hours prior
- 81-day average F10.7 or F30
- Daily F10.7 or F30

Major differences between the models are summarized in Table 3.1 below.

Table 3.1: Major features of the three major empirical density models.

Feature	MSIS-00	JB-2008	DTM-2013
No. Inputs	7 or 13	4	8
Altitude Range (km)	0-1000	90-2500	120-1500
Sum over Composition	Y	N	Y
Solar Flux	F10.7	F10.7	F10.7 or F30
Geomagnetic Activity	a_p	K_p or Dst	K_p or K_m

3.2.3 Storm Selection

Storms were selected between a start and end date, necessarily coinciding with times for which corresponding satellite density data exists. Given that geomagnetic storms exhibit unique behavior and vary in intensity, selection criteria from *Katus et al.* 2013 were adopted in order to obtain a selection of storms with similar and easily definable characteristics. These selection criteria depend on how the phases of each storm were defined. The Dst index was used for this purpose:

- (4) Peak (Start of the Recovery Phase): The lowest (most negative) value of Dst.
- (3) Start of the Main Phase: The maximum (most positive) Dst within the 24 hours leading up to the peak Dst.

- (2) Start of the SSC: An increase in Dst by at least 10 nT within 8 hours before the beginning of the main phase.
- (1) Storm Start: Defined as 4 hours prior to the SSC.
- (5) End of the Recovery Phase: The end of the recovery phase is set at the location of maximum Dst within 96 hours after the peak.

The Dst index was also used to classify storms by their intensity, using the categories described by *Sugiara and Chapman* 1960 and *Zesta and Oliveira* 2019:

- Weak: -50 nT $<$ min(Dst) $\leq$ -30 nT
- Moderate: -100 nT $<$ min(Dst) $\leq$ -50 nT
- Strong: -150 nT $<$ min(Dst) $\leq$ -100 nT
- Severe: -150 nT $<$ min(Dst) $\leq$ -250 nT
- Extreme (Superstorm): min(Dst) $<$ -250 nT

Storms preceded by a disturbance of moderate strength or greater were discarded. This involved discarding events for which Dst dropped below -50 nT 12 hours prior to the main phase. Storms with more than one peak at or below -50 nT within 48 hours of the first peak after the main phase were also discarded. An example of a storm that would be discarded according to these restrictions can be found in Figure 3.2.

Additionally, in ensure periods of quiet time between storms considered, storms occurring within 24 hours of the end of a previous storm were neglected, and in order to limit selection to CME-driven storms, only storms with a sudden commencement (SSC) were accepted. SSCs are caused by compression of the magnetosphere caused by the passage of a shock or tangential discontinuity in the solar wind (*Matsushita* 1962 and *Joselyn and Tsurutani* 1990); the existence of a SSC was approximated per

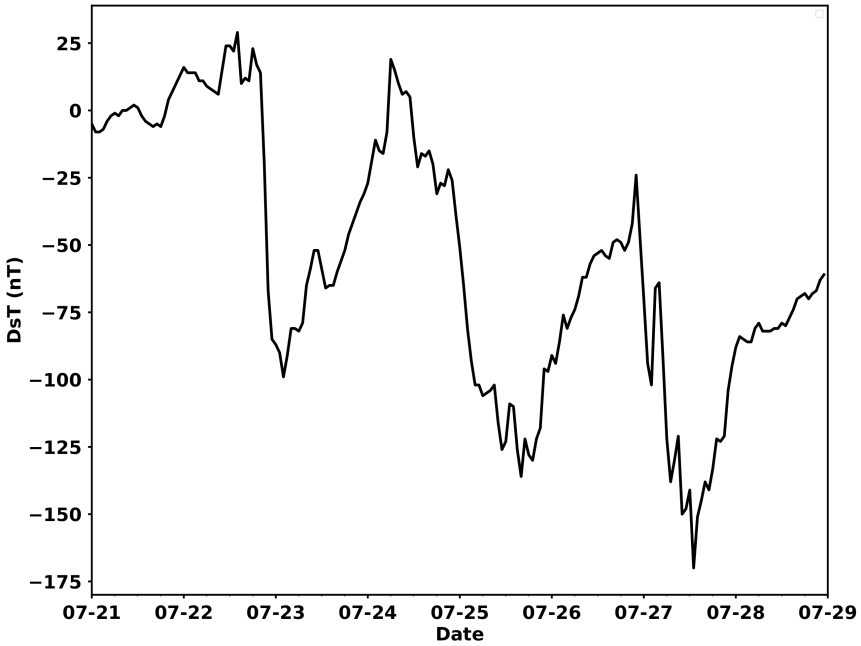

Figure 3.2: Dst for a triple-peaked geomagnetic storm.

Katus et al. 2013 by an increase in Dst by at least 10 nT within 8 hours before the beginning of the main phase. Due to the fact that Dst has a 1-hour resolution, for storms determined to have a SSC within 1 hour of the main phase, it may in fact be unclear whether or not the SSC in these cases is truly representative of a CME impact. To avoid this uncertainty, storms with a SSC within one hour of the main phase were also rejected.

Solar and geomagnetic index data were downloaded from NASA OMNIWeb between the specified start and end dates, and F30 index data was obtained from `ftp://ftpsedr.cls.fr/pub/previsol/solarflux/forecast/absolute` for the same time period. For the entire time period, splines were found for all of the indices.

Applying the above selection criteria to the Dst data yielded a set of usable storms out of a larger total. For each storm, the peak of storm (most minimum Dst) was identified and used to isolate a time period over which all of the phases of the storm were determined. The beginning of that time period was set as three days prior to the peak, and the end of the time period was set at nine days after the beginning. The

times of the main phase (3), start (1), SSC (2), peak(4), and ending of the recovery phase (5) were then found for each storm.

Densities were then found for each storm during the time period for that storm found via parsing of Dst, being obtained from the CHAMP, GOCE, GRACE, or Swarm spacecraft accelerometer data from ftp://thermosphere.tudelft.nl/version_01/, and then computed by MSIS-00, JB-2008, and DTM-2013. The models were all run with their standard inputs, as mentioned in Section 3.2.2, with MSIS-00 being run with the array of 7 a_p values, and DTM-2013 being run using F30 scaled to F10.7 as in Equation 3.10. Solar and geomagnetic indices used to drive the models were calculated from the splines found from the downloaded OMNIWeb data. Densities found for each storm were saved to an individual file for later retrieval by the SEA routine.

3.2.4 SEA

Prior to conducting the SEA proper, it was necessary that the satellite and model densities were orbit-averaged. The densities were then expressed in terms of percent-change from the 24-hour average preceding the storm, as shown by

$$\delta_\rho(\tau) = 100 \times \frac{\rho(\tau) - \rho_a}{\rho_a}, \tag{3.11}$$

where $\rho(\tau)$ is the orbit-averaged neutral density at time τ, and ρ_a is the neutral averaged over duration of one day, directly prior to the start of the storm, defined as 4 hours prior to the SSC.

Expressing the densities in terms of percent change from their averaged quiet time value allows a more direct analysis of probing the storm response characteristics of each density model, as a given model may be biased to either overestimate or underestimate the quiet time neutral density, but vary wildly in how it models the density response as a percentage increase. Focusing on raw densities themselves

therefore doesn't give the clearest picture of storm time model performance in terms of thermosphere dynamics for these empirical models.

After the densities are orbit-averaged and expressed in terms of percent change from their average quiet time value, a normalized timeline is constructed. This is done by determining the average duration of the individual storm phases across all of the storms collected, and creating a representative epoch timeline from those averages. Then, for each storm, its respective phases are stretched or compressed in duration to conform to those of the average timeline, while retaining the same density behavior in their respective phase. The following is done for each phase:

1. A linear univariate spline is constructed for the density data of the given storm.

2. The time cadence of the splined density data is increased by retaining the duration of the storm but increasing the number of time elements to 10,000.

3. A splined density value is found at each of the 10,000 times.

4. The average timeline is constructed from the mean durations of each phase calculated across all storms, and given the time cadence of the average orbital period of the satellite (CHAMP) during the storm.

5. The times of specific storm are truncated to those between its respective start and end of its recovery phase.

6. For the time between the beginning/end of each, the densities of the storm are isolated.

7. The times corresponding to the phase in question are then isolated from the average timeline.

8. The phase times for the storm in question are then stretched or compressed by conforming them to the boundaries of the phase times of the average timeline,

and given a time cadence corresponding to the number of density values of the storm in question in its respective phase (retains the density behavior).

9. A linear univariate spline is then constructed between the stretched/compressed times and the storm's density values in the phase.

10. Representative densities for the phase are then calculated by applying that spline at the phase times for the average timeline.

This conforms all of the densities for each storm to a timeline of uniform length, while retaining the behavior in each phase so that density data for each storm can be directly superposed with its counterparts.

Dst for an extreme geomagnetic storm occurring during November 2001 is shown in Figure 3.3. Figure 3.4 shows the SEA process occurring step by step, using the November 2001 CHAMP densities to show how the compression and stretching of the epoch timelines occurs for just 7 storms collected between 2001-05-01 and 2002-05-01, along an epoch timeline ~ 81.4 hours in duration. Figure 3.4 displays the process of moving from raw CHAMP densities shown just for a single storm, to orbit-averaged densities for that storm, to displaying the orbit-averaged densities in terms of percent change, to showing the orbit-averaged densities (in units of percent change) for all storms together, and is followed by Figure 3.5, which finally shows the superposed densities for the CHAMP data themselves.

After all of the storm densities are collected and processed so that they conform to the normalized timeline, they are superposed by adding the densities at each point along the normalized timeline, and divided by the number of storms involved in the superposition in order to compare the mean behavior in density modeling from each of the models in comparison to the satellite data (Fig 3.6). For the superposed density data corresponding to each data source (whether satellite or one of the models), at each time along the normalized epoch timeline, the maximum and minimum values

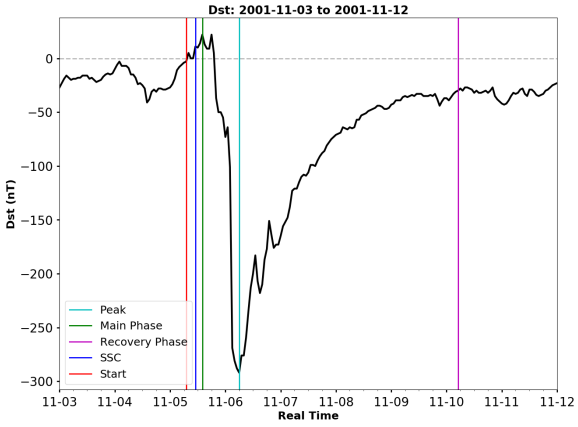

Figure 3.3: Dst and phases for an extreme geomagnetic storm in November 2001.

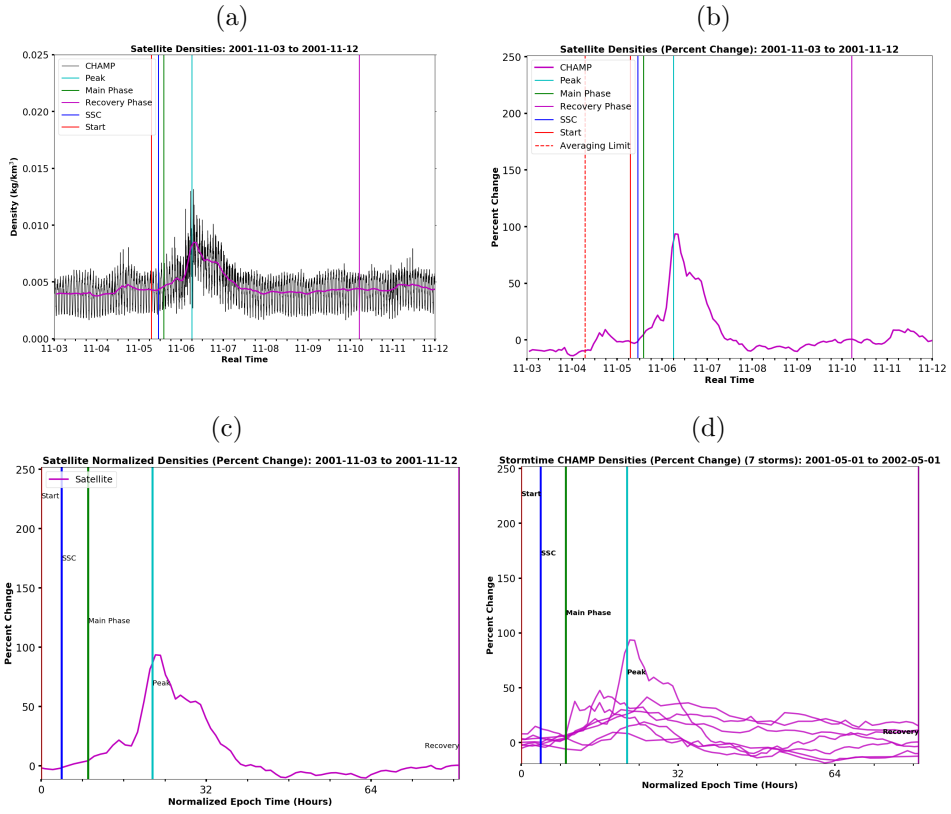

Figure 3.4: CHAMP densities throughout the SEA process: (a) from the accelerometer for one storm, (b) orbit-averaged for one storm, (c) along a normalized timeline for all storms, (d) for all storms superimposed.

of the densities for each storm are found and set displayed as to show the variation in the data used to construct the superposition.

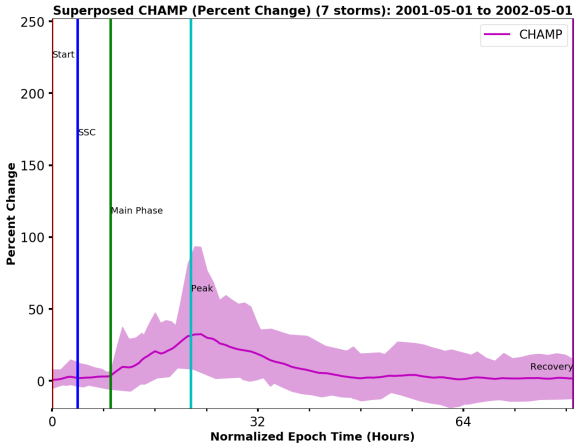

Figure 3.5: Superposed CHAMP densities and phases for 7 storms.

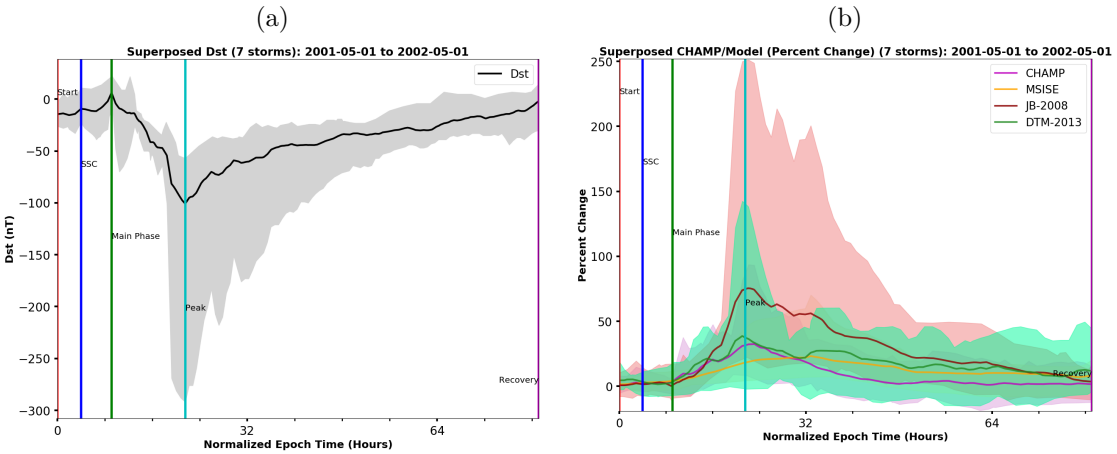

Figure 3.6: Superposed Dst (a) and CHAMP and model densities for 7 storms (b).

In order to compare the performance of each model with the behavior of the satellite data, with an eye towards future calibration techniques, the peak orbit-averaged density per storm may be plotted as a function of peak Dst, for all of the storms involved in the superposition, and a line fitted to the data. This allows responsiveness during the height of the storm as a function of Dst to be compared between all the models in comparison to the satellite data (Figure 3.7).

The peak densities from each model for each storm can also be graphed as a function of peak densities from the satellite, in order to compare how tightly they are correlated in comparison to unity. Figure 3.8 shows an example of this for the 7

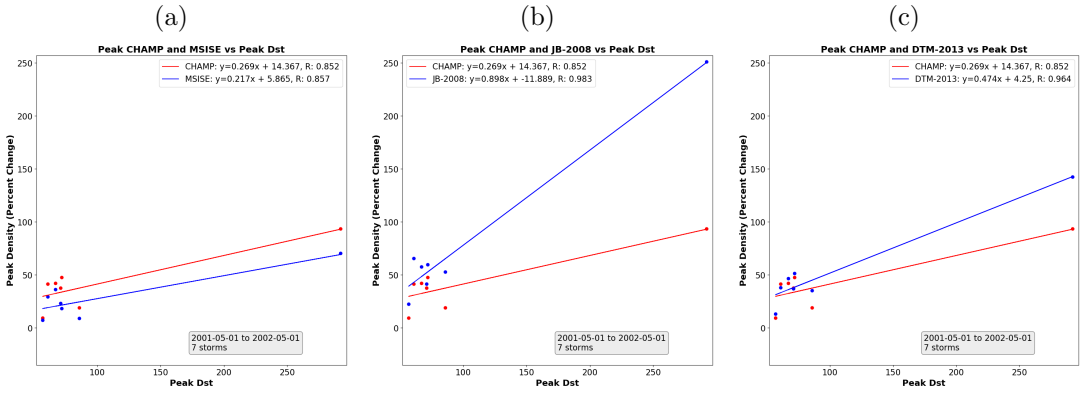

Figure 3.7: Peak ρ vs peak Dst for 7 storms for (a) MSIS-00, (b) JB-2008, and (c) DTM-2013.

storms collected between 2001-05-01 and 2002-05-01.

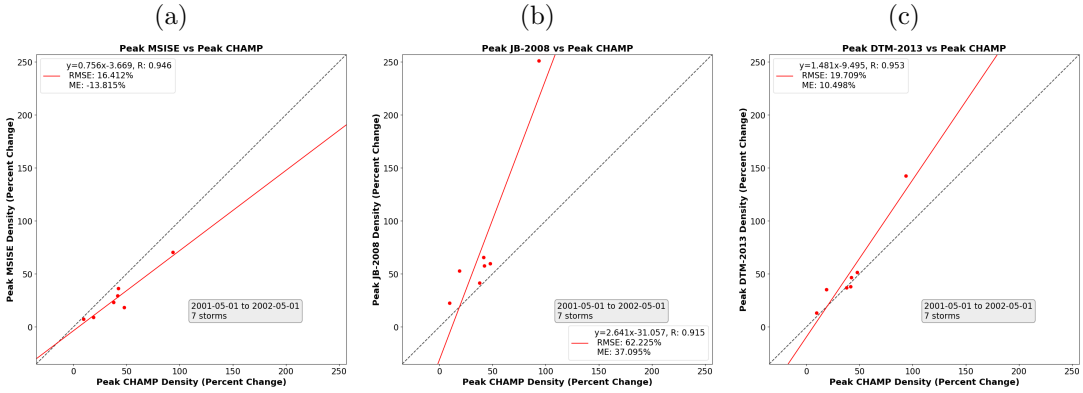

Figure 3.8: Peak model ρ vs peak CHAMP ρ for 7 storms for (a) MSIS-00, (b) JB-2008, and (c) DTM-2013.

The overall bias of each model in comparison to the satellite data may be specified with the RMS (Equation 2.1) or the Mean Error (ME) given by,

$$\text{ME} = \frac{\sum_{i=1}^{n} y_i - x_i}{n}, \tag{3.12}$$

where y_i is the i-th model density, x_i is the i-th satellite density, and n is the number of model-satellite density pairs considered. Just considering 7 storms over the span of a year shows that JB-2008 and DTM-2013 have an overestimation bias during the

height of storms, while MSIS has an underestimation bias. An increased number of considered storms, and more restrictions on the selection of storms, not only by intensity but also by peak F10.7 (or the value of any other geomagnetic indices such as a_p or IMF B_z or B_y) will allow for further investigation of model performance as a function of geomagnetic conditions. Results for an SEA study conducted along the CHAMP orbit for just over 9 years worth of data follows.

3.3 Results

Storms of varying levels of intensity were gathered between 2001-05-01 and 2010-08-31. A total of 138 storms were found. Of these storms, 96 were rejected and 42 were determined as usable by the selection criteria specified in Section 3.2.3. Of the usable storms, 3 were of weak intensity, 32 were of moderate intensity, 4 were of strong intensity, 2 were of severe intensity, and 1 was of extreme intensity. Of the 96 rejected storms, 36 were rejected due to having multiple peaks, 19 were rejected due to the SSC being within an hour of the main phase, 14 were rejected due to being preceded by a magnetospheric disturbance of moderate intensity or greater, and 9 were rejected due to having no SSC. Additionally, two storms occurring between 2001-11-21 and 2001-11-30 were neglected due to a large density data gap for CHAMP, and 13 storms occurring during 2004 were discarded due to poor modeling performance by JB-2008, which showed difficulty modeling densities during 2004, most likely due to an issue with its underlying Dst database for that year.

Superposition of the normalized storm-time orbit-averaged densities for CHAMP and all of the models (Figure 3.9) revealed different distinctions in model performance than in Figure 3.6.

The duration of the normalized epoch timeline for the superposition of 42 storms of varying intensities was ∼90.71 hours. The superposed Dst for all of the storms showed degree of spread in the values of Dst for each storm, with the least intense peak

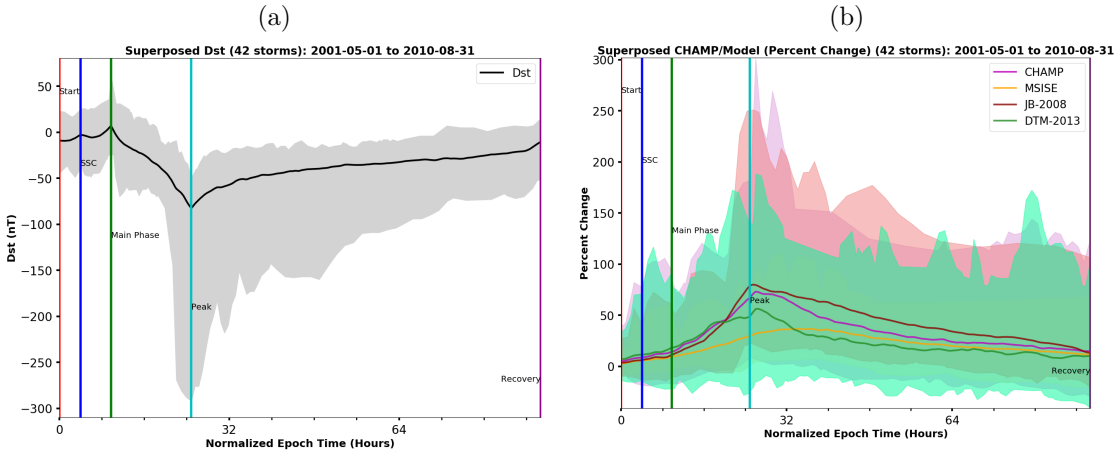

Figure 3.9: Superposed Dst (a) and CHAMP and model densities for 42 storms (b).

value near −30 nT, and the most intense peak value near −300 nT. The dominance of storms of moderate intensity among those considered contributed to the (mean) superposed Dst values peaking at approximately −75 nT.

What is clearly observable in the superposed density results is that each model performed well in comparison to CHAMP between the Start of the storms and the Main Phase, but thereafter, model performance diverged starkly. From the main phase to the peak of the storms, MSIS-00 underestimated the density response and in fact displayed a characteristic delay on the order of ∼12 hours between the satellite peak density response and its own peak density response. JB-2008 showed no delay, while delays for DTM-2013 and CHAMP were on the order of 1-2 hours. While JB-2008 and DTM-2013 displayed better performance than MSIS-00 leading up to the peak, DTM-2013 fell short in comparison to JB-2008, underestimating the overall peak density response compared to CHAMP by ∼20%, whereas JB-2008 overestimated the overall peak density response by <10%. During the recover phase MSIS-00 and DTM-2013 traded places, so to speak, such that while both underestimated the density response, MSIS-00 was closer to CHAMP throughout the entire recovery phase than DTM-2013, though not by much. In contrast, JB-2008 overestimated the density response during the entirety of the recovery phase, with the largest overestimation occurring

32 and 64 hours along the normalized epoch timeline.

Comparing the peak density response of each model to peak Dst, with CHAMP as the control (Figure 3.10), showed that DTM-2013 performed most similar to the CHAMP data, with a slope of 0.44 compared to 0.264 for CHAMP. JB-2008 showed the strongest peak density response to peak Dst, with a slope of 0.754, and a correlation of R∼0.772, a correlation stronger than that of the CHAMP data itself (R∼0.215), as well as DTM-2013 (R∼0.425) and MSIS-00 (R∼0.197). MSIS-00 showed both the smallest response (slope of 0.091) and weakest correlation between peak density and peak Dst.

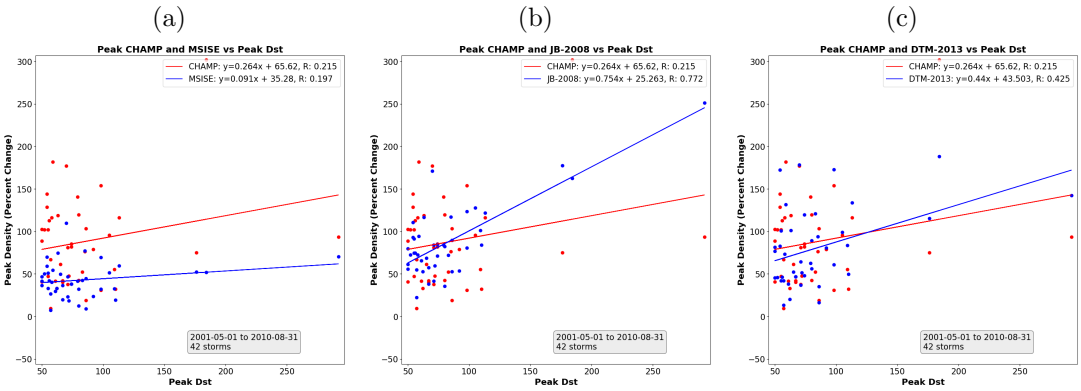

Figure 3.10: Peak ρ vs peak Dst for 42 storms for (a) MSIS, (b) JB-2008, and (c) DTM-2013.

Fitting linear relations to peak model density and peak satellite density allow more insight to be gained for each model (Figure 3.11). DTM-2013 distinguished itself as most closely modeling the peak CHAMP densities across all storms, with a model-satellite slope (correlation) of 0.618 (0.734), compared to 0.434 (0.547) for JB-2008 and 0.232 (0.619) for MSIS-00. The DTM-2013 results also showed the smallest RMS error value (37.576%) compared to JB-2008 (46.712%) and MSIS-00 (62.78%). Though the DTM-2013 results gave the best model-satellite slope for peak density response as well as the smallest RMS error, JB-2008 showed the smallest mean error compared to CHAMP, with a value of 0.187%, compared to -7.554% for DTM-2013

and a notable -44.725% for MSIS-00.

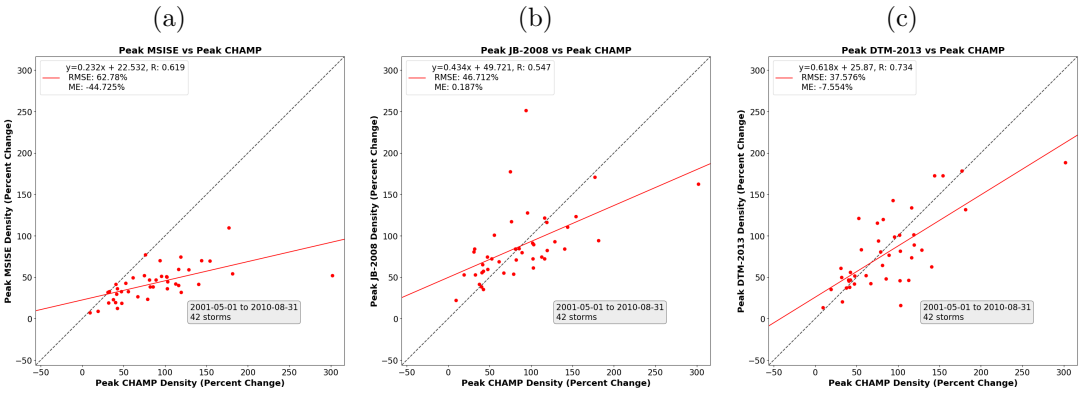

Figure 3.11: Peak model ρ vs peak CHAMP ρ for 42 storms for (a) MSIS-00, (b) JB-2008, and (c) DTM-2013.

3.4 Conclusion

SEA of the three most prominent empirical thermosphere density models for 42 storms of varying intensities has revealed important trends in modeling of the storm-time density response, highlighted by overestimation by JB-2008, mild underestimation by DTM-2013 and severe underestimation by MSIS-00, with DTM-2013 distinguishing itself as showing the most favorable performance across all storms considered. The incorporation of Dst into the underlying parameterization of JB-2008 is a likely factor for its noteworthy overestimation, and may suggest a disproportionate reliance of the model on Dst to model storm-time dynamics. The results also indicate that JB-2008's lower mean error is more a result of its greater variance in peak density modeling in comparison to DTM-2013, which statistically overall can be described as exhibiting the most favorable storm time performance. Given the varying degrees of correlation between peak model density and peak Dst for all of the models, a Dst-based density calibration scheme may not result in the same degree of model improvement for each model, especially depending on the intensity of the storm. Dst-

based scale factor corrections to the density may be derived by taking ratios between the peak densities obtained from CHAMP, GRACE, GOCE or Swarm and JB-2008 or MSIS-00, and related to peak Dst. The effectiveness of this as a coarse density calibration method should be explored for storms of varying intensities, given that only of strong or greater intensity were studied here.

Additional work should investigate how the percent change by model differs in each storm phase as a function of storm intensity, as well as studying the e-folding recovery time for densities from each model in comparison to satellite data for a variety of storms, as well as comparing those recovery times to the e-folding recovery time of the Dst. The latter analysis, which does not require storms to with a SSC, allows for investigating how the models perform for both CME- and CIR-driven geomagnetic storms of varying intensities. The delay between the peak Dst and the peak density should also be investigated in order to determine how and if each model shows different delays by storm type and intensity; this is particularly important for MSIS which seems to show a delay on the order of $\sim$12 hours compared to merely 1-2 hours for CHAMP data and densities modeled by JB-2008 and DTM-2013. Model accuracy should also be assessed by storm phase.

Future work should not only involve SEA conducted across a wide variety of storm intensities, but also involve additional storm selection criteria that distinguish storms based on peak F10.7, to determine the viability of calibration methods involving several scale factors to the density. In this respect, it may be possible to determine, based on the peculiarities of the parameterization of each density model, which solar or geomagnetic indices most effectively serve as SEA-driven calibration tools for improved storm-time density modeling, and under what conditions. This analysis should be extended to a wider variety of times, in order to perform comparative SEA on storms throughout the solar cycle, to determine biases in each empirical model related to their annual, semiannual, and solar cycle contributions. The analysis also ought to

be conducted along the orbits of satellites of varying altitudes, in order to determine the relevance of altitudinal biases in storm-time density performance. Lastly, the feasibility of an "ensemble" approach should be investigated, involving the averaging of the results of all of the model densities together to see how well such a method accounts for the shortcomings of each, and where and when such an approach shows the most success. Ensemble methods should involve the averaging of pairs of models as well as all three models considered, and performance should again be assessed by storm type, phase, and intensity.

Overall, SEA serves as a powerful tool for uncovering the nuances of thermospheric model performance. In condensing model outputs to a uniform timeline, it allows for the amplification of characteristic patterns in model behavior that reveal possible avenues for calibration through use of highly-accurate accelerometer or GPS-derived densities as a control. This supplies the space research community with a powerful investigative tool that can serve to benefit satellite mission operations, space situational awareness, and thermospheric model development. The next chapter focuses on how satellite measurements can aid model development in the context of thermospheric horizontal winds.

CHAPTER IV

Thermospheric Horizontal Wind Modeling

This chapter focuses on validating winds from the Global Ionosphere Thermosphere Model (GITM) as compared to measurements made by the Gravity Field and Steady-State Ocean Circulation Explorer (GOCE) satellite. Winds are a critical component to any physics-based model, since they advect density, composition changes, momentum, and energy across the globe. Therefore, it is important to understand the model's ability to simulate the winds in order to fully understand possible reasons for other deficiencies or strengths in the model.

An introduction to the importance and current understanding of thermospheric horizontal winds is presented, followed by a statistical study of model-data comparisons of cross-track (horizontal) thermospheric wind (V_x) between those computed by the Global Ionosphere-Thermosphere Model (GITM) and accelerometer-derived cross-track winds obtained from the Gravity Field and Steady-State Ocean Circulation Explorer (GOCE) satellite. GITM was used to model winds along the GOCE orbit from January to November 2013. Probability distributions of the GITM and GOCE winds were computed, and compared in the mid-, auroral, and polar latitudes for low, moderate, and high geomagnetic activity, as represented by the AE. Furthermore, the winds were distributed over bins of AE, MLAT, MLT, DOY, and F10.7, in order to characterize how GITM V_x responds to these different parame-

ters, and compare that responsiveness to that of the GOCE data. Histograms are presented instead of a point-by-point comparison in order to simply determine if the wind speeds have the correct statistical behavior, as opposed to whether they are simulated with the exact right speed at the exact right location. First, observation methods of thermospheric horizontal winds are reviewed and a brief history of thermospheric wind modeling presented, followed by a description of the methods of the analysis, its results, and a conclusion with implications for future work.

4.1 Thermospheric Winds

Horizontal winds are a critical component of circulation within the thermosphere. They transport gradients in density, composition, and temperature, and the wind itself across the globe (*Rodrigo et al.* 1981 and *Kazimirovsky et al.* 1999), and are primarily driven by daily variations in solar EUV radiation (*Roble* 2003). Divergence and convergence of horizontal winds can also drive vertical flows, density and composition changes, and changes in temperature (*Rishbeth et al.* 1969, *Biondi* 1984a, and *Fejer et al.* 2000). Interaction of the neutral winds with the ions can drive frictional heating and momentum transfer through ion drag, as well as field-aligned ion flows (*Guo et al.* 2018). Ion drag in particular is governed by the collision frequency of ions and neutrals, Acceleration due to ion drag is governed by the following equation (*Rees* 1989):

$$\frac{\mathrm{d}V_n}{\mathrm{d}t} = \nu_{\mathrm{ni}} \left(u_i - u_n \right) \tag{4.1}$$

where ν_{ni} is the ion-neutral collision frequency, u_i is the speed of the ions, and u_n is the speed of the neutrals. Equation 4.1 is then included in the linear momentum equation, which can be written as follows:

$$\frac{Du_n}{Dt} = -\frac{1}{\rho}\nabla p - 2\Omega \times u_n + \frac{1}{\rho}\nabla\left(\mu \nabla u_n\right) + \nu_{\mathrm{ni}}\left(u_i - u_n\right) \tag{4.2}$$

where the left-hand side is the local derivative $\frac{D}{Dt} = \frac{\partial}{\partial t} + U \cdot \nabla$, ρ is the neutral density, p is pressure, Ω is the Earth's rate of rotation, and $\mu$is the viscosity coefficient. The first term on the right-hand side is the pressure gradient, the second term the Coriolis force, the third term the viscosity, and the last term the ion-drag. If the ion-neutral collision frequency is sufficiently great, and if the ion drift is sufficiently large and acts over a sufficient length of time, the circulation of the neutral gas will begin to mirror that of the ionospheric plasma, especially during substorms.

Winds can also push ions across geomagnetic field lines, driving electrodynamical changes in the F-region ionosphere (*Billett et al.* 2020), specifically by inducing electron density variations at various temporal and spatial scales (*Titheridge* 1995). During geomagnetic storms, momentum advection becomes dominant, the pressure gradient force is enhanced, and ion drag is modified such that altitudinal variations in the horizontal wind are induced, causing large vertical shears (*Burnside et al.* 1991 and *Wang et al.* 2008). These shears can also be generated by gravity waves (*Millward et al.* 1993).

4.2 Thermospheric Wind Measurements

4.2.1 Specular Meteor Radars

The horizontal wind itself, has customarily been observed or derived from specular meteor radars, Fabry-Perot Interferometers (FPIs), Doppler lidars, and satellite accelerometer data, It has been modeled with both empirical and physics-based models. Specular meteor radars detect plasma trails from incoming meteors when their paths lie perpendicular to the radar beam (*Ceplecha et al.* 1998). Measurement of the average Doppler shift of gases in the plasma trail allows an observer to infer neu-

tral wind speeds along the radar's line of sight, providing an inexpensive means of generating a dataset of winds. Historically, small interferometric broadband radars have been used to obtain winds and temperatures using this method (*Hocking et al.* 2001), and generally are limited to obtaining measurements between ∼80-100 km in altitude (*Chau et al.* 2021), as demonstrated by the SKiYMET meteor radar (*Korotyshkin et al.* 2019). Recent developments in meteor radar techniques have enabled use of large radars that track reflections from plasma irregularities that develop from many meteor trails, instead of following a single trail, and have yielded observations showing wind speeds in excess of 100 m/s between 93 and 110 km using a large Very High Frequency (VHF) radar (*Oppenheim et al.* 2000 and *Oppenheim et al.* 2009). Improvements in calibration and detection techniques have also granted the capability of deriving useful information from nonspecular meteor trails (*Zhao et al.* 2011) and observations from multilink configurations where the radar receivers are not located at the same location as the transmitters (*Chau and Clahsen* 2019). While meteor radars can produce high-resolution observations of horizontal winds (Figure. 4.1), they are limited to the upper mesosphere and lower thermosphere.

4.2.2 Fabry-Perot Interferometers

FPIs are also widely-used to obtain thermospheric wind and temperature measurements with airglow emissions at 630.0 nm being collected by the instrument and multiply reflected through a series of lenses to create an interference pattern (Figure 4.2). The broadening function determined from the interference pattern allows the estimation of the temperature of the emitting species (*Killeen and Hays* 1984), and Doppler shifts of the interference fringes allow for the determining of wind speed (*Shiokawa et al.* 2012). FPIs have been specifically used to show the relationship between horizontal convergence/divergence, and changes in the vertical flow (*Biondi and Sipler* 1985). The horizontal vector winds can be obtained by observing the same

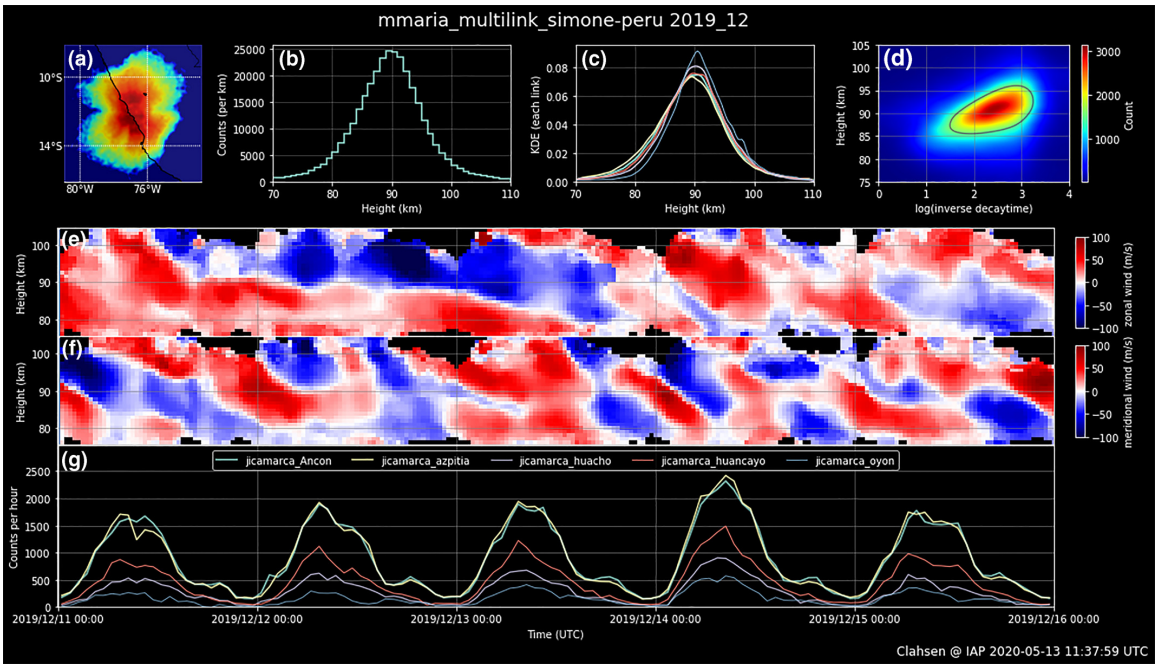

Figure 4.1: SIMONe meridional and zonal winds (e and f) (*Chau et al.* 2021).

thermospheric volume at orthogonal look directions from two sites.

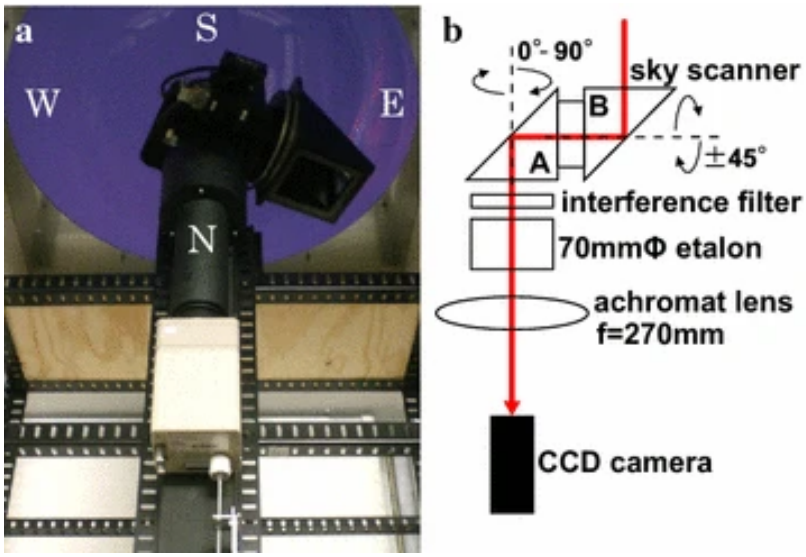

Figure 4.2: Interferometer photo and schematic (*Nakamura et al.* 2017).

Due to the fact that there is no absolute measurement, just relative changes in the ring pattern spacing from measurement to measurement, it is conventional to assume a vertical zero-wind reference measurement (*Makela et al.* 2013 and *Biondi*

1984b), and/or use a stable calibration source, such as a frequency-stabilized He-Ne laser (*Makela et al.* 2012) to track instrumental calibration effects through the night. Under geomagnetically quiet conditions in the midlatitudes, FPI measurements routinely show wind speeds up to 50 m s^{-1} in the zonal direction and up to 100 m s^{-1} in the meridional direction (*Jiang et al.* 2018). FPI measurements have shown increased zonal flow and more negative meridional flow as a function of increasing altitude, as well as greater absolute wind speeds during the winter (*Yuan et al.* 2013). They have also been used to study the impact of gravity waves and atmospheric airglow on wind velocity observations in comparison to those obtained with radar techniques (*Fujii et al.* 2004). FPIs have also been installed aboard satellites, such as the UARS (*Khattatov et al.* 1997) the TIMED satellite (*Killeen et al.* 2006), where they were used to study diurnal and semidiurnal tides. Unfortunately, some drawbacks of relying on ground-based FPIs include the limited spatial distribution of measurement stations, the requirement of nighttime clear-sky conditions, the choice for a zero Doppler baseline (*Anderson et al.* 2012, and *Aruliah and Rees* 1995), and errors in measurements due to atmospheric scatter (*Harding et al.* 2017). Recently, *Wu et al.* 2012 flew an FPI on a balloon to overcome some of these limitations.

4.2.3 Doppler Lidars

Doppler lidars have been used to study wind and temperature in the mesopause region by detecting the Doppler shift of atomic spectral lines of mesospheric metals such as Na (*Bowman et al.* 1969, *fang Du et al.* 2017 and *Philbrick et al.* 2021). This technique, which uses similar principles to the FPI but uses visible wavelengths (Figure 4.3), has seen most applicability using broadband lidars to observe the mesopause region and below, but notable observations of the existence of detectable metals within the lower thermosphere (*Gardner et al.* 1999, *Chu et al.* 2011, and *Gao et al.* 2015) and the usage of a narrow-band Lidar has allowed for observation of winds up to

140 km using this method, and have been shown to be consistent with past rocket measurements (*Liu et al.* 2016a). While FPIs are passive in that they rely on the natural airglow to provide the signal, Lidars are active, and shoot a laser into the atmosphere and measure the return signal's doppler shift and doppler broadening.

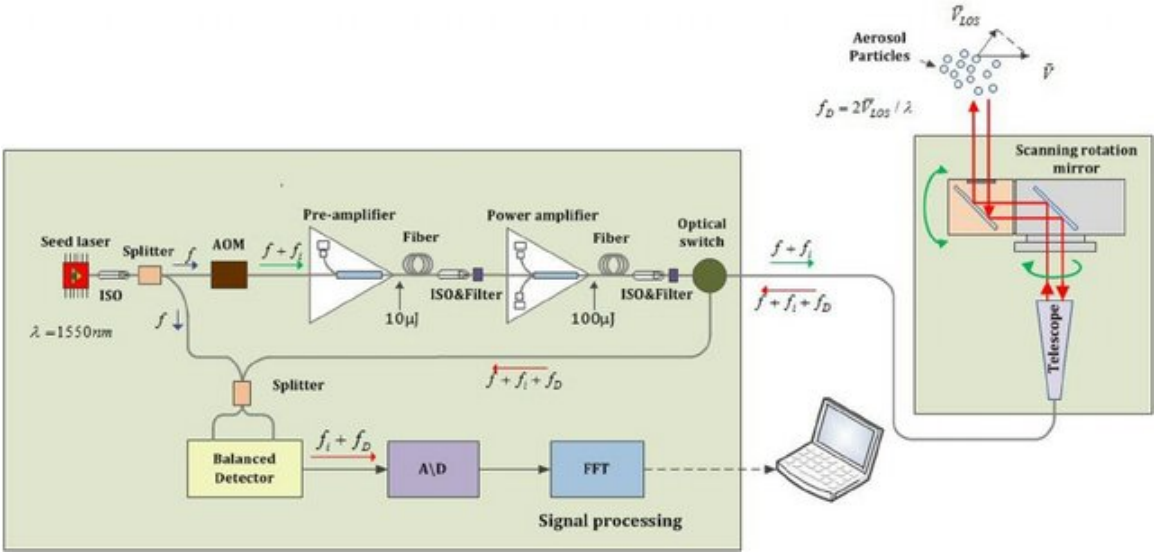

Figure 4.3: A schematic of the pulsed coherent Doppler lidar system (*Wu et al.* 2014).

4.2.4 Satellite Accelerometers

LEO satellites are another source from which thermospheric wind measurements may be obtained. Before the CHAMP satellite, wind measurements on satellites were mostly made with FPIs. The DE-2 satellite had both an FPI and an *in-situ* wind sensor (*Spencer et al.* 1982a). The GOCE satellite (Figure. 4.4) is a prominent example of a spaceborne source of horizontal wind data (*Floberghagen et al.* 2011). The satellite was launched on 17 March 2009, used an ion thruster to sustain its orbit at ∼250 km at 96.7° inclination, and it reentered the Earth's atmosphere on 11 November 2013. GOCE's main payload was the Electrostatic Gravity Gradiometer (EGG), a set of six 3-axis accelerometers mounted in a diamond configuration. The accelerometers of the EGG were 100 times more sensitive than any others previ-

ously flown, such as the SuperSTAR accelerometer onboard the GRACE spacecraft (*Touboul* 2003b). GOCE accelerometer data have been used to investigate the wave coupling between the lower and middle thermosphere (*Gasperini et al.* 2015), probe the mechanisms driving an eastward wind jet in the evening sector and westward wind jet in the morning sector as well characterizing seasonal variation of the wind (*Liu et al.* 2016b), and improve handling of the energy accommodation coefficient to reduce discrepancies when compared to ground-based measurements (*Visser et al.* 2019a).

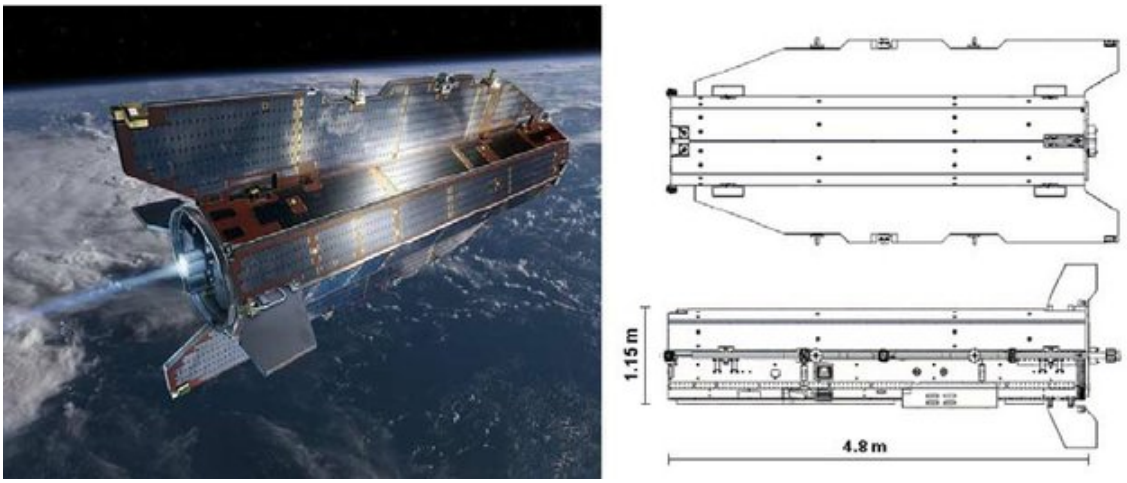

Figure 4.4: An impression (left), and schematic (right) of the GOCE spacecraft (*Romanazzo et al.* 2013).

Cross-track (horizontal) wind along the GOCE orbit was derived from its accelerometer measurements by using them to determine the net force and torque acting on the satellite. Models described in *Doornbos* 2011 and *Visser et al.* 2018 were combined with measurements and housekeeping data to estimate the forces and torques on the spacecraft caused by the gravity gradient, magnetic attitude control, and other equipment. The residual force and torque was found by subtracting the model output from the measurement. This residual force and torque was assumed to be entirely aerodynamic, and an aerodynamic model was constructed to match it by changing the direction of the incoming flow. The wind vector was thus defined as the

difference between the incoming flow and the orbital plus co-rotation velocities. The acceleration due to drag on the spacecraft can then be written in the following form:

$$\vec{a} = -\frac{1}{2}\rho\frac{A}{m}C_D\left(\vec{v_o} - \vec{v_w}\right)^2\left(\widehat{v - v_w}\right) \tag{4.3}$$

where the ρ is the local thermospheric density, A is the spacecraft cross-sectional area, m is the spacecraft mass, C_D is the drag coefficient, $\vec{v_o}$ is the orbital velocity of the spacecraft, and $\vec{v_w}$ is the velocity of the thermospheric wind, which includes velocities in the along-track, cross-track, and cross-vertical directions, including co-rotation. It is extraordinarily difficult to separate changes in ρ vs changes in $v_o - v_{\text{along}}$, so it is customary to assume that v_{along} is negligible given that $v_o >> v_{\text{along}}$. This algorithm is described in detail in *Visser et al.* 2019a. By reason of the overall focus on satellite observations being used to improve thermospheric modeling, and due to the high accuracy of the GOCE accelerometer and its coverage of middle thermosphere, the following study used its data as a baseline statistical comparisons.

4.3 Empirical Wind Modeling

Thermospheric winds have been studied with empirical models, the most prominent of which have been of the Horizontal Wind Model (HWM) family, a family of empirical thermospheric wind models.

HWM is a series of empirical thermospheric wind models that saw its first iteration with HWM-87, which generated modeled winds using thermospheric wind data obtained from the Atmospheric Explorer E and Dynamics Explorer 2 satellites, using a limited set of spherical harmonics (*Hedin et al.* 1988). It however was limited to the upper thermosphere (specifically above 220 km), and was unable to detect solar cycle effects due to F10.7, though it did include magnetic activity effects. HWM-87 was succeeded by HWM-90, a revision which improved modeling capabilities by includ-

ing ground-based FPI and ISR data, extended down to 100 km, added solar activity dependence, and improved spatial and temporal resolution (*Hedin* 1991). HWM-93 added further improvements by incorporating midlatitude radar data, rocket soundings, and winds inferred from mean density and temperature gradients, extending performance down to the terrestrial surface (*Hedin et al.* 1996). HWM-07 would later extend from the ground to the exosphere (∼500 km), incorporating over 50 years of satellite, rocket, and ground-based wind measurements, and being split into two components: a quiet-time component for the background state of the thermosphere, and a geomagnetic storm time component (DWM-07) (*Drob et al.* 2008 and *Emmert et al.* 2008). HWM-14 represents the most recent update, incorporating cross-track winds from the GOCE satellite and new data from ground-based 630 nm FPIs (*Drob et al.* 2015).

4.4 General Circulation Models

Several physics-based Global Climate Model (GCM) models have also seen development, including those developed at National Center for Atmospheric Research (NCAR), at University College of London (UCL), and lastly, at the University Michigan. Those developed by NCAR began with the Thermosphere General Circulation Model (TGCM), which modeled neutrals only, and was valid between 90-500 km (*Dickinson et al.* 1981). Subsequent iterations saw the addition of ions and treating major species separately (*Roble et al.* 1988), adding self-consistent wind-generated electric fields at middle and low latitudes (*Richmond et al.* 1992), and extending down to 30 km and adding middle atmosphere chemistry (*Roble and Ridley* 1994b).

Physics-based models developed at UCL saw their initial manifestation with Coupled Thermosphere-Ionosphere Model (CTIM), which included a self-consistent ionosphere at mid and high latitudes (*Fuller-Rowell et al.* 1996). Later iterations included a self-consistent low-latitude ionosphere and inner magnetosphere (*Millward. et al.* 1996),

addition of self-consistent mid and low latitude electric fields (*Millward et al.* 2001), and extension down to 30 km and the addition of middle atmosphere physics and chemistry (*Harris et al.* 2002).

GITM represents a more recent addition to the family of physics-based models distinguishing itself with adjustable resolution and use of an altitude grid instead of a pressure grid. It is described in the next section.

4.5 The Global Ionosphere Thermosphere Model

GITM (*Ridley et al.* 2006) is a three-dimensional, spherical, and parallel code that models the thermosphere-ionosphere system from 100-600 km and uses a stretched altitude grid in latitude and altitude. It includes a modern advection solver and realistic source terms for the continuity (Eq. 4.5), momentum (Eq. 4.6), and energy equations (Eq. 4.7), which are given as:

$$\rho = \Sigma_s M_s N_s$$
$$\Upsilon = p/\rho \tag{4.4}$$

$$\frac{\partial N_s}{\partial t} + N_s \nabla \cdot \mathbf{u} + \mathbf{u} \cdot \nabla N_s = S_c \tag{4.5}$$

$$\frac{\partial \mathbf{u}}{\partial t} + \mathbf{u} \cdot \nabla \mathbf{u} + \nabla \Upsilon + \frac{\Upsilon}{\rho} \nabla \rho = 2\Omega \times \mathbf{u} - \frac{1}{\rho} \nabla \left(\mu \nabla \mathbf{u} \right) + \nu_{\mathrm{ni}} \left(u - v_i \right) \tag{4.6}$$

$$\frac{\partial \Upsilon}{\partial t} + \mathbf{u} \cdot \nabla \Upsilon + (\gamma - 1) \, \Upsilon \nabla \cdot \mathbf{u} = \Sigma Q \tag{4.7}$$

where, u is the horizontal velocity, ρ is total mass density, N_s is number density of the individual species s, Υ is the normalized temperature, p is total neutral pressure, $\mathbf{u}$ is the neutral velocity, t is time, γ is the ratio of specific heats $\left(\frac{5}{3}\right)$, Ω is the Earth rotation rate, μ is the viscosity coefficient, ν_{ni} is the ion-neutral collision frequency, v_i

is the neutral speed, and ΣQ is the sum of frictional heating, heat transfer between ions and neutrals due to elastic collision, energy transfer via conduction, and energy input from EUV and chemical processes (*Zhu et al.* 2016).

GITM solves explicitly for the neutral densities of nine neutrals (O, O_2, N(^{2}D), N(^{2}P), N(^{4}S), N_2, NO, H, and He), neutral, ion, and electron temperatures, the bulk horizontal neutral winds, the vertical velocity of the individual neutral species and the ion and electron velocities, solving the momentum equations, allowing for the capability of modeling problems for which the hydrostatic approximation is inaccurate. The code can use a dipole magnetic field, a tilted dipole, or the International Geomagnetic Reference Field (IGRF) magnetic field (*Maus et al.* 2005) with the APEX coordinate system (*Richmond* 1995). The primary drivers of the thermosphere and ionosphere in GITM are solar EUV radiation modeled by FISM (*Chamberlin et al.* 2007b and *Chamberlin et al.* 2008), and high-latitude electrodynamics, specified by the *Weimer* 2005 electrodynamics potential patterns driven by time-delayed IMF and solar wind measurement from the Advanced Composition Explorer (ACE) satellite, and the *Fuller-Rowell and Evans* 1987 particle precipitation patterns driven by hemispheric power estimated by LEO satellites operated by NOAA. GITM can be initiated using the MSIS model (*Hedin et al.* 1991) and the International Reference Ionosphere (IRI) (*Bilitza* 2001) neutral and ion densities and temperatures.

GITM has been used to study the role of ion convection in the high-latitude ionospheric plasma distribution, where it showed enhanced horizontal convection and vertical advection above 450 km in response to electric field enhancement (*Deng and Ridley* 2006b). It has also been used to investigate zonal differences in the electron density (N_e), where it showed that the zonal wind contributes to ~80% of the fraction of the observed longitudinal dependence of N_e (*Wang et al.* 2015), and it has been used to study day-to-day variability (weather) in the thermospheric winds in comparison to data collected by ground-based FPIs, where it was found to underestimate the

weather by ∼65% (*Harding et al.* 2019), as mentioned in Section 1.2.2. Additionally, GITM has been used to model winds over Alaska during a substorm (*Liuzzo et al.* 2015b), which occurs when energy from the magnetospheric tail is ejected into the high-latitude ionosphere (*Wang et al.* 2017 and *Cai et al.* 2019).

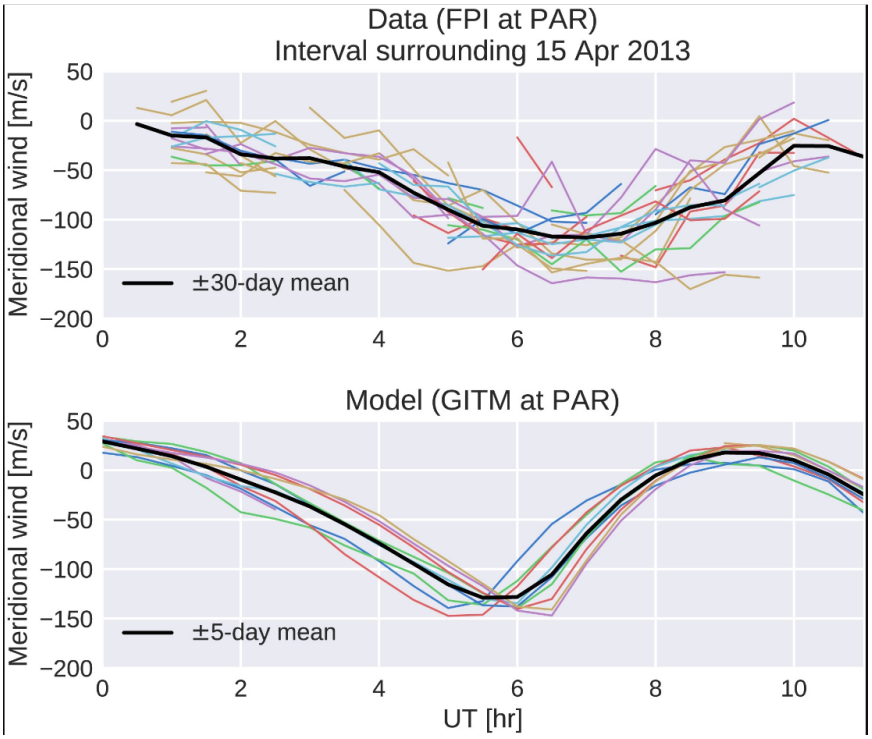

Figure 4.5: Meridional winds in GITM and from the PAR FPI (*Harding et al.* 2019).

To date, however, the horizontal winds in GITM have not been statistically validated. The following study presents one such initial evaluation, where winds modeled by GITM along the GOCE orbit are investigated in their dependencies on magnetic local time, magnetic latitude, season, and magnetic activity, and compared to the winds derived from the GOCE accelerometer, an approach that has only heretofore been applied to the standard deviation of the vertical wind $\sigma(V_z)$ in *Visser et al.* 2019b.

4.5.1 Methodology

GITM was with the parameters listed in Table 4.1, and high-latitude drivers from *Weimer* 2005 and *Fuller-Rowell and Evans* 1987, from January to November 2013 and results were extracted and data along the GOCE trajectory was extracted from the GITM simulations. The GOCE spacecraft was launched on March 17, 2009, and reentered the Earth's atmosphere on 11 November 2013. It had a circular, sun-synchronous orbit in low LEO at ∼270 km (decaying to ∼230 km by the mission's end), with an inclination of 96.6° (*Strugarek et al.* 2019), making it close to sun-synchronous, with a dusk ascending node, and dawn descending node.

Table 4.1: GITM Parameters for the Horizontal Wind Validation Study

Parameter	**Value**
Eddy Diffusion Coefficient	100
Eddy Pressure Lower	0.0050
Eddy Pressure Upper	0.0005
Photoelectron Heating Efficiency	0.02
Neutral Heating Efficiency	0.05
Thermal Conduction (Molecular)	3.6×10^{-4}
Thermal Conduction (Atomic)	5.6×10^{-4}
Thermal Conduction Power	0.69
AUSMSolver	True
CFL	0.80
Limiter	MC, 2.0
Dynamo High Lat. Boundary	45.0
Improved Ion Advection	True
Nighttime Ion B.C.s	True
Minimum TEC for Ion B.C.s	2.0

Given that he horizontal wind in GITM was extracted along the GOCE orbit, both the GITM results and the GOCE measurements have the same 10-second temporal resolution. As the GOCE cross-track wind measurements have associated errors, some measurements may constitute outliers in the data and be too uncertain. Therefore, for wind measurements in excess of 25 m/s, if the associated error was greater than 25 m/s and the absolute value of the GOCE cross-track wind measurement was less

than the associated error, the wind data were discarded.

Figure 4.6 shows 14 minutes of horizontal wind speed (magnitude of the cross-track wind, V_x) at different times on the first six days of March 2013 along the GOCE orbit, as representative examples of GITM's performance in comparison to the GOCE data. Each of the times chosen corresponded to the time for which the largest peak in the vertical wind (not shown) was observed in the GOCE data (Figure 5 in *Visser et al.* 2019c). On each day, the GOCE data show the horizontal wind rising to a crest, often featuring smaller peaks surrounding a dominant central peak. The small gaps in the GOCE cross-track wind measurements on March 2 and March 4 correspond to discarded data.

By inspection, GITM performed well in about half of the times, capturing the overall contour and magnitude of the horizontal cross-track wind speed on each day, especially on March 3 and March 5, though it did less well at capturing smaller features in the wind speed that occurred over shorter timescales than that of the central peak.

The statistical analysis of *Visser et al.* 2019c was followed for the analysis, and applied to the cross-track horizontal wind speeds (V_x). GITM V_x results were compared to GOCE V_x data in terms of their probability distributions calculated over bins with a width of 1 m/s. The means, 25th, and 50th percentiles were calculated for each distribution. The effects of several controlling parameters on the GITM and GOCE V_x data were compared: namely magnetic latitude (MLAT), magnetic local time (MLT), day-of-the-year (DOY), and geomagnetic activity. The minute-by-minute Auroral Electroject (AE) Index was used to quantify geomagnetic activity. AE is a measure derived from geomagnetic variations of the horizontal component of the terrestrial magnetic field at selected observatories within the auroral zone in the northern hemisphere (*Davis and Sugiura* 1966 and *Weygand et al.* 2014). Probability distributions in three magnetic latitude ranges were calculated: midlatitudes (30-60°),

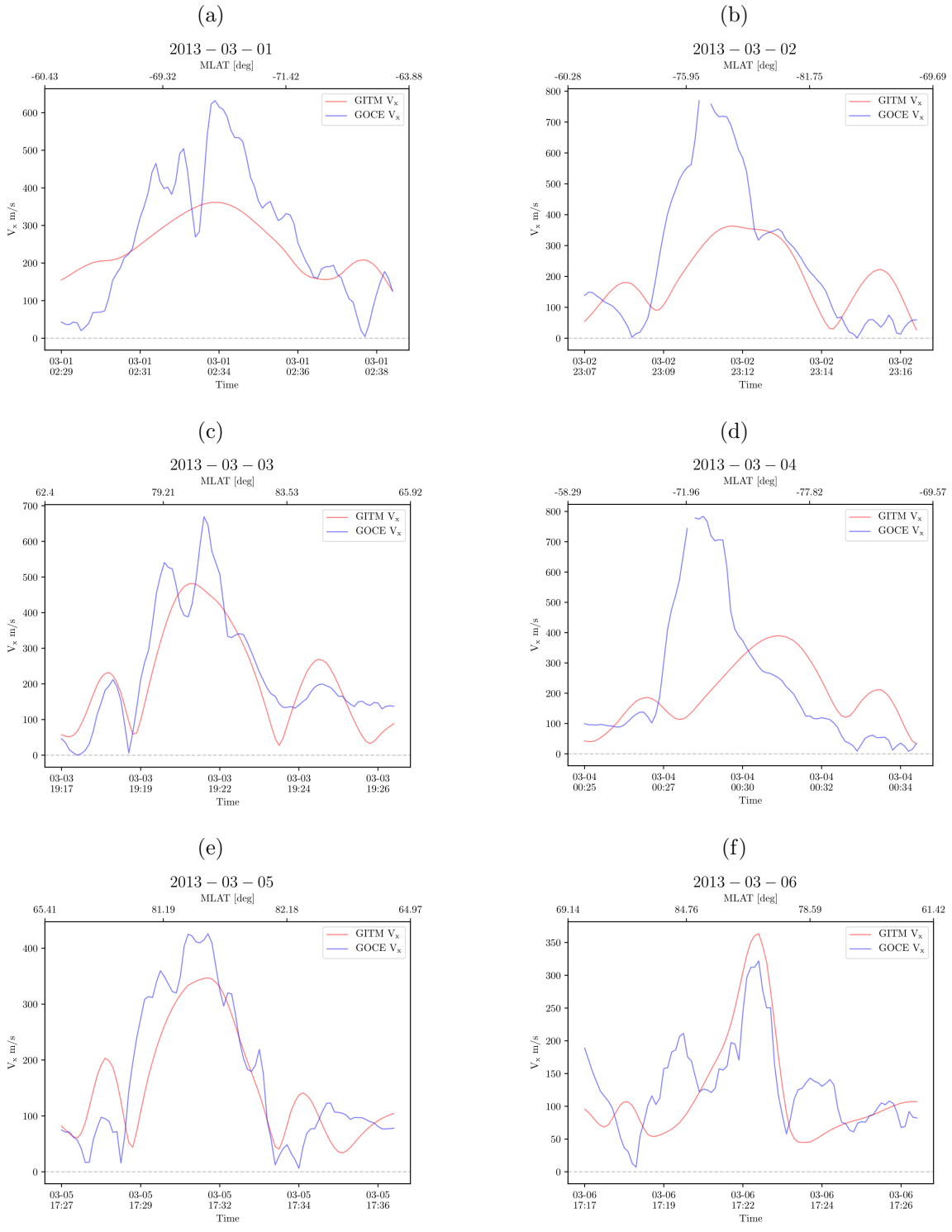

Figure 4.6: GITM and GOCE V_x surrounding notable peaks in the horizontal wind for the first 6 days of March.

auroral latitudes (60-80°) and polar cap latitudes (80-90°). As in *Visser et al.* 2019c and *Innis and Conde* 2002b, we further subdivided each MLAT bin according to the following AE bounds: AE≤250, 250<AE≤500, and AE>500.

In order to compare and contrast how GITM's V_x responded to different parameters, the method of *Visser et al.* 2019c was mirrored again, and the data were distributed over bins of AE, MLAT, MLT, DOY, and F10.7, and the 25th, 50th, and 75th percentiles of V_x were compared.

4.5.2 Results

Comparisons of the cross-track horizontal wind for GITM and GOCE for the entire time period considered are shown in Figure 4.7 for the dusk node and Figure 4.8 for the dawn node. The data are displayed as a function of time and MLAT rather than in geographic coordinates in order to minimize the effect of diurnal variation caused by the Earth's magnetic field rotating throughout the day. This has the consequence of resulting in a lack of data near the magnetic equator, which is due to the choice of using a reference altitude of 100 km for the MLAT, such that most of the time, GOCE, which orbited at ∼250 km, did not sample 0° magnetic latitude (i.e., magnetic field lines were traced from the GOCE location to 100 km and the magnetic latitude of that point was used). Both GITM and GOCE V_x showed greater speeds in the auroral region and lesser speeds in the midlatitudes, in both hemispheres and for both the ascending and descending nodes.

By inspection, GITM's demonstrated difficulty in capturing finer latitudinal structures in the horizontal wind, and placed a morphological feature at $\pm 20° - 30°$, coincident with location of the Equatorial Ionization Anomaly (EIA), a phenomenon caused by the removal of plasma from around the equator by the upward $\mathbf{E}\times\mathbf{B}$ drift creating an equatorial trough and two bounding crests of plasma within $\sim \pm 20°$ magnetic latitudes (*Balan et al.* 2018). GITM also struggled with capturing some of

(a) GITM Wind Speeds near Dusk

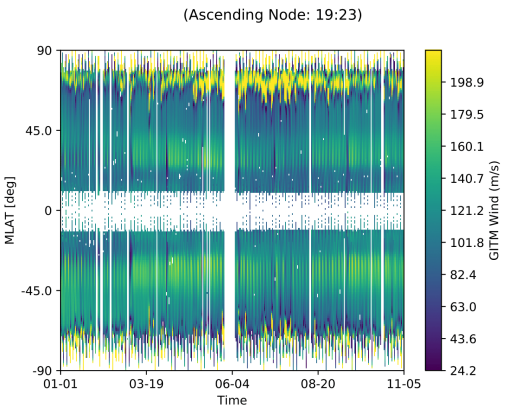

(b) GOCE Wind Speeds near Dusk

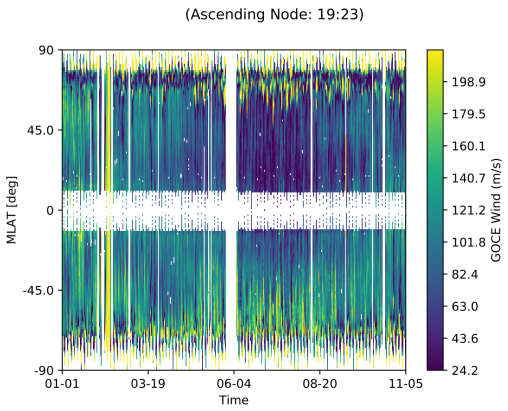

(c) Difference between GOCE and GITM Wind Speeds

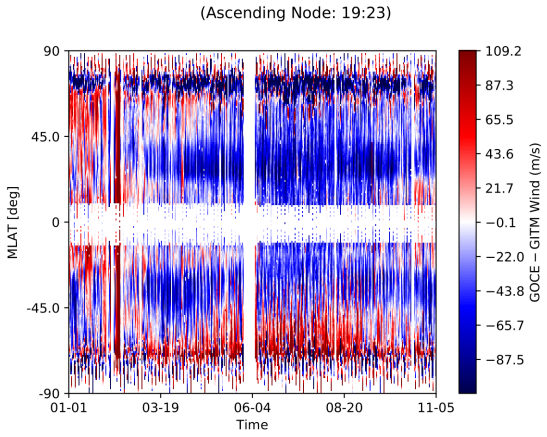

Figure 4.7: GITM (a) and GOCE (b) V_x, and differences between the two (c) in 2013 for the ascending (dusk) node.

the seasonal variation in the horizontal wind speeds shown in the GOCE data. This is most evident in the midlatitudes for the dawn node: For the descending (dawn) node, GOCE data showed that higher wind speeds begin to extend from the auroral to the equatorial region throughout the summer in the Northern Hemisphere, which GITM failed to capture, as it underestimated the winds during those times in that region. Conversely, for the ascending (dusk) node, during that same time period, GITM overestimated the horizontal winds in the same latitude region. For both the ascending and descending node throughout the entire year, GITM generally overes-

(a) GITM Wind Speeds near Dawn

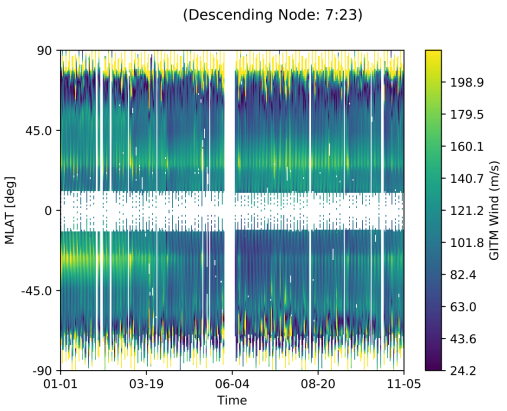

(b) GITM Wind Speeds near Dawn

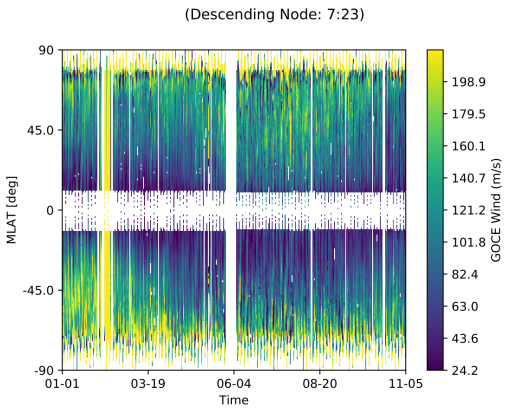

(c) Difference between GOCE and GITM Wind Speeds

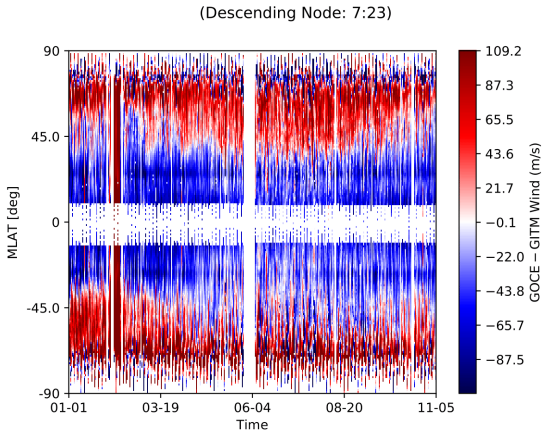

Figure 4.8: GITM (a) and GOCE (b) V_x, and differences between the two (c) in 2013 for the descending (dawn) node.

timated the horizontal wind speeds in the midlatitudes and the auroral latitudes in the Southern Hemisphere. Overall, GITM overestimated the wind speed for the dusk node most prominently during summer, and underestimated the wind speed for the dawn node most drastically during the height of summer in the northern hemisphere (Figure 4.7(b)).

Exploring V_x specifically during the first six days of March (Figure 4.9) shows the differences between GITM and GOCE in greater detail. GITM reproduces the diurnal variability of V_x shown in the GOCE data, but higher wind speeds in the

EIA region are again clearly visible, most likely due to ion drifts that are too strong. GITM's wind speeds are more similar to GOCE at high latitudes in the dusk sector, but GOCE wind speeds are larger in the southern auroral zone in the dawn sector.

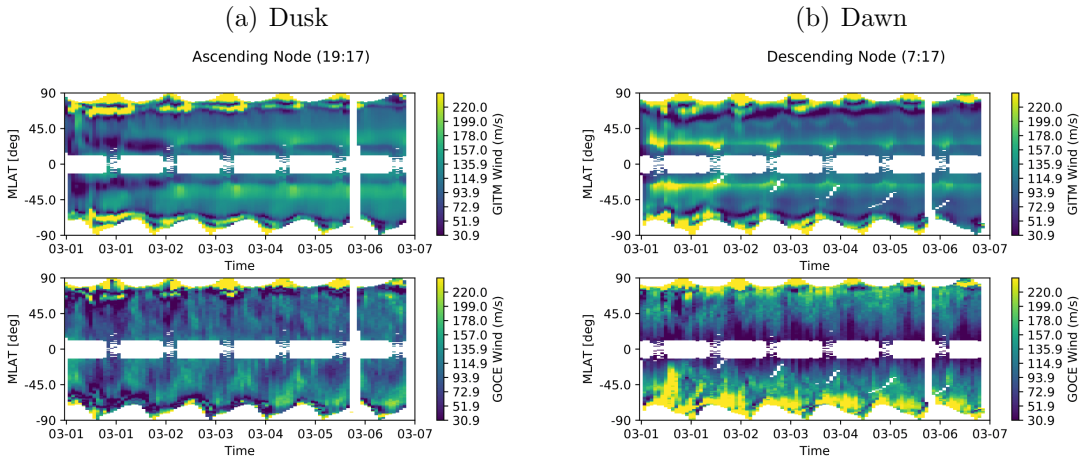

Figure 4.9: GITM and GOCE V_x for the beginning of March for the ascending (dusk) (a) and descending (dawn) (b) nodes.

Probability distributions of V_x for GITM and GOCE allow comparisons to be made as a function of the three latitude ranges and three categories of geomagnetic activity described by AE (Figure 4.10). GITM's probability distributions are generally narrower than those of GOCE outside of the polar region, especially in the midlatitudes, which was likely due to the constant jet associated with the EIA. Additionally, the stronger signature of the diurnal variability in the GOCE data shows up as a wider spread in the distribution.

Even though GITM's distributions were narrower in the midlatitudes, its values of mean V_x were closer to those of GOCE than in the auroral latitudes. GITM's peak probabilities skewed slightly rightward (larger V_x) in comparison to GOCE in the midlatitudes, where it showed a tendency to overestimate wind speed by 10%-15%, but skewed leftward (too weak of V_x) of GOCE in the auroral latitudes, where it underestimated wind speeds, except during high geomagnetic activity. At moderate activity at auroral latitudes, GITM and GOCE's mean winds were quite similar, but

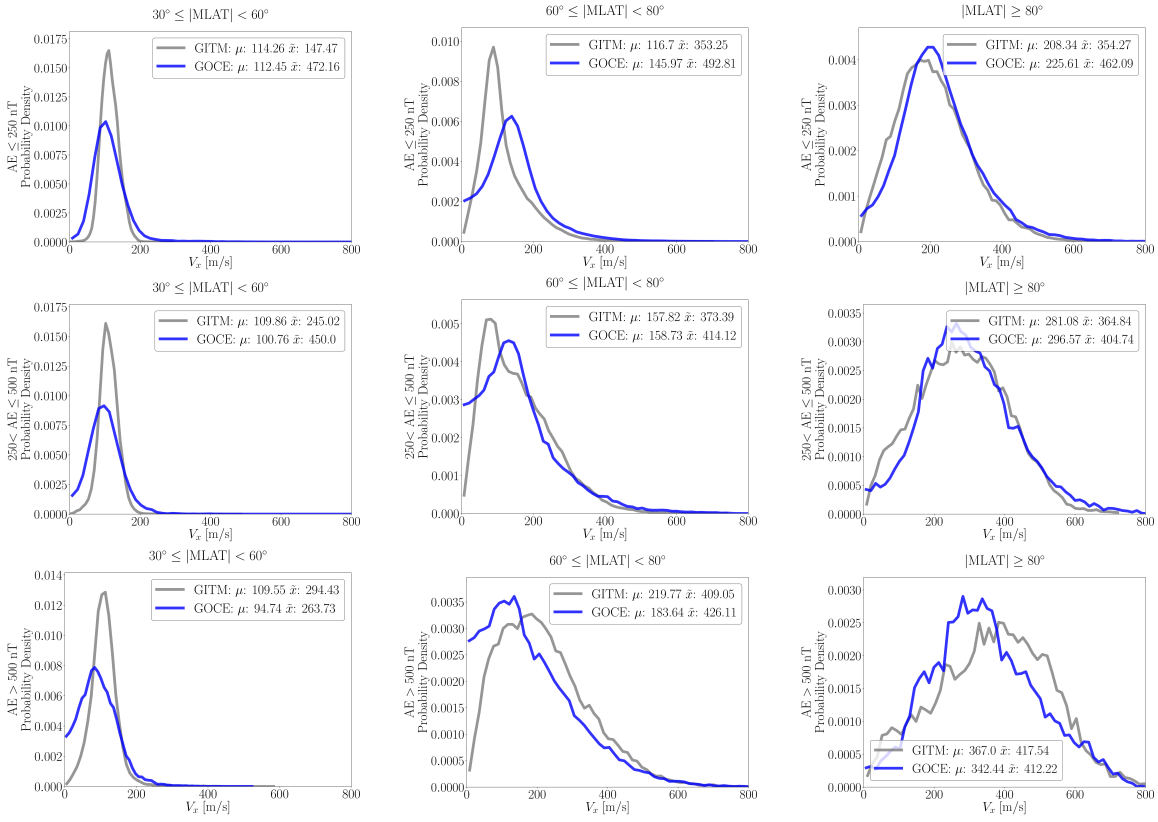

Figure 4.10: GITM and GOCE V_x probability densities across the three MLAT ranges for three different levels of geomagnetic activity.

GITM overestimated the winds in the auroral zone with high activity. GITM's probabilities matched GOCE's quite well in the polar region, with the exception of during high activity, where it tended to overestimate the wind speed. The overestimation of the wind speeds could be due to too much ion drag during stronger driving conditions, either due to over-prediction of ion drift speeds in the *Weimer* 2005 model, lack of ion drift variability, which may decrease the net force on the neutrals. This winds speeds that are too high may contribute to an insufficient heating rate during strong heating, due to the difference between the ion drift and neutral winds being too low (assuming that winds speeds that are too high implies smaller difference in the ion and neutral speeds).

The 10-month window chosen for this study allowed for the exploration of how

different conditions affected the GITM results. In the manner of *Visser et al.* 2019c, 25th, 50th, and 75th percentiles of the V_x were calculated for both GITM and GOCE V_x and were distributed as a function of AE, MLT, DOY, and F10.7 in each MLAT region (midlatitudes, auroral zone, and polar zone). Due to the fact that GITM was sampled at the GOCE locations and times, the number of counts of V_x per bin of the selected parameter were identical for both sets of data. The Northern and Southern Hemisphere data were combined for this analysis, except when binning the data as a function of MLT. In each figure, GITM results are shown with a red dashed line, and GOCE data shown with a solid blue line.

Figure 4.11 displays the dependence of V_x on AE for GITM in comparison to GOCE. The GOCE data show that in the low- and midlatitudes, thermospheric horizontal wind speeds decreased slightly as activity level increased. In both these regions, GITM significantly overestimated the wind speed. For the low-latitudes, the magnitude of the overestimation grew as a function of activity level, as GITM's winds did not decrease with activity. In this region, the overestimation grew from ∼10 m/s to ∼25 m/s between AE values of 50 to 1200. In contrast to the midlatitudes, where GITM's V_x values slightly decreased with activity, in the low latitudes, GITM's V_x slightly increased with activity. In the polar zone, GITM performed much better in capturing the characteristic increase in V_x with activity level shown in the GOCE data, even though it began to overestimate the wind speed above AE=400, growing to a difference of at least ∼100 m/s at AE=1200 nT. In the auroral zone, GOCE showed less dependence on activity level, with average wind speeds increasing only slightly with activity, while the GITM wind speeds increased significantly with AE. In this region, GITM underestimated the wind speeds for AE< 400 nT but increasingly overestimated them above that threshold. It is unclear why GOCE's horizontal wind speeds did not increase more significantly with activity in this region, which may be expected (*Killeen et al.* 1995).

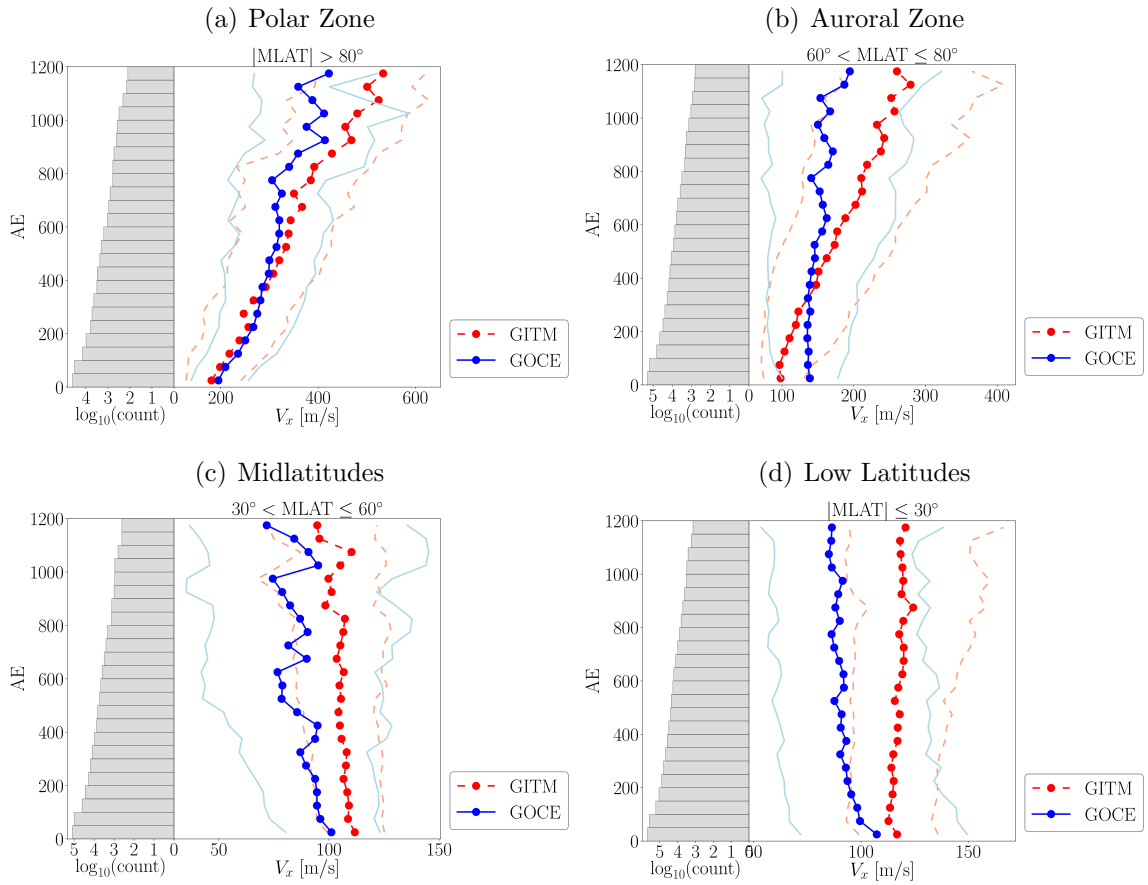

Figure 4.11: GITM and GOCE V_x binned by AE for different MLAT regions.

Next, variations with magnetic local time were considered (Figure 4.12). Most of the GOCE data are observed to be at ∼7 and ∼19 MLTs in the both the northern and southern auroral zones, due to GOCE being in a roughly dusk-to-dawn orbit (in geographic coordinates). Due to the offset between the geographic and magnetic poles, GOCE was able to sample all MLTs in the polar cap and most MLTs in the southern auroral zone, but was limited to coverage of near dawn and dusk at lower latitudes. In contrast to when V_x was distributed as function of AE, GITM generally underestimated V_x compared to GOCE.

GITM best matched GOCE in the low and midlatitudes, for which GITM mean V_x was generally consistent with GOCE but with significant variability: at the locations with the most data, GITM's wind speed was too large. Overall, GITM's wind speed

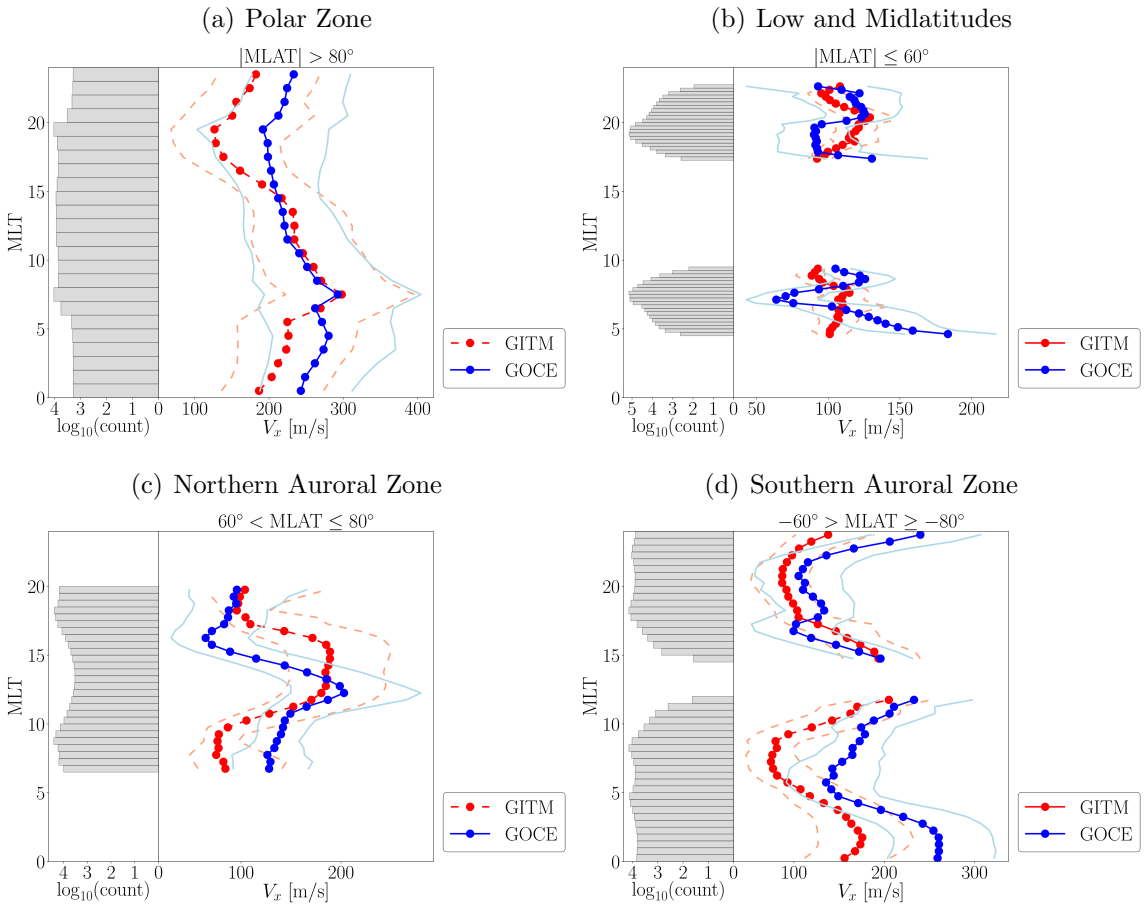

Figure 4.12: GITM and GOCE V_x binned by MLT for different MLAT regions.

at low- and mid-latitudes was too constant, which is similar to what was observed in Figure 4.11. The mismatch between GITM and GOCE was strongest in both auroral zones, with GITM mean V_x exceeding GOCE only for 13≤MLT≤17. In the auroral zones, the greatest underestimation by GITM occurred at MLT≈0 and MLT≈7 in the southern hemisphere, where GITM's mean V_x undershot GOCE V_x by nearly 100 m/s, approximately the same magnitude by which GITM overestimated the mean V_x in the northern hemisphere at MLT≈15. In the polar zone, GITM performed best for 7≤MLT≤15, where it's 25th, 50th (mean), and 75th percentiles of V_x tracked GOCE with minimal deviation. Outside of that MLT range, GITM generally underestimated V_x by ∼50 m/s. Overall, GITM demonstrated the best performance on the dayside, and the worst performance on the nightside around midnight. It may be that the solar-

driven ionization, and therefore the ion drag, may be best modeled at high latitudes on the dayside, while on the night side, the ionization is much more variable, and GITM may struggle with getting this correct.

Comparisons of seasonal effects of V_x for each hemisphere can be found in Figure (4.13). Due to the reentry of GOCE in November 2013, the analysis was limited and could not be extended through December 2013. Patterns in the GOCE data differed depending on the MLAT ranges considered.

In the northern polar zone, GOCE showed no discernible seasonal dependence, with its values of mean V_x oscillating around ∼250 m/s throughout the entire time considered. GITM's values of mean V_x tracked those of GOCE very well in this region, with GITM slightly overestimating the wind speed in the days surrounding the summer solstice. GITM's 25th and 75th percentile V_x values also did not deviate much at all from those of GOCE. Contrary to the northern case, in the southern polar zone, GITM underestimated V_x in all percentiles outside of mid-winter, even though it was able to capture the overall trend in the wind speeds throughout the year. Similar to how GITM overestimated the wind most in the northern polar zone during the summer solstice, it is around that time (i.e., the southern winter solstice) that GITM underestimated the wind in the southern polar zone most significantly. In both the northern and southern hemispheres, however, GITM's performance was best for $0 \leq \text{DOY} \leq 100$. It should be added that GOCE showed that in the southern polar hemisphere, the speed seemed to be seasonally dependent, with the strongest winds in the summer. GITM over-predicted the seasonal dependence, resulting in wind speeds that were too low during the winter.

In the northern auroral zone, the GOCE data showed no discernible dependency on season, with as its mean V_x clustered around ∼120 m/s throughout the year. GITM reproduced this behavior overall, with the slight caveat of underestimating the winds by up to ∼ 30 m/s between January and late February (northern winter). GITM's

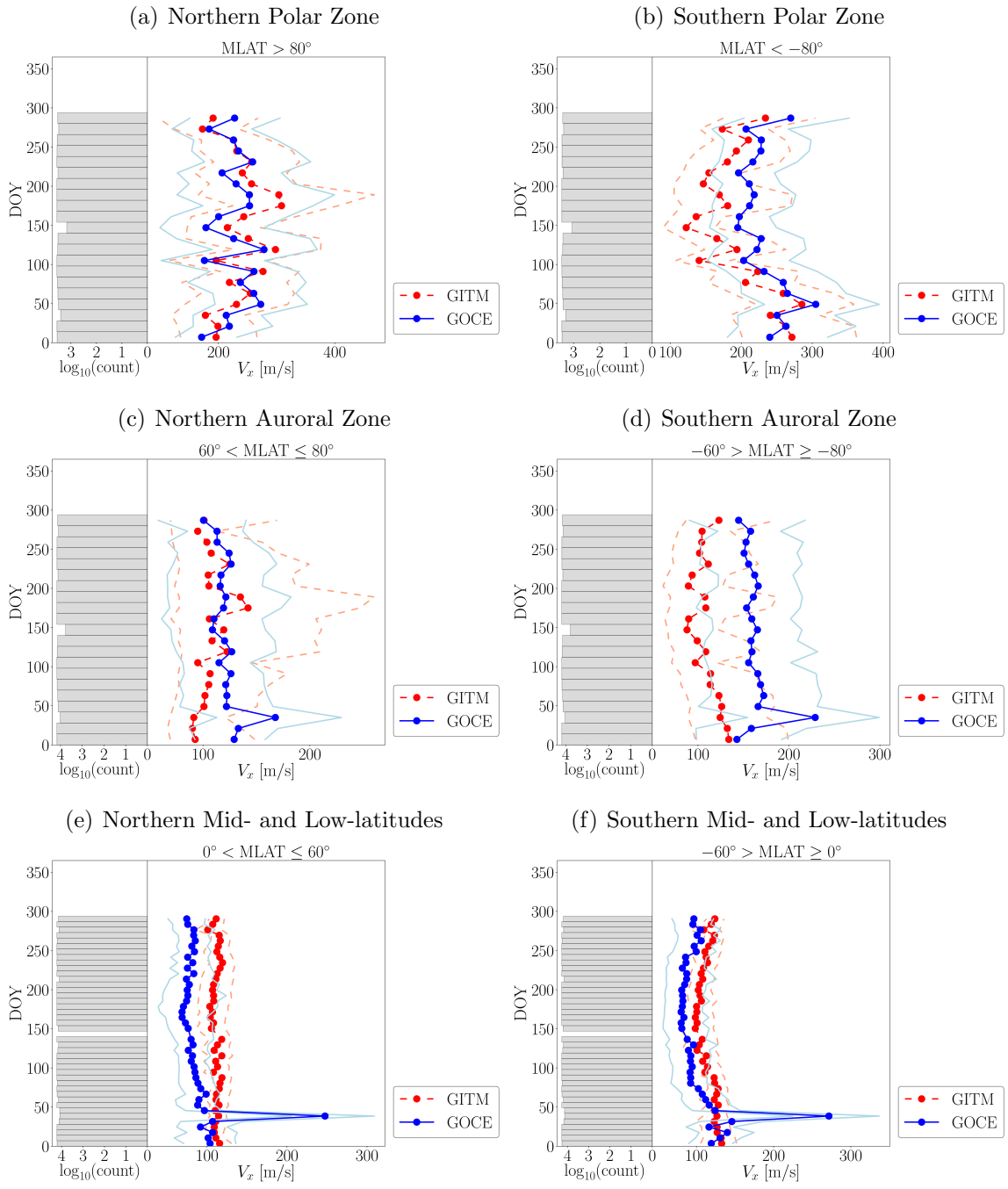

Figure 4.13: GITM and GOCE V_x binned by DOY for different MLAT regions.

25th percentile V_x values were similarly close to those of GOCE, but GITM's 75th percentile V_x values were much higher than GOCE's between the March Equinox and just prior to the autumnal equinox, indicating that GITM's horizontal winds were too variable during the summer. In the southern auroral zone, the GOCE wind speeds

were nearly identical to that of the northern auroral zone, except that the values of V_x were higher by tens of m/s. Here, GITM underestimated V_x in all percentiles throughout the entire time shown, and did not capture the contour of the GOCE data, instead showing a slight decline in winds speed that reached nadir at ∼100 m/s during the southern winter solstice before increasing again. GITM's underestimation can be highlighted by noting that its 75th percentile V_x values tracked the best with GOCE's mean V_x values throughout the entire year, and that its mean V_x values tracked best with GOCE's 25th percentile V_x values.

In the mid- and low-latitudes, for both hemispheres, the GOCE data showed a slight slowing of the wind across all percentiles that reached its nadir around June, before increasing slightly again through the end of October. GOCE's mean V_x values clustered around 100 m/s in January for both hemispheres and decreased to ∼80 m/s by the northern summer solstice, but the following increase in wind speed leading up to the autumnal equinox was slightly more prominent in the southern hemisphere by several m/s. In both hemispheres, GITM was closest to GOCE during early January. During the rest of the year, in both hemispheres, it overestimated V_x in all percentiles compared to GOCE, and its performance was worse in the northern hemisphere than the southern hemisphere. In the northern hemisphere, GITM did not capture the mild seasonal trend in V_x featuring the trough during the summer solstice, and its mean V_x values remained close to ∼100 m/s during the entire year. GITM performed better in the southern hemisphere, capturing the seasonality in V_x throughout the entire time shown, with its mean V_x values differing from those of GOCE by $\sim 10-15$ m/s outside of January and February. It is possible that this consistent overestimation of wind speeds in the mid and low latitudes is owed to the EIA-related jet that drove up average wind speed throughout the entire region.

Lastly, the horizontal wind response to F10.7 flux was analyzed, beginning with an overall view for GITM and GOCE across all MLAT (Figure 4.13(a)).

For the available range of F10.7 between ∼87 sfu and ∼175, the GOCE wind speed decreased in mean V_x down from ∼110 m/s around 90 sfu to ∼100 m/s around 130 sfu, before increasing to ∼130 m/s at 175 sfu. The GITM results do not capture this trend, with the mean V_x remaining around ∼120 m/s throughout the entire F10.7 range. Both GITM's 25th and 75th percentile V_x values were constrained between GOCE's 25th and 75th percentile values throughout the entire F10.7 range, indicating that GITM displays less wind variability than it should compared to the measurements.

Comparisons between GITM and GOCE for the ascending and descending nodes separately show differences in more detail, and allow for comparisons for the dusk and dawn sectors, respectively, given GOCE's orbit. For dusk, the ascending node (Figure 4.13(b)), GITM's mean V_x was consistently higher than GOCE's mean V_x throughout the entire range of F10.7, except at the highest levels. GITM also modeled faster V_x values too often, as shown by its 25th percentile values being greater than those of GITM by $\sim$ 30 m/s. This behavior was not seen, however, for the 75th percentiles, for which GITM matched GOCE very well.

GITM matched GOCE much better for the descending (dawn) node (Figure 4.13(c)), following its behavior of decreasing from 90<F10.7≤135, and rising from 135<F10.7≤175. GITM's mean V_x matched GOCE very well throughout the entire range of F10.7, while it's 25th percentile values were slightly higher than those of GOCE, and its 75th percentile values were slightly lower than those of GOCE.

Overall, distributed by F10.7, GITM performed better on the dawn sector in comparison to the dusk sector, where it overestimated wind speed. For both the ascending and descending nodes, GITM's variability of V_x was too constrained in comparison to GOCE.

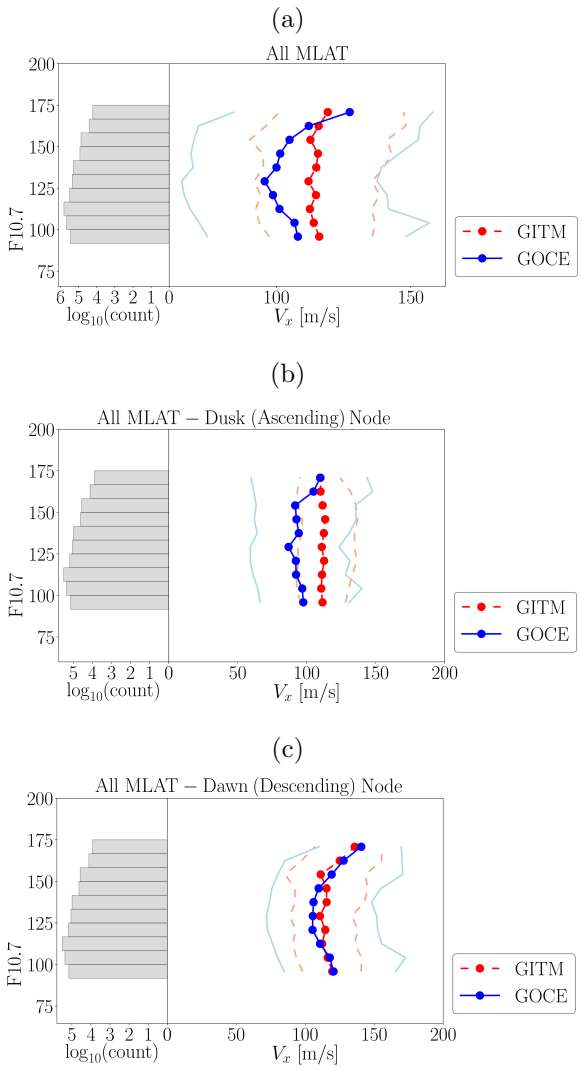

Figure 4.14: GITM and GOCE percentiles per bin of F10.7 flux for (a) the entire MLAT range, (b) for the ascending/dusk node, (c) and for the descending/dawn (node).

4.5.3 Vertical Winds

Vertical winds are additionally of interest as a subject of study, as upward motion in the thermosphere is typically accompanied by horizontal divergence of air higher in the thermosphere, and horizontal convergence of air lower in the thermosphere, with the vertical velocity being inversely proportional to the density and directly proportional to the pressure gradient (*Rishbeth and Müller-Wodarg* 1999). It is conventional

to assume a hydrostatic atmosphere, which results in the vertical wind emerging as a consequence of redistributed pressure levels, where it acts as a crucial component of adiabatic cooling (*Hsu et al.* 2014). GITM simulations have shown that vertical pressure gradient force can locally exceed the gravity force by 25% during strong driving, creating non-hydrostatic conditions, generating a disturbance transported from lower altitudes to higher altitudes through an acoustic wave, which can drive vertical wind perturbations to 150 m/s at 300 km, and raise the neutral density at high altitudes by more than 100% (*Deng and Ridley* 2006c). GITM simulations have also indicated that heating above 150 km is a primary source for a large increase of the average vertical velocity (40 m/s) at higher altitudes (*Deng et al.* 2011). Vertical winds exhibit increased variability and higher peak velocities with increasing magnetic latitude (*Spencer et al.* 1982b). In the northern polar cap, the vertical wind velocities can routinely reach maximums of approximately 50 m/s (*Ishii et al.* 2004), while downward velocities in excess of 100 m/s have been measured at Southern high-latitudes (*Anderson et al.* 2011). It remains, however, unclear, what mechanisms are primarily responsible for driving the different levels of the vertical wind at various latitudes and altitudes.

Figure 4.15 shows a comparison between GITM and GOCE vertical winds for 10 months. The behavior between the two show strong disagreement, and the following should be addressed:

1. GITM shows far too little temporal and latitudinal variation in the vertical wind speeds throughout the entire the considered.

2. The GOCE data show prominence of upward vertical motion in the northern hemisphere and downward vertical motion in the southern hemisphere. Not only does GITM not show this behavior whatsoever, but it shows a nodal dependency: GITM winds are primarily downward for the ascending node and primarily upward for the descending node.

3. The GOCE data show significant variability in the northern hemisphere throughout the mid- and auroral latitudes, while the GITM results show no such variability. In GITM, and it is assumed in the thermosphere, the main source of energy input variability is in the auroral zone. If there is another source of energy input, such as waves from the lower atmosphere (*Holton* 1982) that are known to have thermal effects on planetary atmospheres (*Müller-Wodarg et al.* 2019), that can drive such strong variability in the vertical winds, it is not included in any model of the thermosphere.

It seems that GITM is underestimating the vertical wind magnitude, and does not capture the variability at high latitudes due to auroral forcing. At the same time, it is additionally unclear whether or not the GOCE vertical winds are an accurate representation of the vertical winds. More measurements of the vertical winds at all latitudes and seasons are needed to address these discrepancies. Furthermore, comparisons to whole atmosphere models such as WACCM-X (*Liu et al.* 2010 and *Liu et al.* 2018) or GAIA (*Jin et al.* 2011) may demonstrate whether there exists significant wave driving from the lower atmosphere that could drive variability of vertical winds to ± 15 m/s at middle and low latitudes.

(a) Dusk

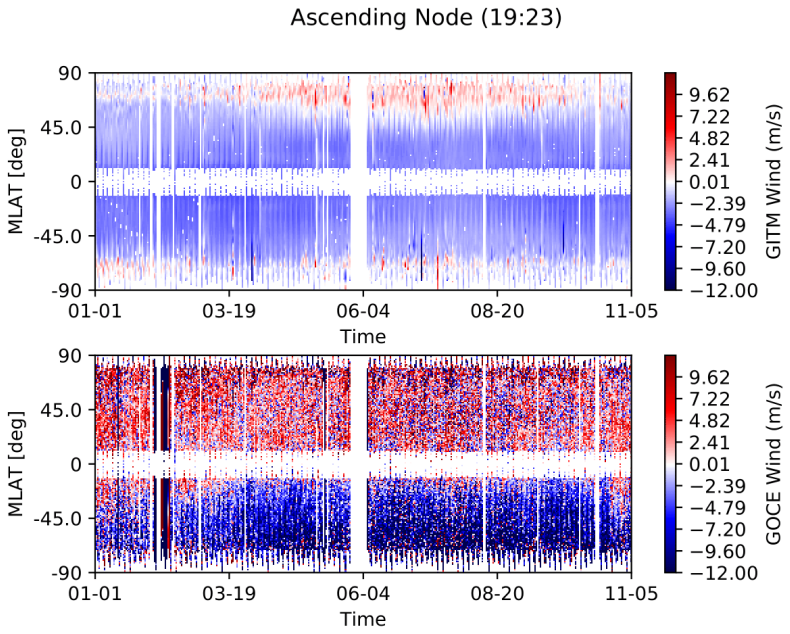

(b) Dawn

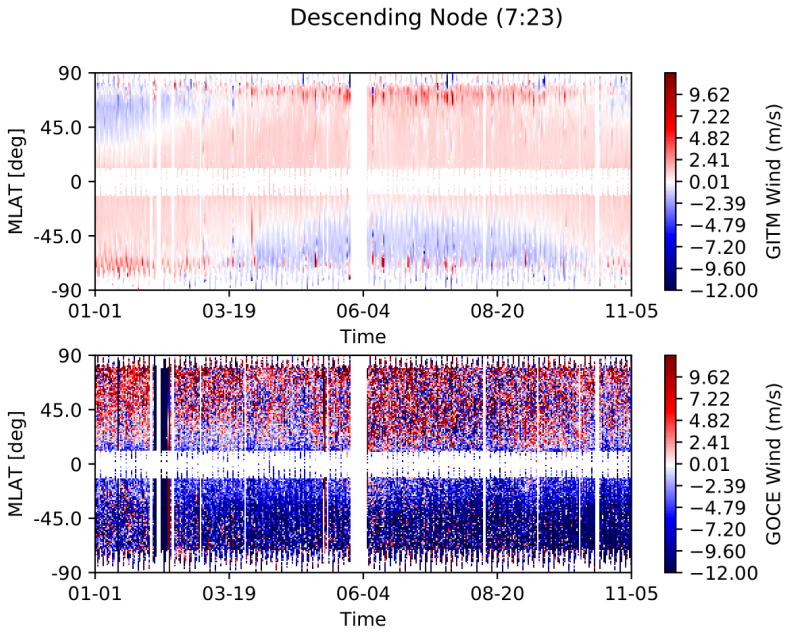

Figure 4.15: GITM and GOCE vertical wind for the ascending/dusk node (top) and descending/dawn node (bottom) for the available data of 2013.

4.6 Conclusion

GITM's capacity to model V_x has been analyzed using the methods of *Visser et al. 2019c*, with GOCE accelerometer-derived cross-track winds serving as the reference. The results showed that GITM possessed satisfactory capability to model cross-track (horizontal) winds, but also showed important areas for improvement. The most pertinent results are as follows:

1. Probability distributions for GITM and GOCE V_x show that GITM's performance improved as a function of MLAT, being best in the polar zone, and worst in the midlatitudes, where it had a persistent wind associated with the EIA. This may indicate ion drag that is too strong at low- and mid-latitudes.

2. As a function of geomagnetic activity represented by AE, GITM again performed the best in the polar and auroral zones, though it overestimated horizontal winds above AE$\sim$400. In all MLAT regions, GITM overestimated V_x as a function of AE. This may again indicate that the ion drag may be too strong in GITM. Further, by having neutral wind in the polar and auroral zones that are too strong, the frictional heating in GITM may be underestimated due to the heating being dependent on the velocity difference squared between the ions and neutrals, with the ion drifts being larger than the neutrals almost all of the time at high latitudes.

3. As a function of MLT, GITM performed the best in the polar zone near noon and worst in the auroral zones near midnight. When GITM was inaccurate compared to GOCE as a function of MLT, its tendency was to underestimate V_x more often than overestimate, which occurred prominently on the nightside.

4. As a function of DOY (season), GITM performed best in the northern polar and auroral zones, and worst in the southern auroral and polar zones. Season-

ality in the mid- and low-latitudes was best captured by GITM in the southern hemisphere. GITM primarily underestimated horizontal winds in the winter and overestimated them in the summer, although the amount of over and underestimation varied.

5. As a function of F10.7, at dusk, GITM displayed less variability than GOCE, and overall slightly overestimated horizontal winds, except for F10.7>150 sfu, where it tracked GOCE the best. At dawn, GITM tracked the dependence of the wind speeds on F10.7 quite well, though with less variability.

6. GITM's underestimation of winds in the summer could be an indication that ion drag could be inaccurate, which may be driven by either electron densities that are inaccurate or ion drifts that are inaccurate. This was true especially in the midlatitudes, where there was a persistent large wind speed modeled by GITM that was at a lower amplitude in GOCE.

This study indicates that GITM's modeling of the cross-track (horizontal) wind is broadly best at higher magnetic latitudes and generally marked by underestimation and insufficient variability of V_x. This may suggest that GITM places preferential emphasis on high-latitude drivers and needs further improvements in its handling of quiet-time conditions, as well as modeling of the seasonality of the diurnal tide, which displays amplitudes 2-3 times larger at equinoxes compared to solstices (*Lu et al.* 2011). Addressing these concerns may improve GITM's ability to capture seasonality, especially at the mid- and low-latitudes. Additional work includes investigating how improved modeling of viscosity and temperature can aid in GITM's modeling of thermospheric winds, as well as a follow-up study covering a wider period of time and incorporating both data from satellites and ground-based FPIs.

CHAPTER V

Conclusion

Satellite data represents a powerful tool for improving atmospheric modeling of thermospheric densities and winds. This is especially the case during geomagnetic storms, when thermal expansion of the atmosphere increases the local scale height and causes a local rise in density, as well as intensifying winds. This thesis presents a method for improving estimates of the thermospheric density during geomagnetic storms solely, by using publically available satellite orbit data, and additionally details an analysis of the storm-time performance of three empirical atmospheric models, and lastly, presents a statistical analysis of the wind modeling capabilities of the GITM physics=based model.

The Multifaceted Optimization Algorithm (MOA) was developed (Chapter II) to investigate using TLE-driven orbit-propagation to improve the storm-time performance of the MSIS-00 model. It uses SpOCK as the propagator, and relies on three subprocesses that estimate adjustments to the atmospheric driver inputs to the model:

1. AROPT: Minimizes orbit error between SpOCK and satellite TLEs by adjusting the cross-sectional area of the simulated satellite.

2. FOPT: Minimizes orbit error between SpOCK and satellite TLEs by adjusting F10.7 inputs to MSIS-00.

3. APOPT: Minimizes orbit error between SpOCK and satellite TLEs by adjusting a_p inputs to MSIS-00.

After these subprocesses are run using TLEs for multiple satellites, the mean driver adjustments are supplied to MSIS-00 along the trajectory of a validation spacecraft in order to compare orbit-averaged calibrated densities to orbit-averaged accelerometer or GPS-derived densities.

Running MOA for 10 Flock 3P satellites during a geomagnetic storm that occurred between 23 May 2017 and 2 June 2017, and applying the MSIS-00 driver adjustments along the Swarm-A and Swarm-B trajectories showed the greatest improvements in integrated orbit-averaged densities during the peak of the storm, where values of ρ_T for MOA differed from those of Swarm by an average of $\sim 3.8\%$, compared to MSIS-00, which differed an average of $\sim 27.7\%$ from Swarm. While MOA did marginally overestimate the orbit-averaged density along Swarm-B, (70 km above Swarm-A) this overestimation was marginal, and superseded by MOA's capability at broadening the peak density response and additionally decreasing the density prior to the storm, matching Swarm overall to a noticeably higher degree than uncalibrated MSIS-00. MOA demonstrates that with TLEs from as few as 10 small satellites, improvements in empirical model density estimates can be achieved for better stormtime density nowcasting. Ultimately, MOA's capabilities should be extended by incorporating TLEs from a wider variety operational satellites, rocket bodies, and trackable space debris, its methods should be tested for storms of varying intensities, and its ability or not to calibrate other atmospheric models should be explored, and its development into a density prediction tool should be explored. In this way, MOA's status as a coarse thermospheric model calibration tool can be established for use by the broader space situational awareness and space traffic management community.

In order to further explore the limitations and biases of thermospheric density models, a superposed epoch analysis (SEA) was performed for the MSIS-00, JB-

2008, and DTM-2013 empirical models (Chapter III), for 42 CME-driven geomagnetic storms of varying intensity collected between 2001-05-01 and 2010-08-31, and compared to accelerometer-derived densities from the CHAMP satellite. Densities from each storm were expressed in terms of percent change from their average quiet-time value, and compressed or stretched to conform to a normalized epoch timeline constructed from the average duration of each phase of all of the geomagnetic storms considered. Superposition of all of the storms atop the normalized epoch timeline visually revealed density responses that were too small by MSIS-00 and DTM-2013, and a density response that was too great by JB-2008. Linear relations constructed between peak storm density and peak storm Dst indicate that the strongest correlation between global geomagnetic disturbances and main phase responsiveness occurred for JB-2008, which tracks well with the fact that its underlying set of parametric coefficients includes a Dst dependency. Linear relations constructed between peak model densities and peak CHAMP densities demonstrated that the characteristic underestimation for DTM-2013 and MSIS-00 across all considered storms was on the order of $\sim 8\%$ and $\sim 45\%$, respectively, while the characteristic overestimation by JB-2008 was $\sim 0.2\%$. These results suggest that DTM-2013 is the most robust empirical density model across storms of any intensity, and further suggest the possibility of using a Dst-based calibration to improve performance for JB-2008, based on both its underlying parameterization and the correlation between its density response to peak Dst. This simple superposed epoch analysis has demonstrated a means of quantifying density model performance and additionally shed light on possible methods of index-based calibration that may vary based on storm intensity, altitude, and season.

Lastly, the capability of the GITM model to capture horizontal wind speed (V_x) behavior observed by the GOCE satellite is investigated (Chapter IV). GITM was run from January to November 2013, and data was extracted along the GOCE spacecraft orbit, which orbited Earth in a sun-synchronous orbit at ~ 270 km. GITM demon-

strated difficulty in capturing fine latitudinal structures in the horizontal wind and placed a morphological feature corresponding to crests of increased wind speed at $\pm 20^{\circ} - 30^{\circ}$, coincident with the Equatorial Ionization Anomaly. Probability densities of GITM V_x and GOCE V_x as a function of MLAT and AE indicated that GITM under-models horizontal wind variability in the midlatitudes, and performs best at auroral and polar latitudes, particularly at moderate geomagnetic activity. Distributing GITM and GOCE V_x across bins of AE, MLAT, MLT, DOY and F10.7 yielded the following results:

1. As a function of AE, GITM performs best in the polar and auroral zones, with an overall tendency to overestimate the wind speeds at stronger driving.

2. As a function of MLT, GITM performs best at polar noon and worst at auroral midnight.

3. As a function of DOY, GITM is best in the northern polar and auroral zones, and worst in the southern and auroral polar zones, and captures seasonality best in the southern hemisphere.

4. As a function of F10.7, GITM V_x tracks GOCE best during dawn, though it is less variable and overestimates during dusk.

GITM's difficulty modeling V_x seasonality and variability, as well as its higher midlatitude wind speeds in the EIA region may be related to inaccurate modeling of electron densities and/or ion drifts. GITM's modeling of viscosity and Eddy diffusion also constitute non-trivial points of consideration, given their importance in vertical flows and thermal conduction that are related to horizontal convergence and divergence processes in the general circulation of the thermosphere. Overall, this statistical study reveals avenues for model improvement realized by considering the relationship between various thermospheric drivers on wind data, with GOCE as the standard.

Future work ought to involve a similar analysis being conducted on ground-based FPI data, and including satellite-derived winds at higher LEO altitudes and with varying orbital inclinations, in order to determine if there is an altitudinal dependency to GITM's performance. Additionally, future work should extend the time period for which GITM is run and compared to reference data by several years, in order to determine how GITM performs throughout the solar cycle.

Ultimately, this body of research comprises an interconnected web of satellite-driven model development, with a particular focus towards simple methods of atmospheric model calibration. This thesis demonstrates that (1) model improvements are attainable with simple calibration methods, (2) that empirical density models can be explored and have their biases characterized clearly with well-established analytical methods, and that avenues for possible methods of calibration can be revealed by these methods, and (3) that comprehensive statistical analysis of physical model results can reveal gaps in the understanding of the thermosphere as a physical system.

Further studies will investigate how MOA performs when many more satellites are used for calibration, and how its performance over storms of different intensities may or may not vary. Additional studies will investigate MOA's capacity for density prediction, with either usage of solar and geomagnetic index predictions from NASA's Space Weather Prediction Center, or using machine learning techniques. Ensemble techniques should also be investigated, involving using the results of SEA for each empirical density model to account for each of their deficiencies and improve density predictions during geomagnetic storms.

Additional work incorporating SEA should involve the investigation of e-folding recovery time across all models as a function of phase and storm intensity, studying the feasibility of an ensemble method involving averaging the densities from all of the models together, and an investigation into calibration methods specific to each model using different solar and geomagnetic indices. Model biases should be analyzed as a

function of not only storm intensity, but also under different solar conditions, such as characterizing model biases for severe storms both when F10.7 $<$ 120 sfu and when F10.7 $>=$ 120. Given that SEA is can being performed for densities expressed in terms of percent change from the pre-storm quiet-time average, this allows for superposing storm-time model densities estimated along the orbits of multiple satellites, which highlights the importance future work involving conducting SEA over many years of storms, along the orbits of CHAMP, GOCE, GRACE, and Swarm. This work would not only make clearer any index- and intensity-related biases in each model due to increasing the amount of data used, but would also would allow for investigation into altitude-related biases, as each of the aforementioned satellites currently orbits or previously orbited at different altitudes.

Future work involving the study of thermospheric winds should involve extending the probability and histogram analysis to more years of data, especially in order to study seasonal effects in more detail. Future analyses should also incorporate ground-based data, which can serve not only to extend the years over which investigation may be performed, but also show if there any non-trivial discrepancies between wind observations obtained via different methods.

Overall, these endeavors demonstrate the scientific and engineering applications of the satellite-model duality, and progress in each shows their power as tools in development for the space community, to the benefit of satellite operators, the safety of astronauts, better understanding of atmospheric physics, and improved capabilities of space situational awareness.

BIBLIOGRAPHY

BIBLIOGRAPHY

(1981), Dynamics explorer spacecraft and ground operations systems, *Space Sci. Instrum.*, *5*(4), 349–367.

Akasofu, S.-I. (2018), A review of the current understanding in the study of geomagnetic storms, doi:10.35840/2631-5033/1818.

Akins, K., L. Healy, S. Coffey, and M. Picone (2003), Comparison of msis and jacchia atmospheric density models for orbit determination and propagation, *13th AAS/AIAA Space Flight Mechanics Meeting*, (AAS 03-165).

Anderson, C., M. Conde, and M. G. McHarg (2012), Neutral thermospheric dynamics observed with two scanning doppler imagers: 2. vertical winds, *Journal of Geophysical Research*, *117*(A03305), doi:https://doi.org/10.1029/2011JA017157.

Anderson, C. T., M. Davies, M. Conde, P. Dyson, and M. J. Kosch (2011), Spatial sampling of the thermospheric vertical wind field at auroral latitudes, *J. Geophys. Res.*, *116*(A06320).

Aruliah, A. L., and D. Rees (1995), The trouble with thermospheric vertical winds: geomagnetic, seasonal and solar cycle dependence at high latitudes, *Journal of Atmospheric and Terrestrial Physics*, *57*, 597–609.

Bag, T., M. Sunil Krishna, S. Gahlot, and V. Singh (2014), Effect of severe geomagnetic storm conditions on atomic oxygen greenline dayglow emission in mesosphere, *Advances in Space Research*, *53*(8), 1255–1264, doi:https://doi.org/10.1016/j.asr.2014.01.031.

Balan, N., L. Liu, and H. Le (2018), A brief review of equatorial ionization anomaly and ionospheric irregularities, *Earth and Planetary Physics*, *2*(4), 257–275, doi:https://doi.org/10.26464/epp2018025.

Baliukin, I. I., J.-L. Bertaux, E. Quémerais, V. V. Izmodenov, and W. Schmidt (2019), Swan/soho lyman-α mapping: The hydrogen geocorona extends well beyond the moon, *Journal of Geophysical Research: Space Physics*, *124*(2), 861–885, doi:https://doi.org/10.1029/2018JA026136.

Barlier, F., C. Berger, J. L. Falin, G. Kockarts, and G. Thuillier (1978), A thermospheric model based on satellite drag data, *Annales Geophysicae*, *34*, 9–24.

Bartels, J. (1949), The standardized index ks, and the planetary index kp, *IATME Bulletin*, *12b*(97).

Bartels, J., and J. Veldkamp (1954), International data on magnetic disturbances, fourth quarter, 1953, *Journal of Geophysical Research*, *59*, 297–302.

Bartels, J., N. H. Heck, and H. F. Johnston (1939), The three-hour range index measuring geomagnetic activity, *Journal of Geophysical Research*, *44*(4), 411–454, doi:10.1029/TE044i004p00411.

Bastida Virgili, B., et al. (2016), Risk to space sustainability from large constellations of satellites, *Acta Astronautica*, *126*, 154–162, doi:https://doi.org/10.1016/j.actaastro.2016.03.034, space Flight Safety.

Beaussier, J., A.-M. Mainguy, A. Olivero, and R. Rolland (1977), In orbit performance of the cactus accelerometer (d5b spacecraft), *Acta Astronautica*, *4*(9), 1085–1102, doi:https://doi.org/10.1016/0094-5765(77)90008-X.

Bellan, P. M. (2006), Cambridge University Press, Cambridge, UK.

Berger, C., R. Biancale, M. Ill, and F. Barlier (1998), Improvement of the empirical thermospheric model dtm: Dtm94 – a comparative review of various temporal variations and prospects in space geodesy applications, *Journal of Geodesy*, *72*(3), 161–178, doi:10.1007/s001900050158.

Bernstein, V., M. Pilinski, and D. Knipp (2020), Evidence for drag coefficient modeling errors near and above the oxygen-to-helium transition, *Journal of Spacecraft and Rockets*, *57*(6), 1246–1263, doi:10.2514/1.A34740.

Bhatnagar, V. P., G. A. Germany, and A. Tan (2005), Satellite ballistic coefficients and the lower thermosphere, *Geophysical Research Letters*, *32*(3), doi:https://doi.org/10.1029/2004GL021627.

Bilitza, D. (2001), International reference ionosphere 2000, *Radio Science*, *36*(2), 261–275, doi:https://doi.org/10.1029/2000RS002432.

Billett, D. D., K. A. McWilliams, and M. G. Conde (2020), Colocated observations of the e and f region thermosphere during a substorm, *Journal of Geophysical Research: Space Physics*, *125*(11), e2020JA028,165, doi:https://doi.org/10.1029/2020JA028165, e2020JA028165 10.1029/2020JA028165.

Biondi, M. A. (1984a), Measured vertical motion and converging and diverging horizontal flow of the midlatitude thermosphere, *Geophysical Research Letters*, *11*(1), 84–87, doi:https://doi.org/10.1029/GL011i001p00084.

Biondi, M. A. (1984b), Measured vertical motion and converging and diverging horizontal flow of the midlatitude thermosphere, *Geophysical Research Letters*, *11*, 84–87.

Biondi, M. A., and D. P. Sipler (1985), Horizontal and vertical winds and temperatures in the equatorial thermosphere: Measurements from natal, brazil during august–september 1982, *Planetary and Space Science*, *33*(7), 817–823, doi: https://doi.org/10.1016/0032-0633(85)90035-2.

Blanch, E., and D. Altadill (2012), Midlatitude f region peak height changes in response to interplanetary magnetic field conditions and modeling results, *Journal of Geophysical Research: Space Physics*, *117*(A12), doi:https://doi.org/10.1029/2012JA018009.

Blum, P., I. Harris, and W. Priester (1972), in *COSPAR International Reference Atmosphere*, p. 399, Akademie-Verlag, Berlin.

Borovsky, J. E., and M. H. Denton (2006), Differences between cme-driven storms and cir-driven storms, *Journal of Geophysical Research: Space Physics*, *111*(A7), doi:https://doi.org/10.1029/2005JA011447.

Bowman, B., W. Tobiska, and F. Marcos (), *A New Empirical Thermospheric Density Model JB2006 Using New Solar Indices*, doi:10.2514/6.2006-6166.

Bowman, B. R., W. K. Tobiska, F. A. Marcos, C. Y. Huang, C. S. Lin, and W. J. Burke (2008), A new empirical thermospheric density model jb2008 using new solar and geomagnetic indices, *AIAA/AAS Astrodynamics Specialist Conference*, (AIAA 2008-6438).

Bowman, M. R., A. J. GIbson, and M. C. W. Sandford (1969), Atmospheric sodium measured by a tuned laser radar, *Nature*, *221*(5179), 456–457, doi: 10.1038/221456a0.

Brandt, D. A., C. D. Bussy-Virat, and A. J. Ridley (2020), A simple method for correcting empirical model densities during geomagnetic storms using satellite orbit data, *Space Weather*, *18*(12), e2020SW002,565, doi:https://doi.org/10.1029/2020SW002565, e2020SW002565 10.1029/2020SW002565.

Brinton, H. C., L. R. Scott, M. W. Pharo III, and J. T. Coulson (1973), The bennett ion-mass spectrometer on atmosphere explorer-c and -e, *Radio Science*, *8*(4), 323–332, doi:https://doi.org/10.1029/RS008i004p00323.

Brouwer, D. (1959), Solution of the problem of artificial satellite theory without drag, *The Astronomical Journal*, *64*.

Bruinsma, S. (2013), The semi-empirical model dtm2012, *6th European Conference on Space Debris, Proceedings of the Conference held 22-25 April 2013, in Darmstadt, Germany, Edited by L. Ouwehand.*

Bruinsma, S. (2015), The dtm-2013 thermosphere model, *Journal of Space Weather and Space Climate*, *5*, 8, doi:10.1051/swsc/2015001.

Bruinsma, S., G. Thuillier, and F. Barlier (2003), The dtm-2000 empirical thermosphere model with new data assimilation and constraints at lower boundary: accuracy and properties, *Journal of Atmospheric and Solar-Terrestrial Physics*, *65*(9), 1053–1070, doi:https://doi.org/10.1016/S1364-6826(03)00137-8.

Bruinsma, S., D. Tamagnan, and R. Biancale (2004), Atmospheric densities derived from champ/star accelerometer observations, *Planetary and Space Science*, *52*(4), 297–312, doi:https://doi.org/10.1016/j.pss.2003.11.004.

Bruinsma, S., J. M. Forbes, R. S. Nerem, and X. Zhang (2006), Thermosphere density response to the 20–21 november 2003 solar and geomagnetic storm from champ and grace accelerometer data, *Journal of Geophysical Research: Space Physics*, *111*(A6), doi:https://doi.org/10.1029/2005JA011284.

Bruinsma, S. L., and J. M. Forbes (2007), Global observation of traveling atmospheric disturbances (tads) in the thermosphere, *Geophysical Research Letters*, *34*(14), doi:https://doi.org/10.1029/2007GL030243.

Bruinsma, S. L., and J. M. Forbes (2008), Medium- to large-scale density variability as observed by champ, *Space Weather*, *6*(8), doi:https://doi.org/10.1029/2008SW000411.

Bruinsma, S. L., and J. M. Forbes (2009), Properties of traveling atmospheric disturbances (tads) inferred from champ accelerometer observations, *Advances in Space Research*, *43*(3), 369–376, doi:https://doi.org/10.1016/j.asr.2008.10.031.

Bruinsma, S. L., N. Sánchez-Ortiz, E. Olmedo, and N. Guijarro (2012), Evaluation of the dtm-2009 thermosphere model for benchmarking purposes, *Journal of Space Weatehr and Space Climate*, *2*, doi:10.1051/swsc/2012005.

Budzien, S. A., R. L. Bishop, A. W. Stephan, A. B. Christensen, and D. R. McMullin (2010), Atmospheric remote sensing on the international space station, *Eos, Transactions American Geophysical Union*, *91*(42), 381–382, doi:https://doi.org/10.1029/2010EO420002.

Burnside, R. G., C. A. Tepley, M. P. Sulzer, T. J. Fuller-Rowell, D. G. Torr, and R. G. Roble (1991), The neutral thermosphere at arecibo during geomagnetic storms, *Journal of Geophysical Research: Space Physics*, *96*(A2), 1289–1301, doi:https://doi.org/10.1029/90JA01595.

Bussy-Virat, C., J. Getchius, and A. Ridley (2018a), *The Spacecraft Orbital Characterization Kit and its Applications to the CYGNSS Mission*, doi:10.2514/6.2018-1973.

Bussy-Virat, C. D. (2017), Spacecraft collision avoidance, Ph.D. thesis, University of Michigan.

Bussy-Virat, C. D., and A. J. Ridley (2021), Estimation of the thermospheric density using ephemerides of the cygnss and swarm constellations, *Journal of Atmospheric and Solar-Terrestrial Physics*, *221*, 105,687, doi:https://doi.org/10.1016/j.jastp.2021.105687.

Bussy-Virat, C. D., A. J. Ridley, and J. W. Getchius (2018b), Effects of uncertainties in the atmospheric density on the probability of collision between space objects, *Space Weather*, *16*(5), 519–537, doi:https://doi.org/10.1029/2017SW001705.

Bussy-Virat, C. D., A. J. Ridley, A. Masher, K. Nave, and M. Intelisano (2019), Assessment of the differential drag maneuver operations on the cygnss constellation, *IEEE Journal of Selected Topics in Applied Earth Observations and Remote Sensing*, *12*(1), 7–15, doi:10.1109/JSTARS.2018.2878158.

Byrne, J. P., S. A. Maloney, R. T. J. McAteer, J. M. Refojo, and P. T. Gallagher (2010), Propagation of an earth-directed coronal mass ejection in three dimensions, *Nature Communications*, *1*, doi:10.1038/ncomms1077.

Cai, L., S. Oyama, A. Aikio, H. Vanhamäki, and I. Virtanen (2019), Fabry-perot interferometer observations of thermospheric horizontal winds during magnetospheric substorms, *Journal of Geophysical Research: Space Physics*, *124*(5), 3709–3728, doi:https://doi.org/10.1029/2018JA026241.

Calabia, A., and S. Jin (2017), Thermospheric density estimation and responses to the march 2013 geomagnetic storm from grace gps-determined precise orbits, *Journal of Atmospheric and Solar-Terrestrial Physics*, *154*, 167–179, doi:https://doi.org/10.1016/j.jastp.2016.12.011.

Carovillano, R. L., and G. L. Siscoe (1973), Energy and momentum theorems in magnetospheric processes, *Reviews of Geophysics*, *11*(2), 289–353, doi:https://doi.org/10.1029/RG011i002p00289.

Casali, S. J., and W. N. Barker (2002), Dynamic calibration atmosphere (dca) for the high accuracy satellite drag model (hasdm), in *AIAA/AAS Astrodynamics Specialist Conference*, AIAA-2002-4008, Monterey, CA.

Ceplecha, Z., J. Borovička, W. G. Elford, D. O. ReVelle, R. L. Hawkes, V. Porubčan, and M. Šimek (1998), Meteor phenomena and bodies, *Space Science Reviews*, *84*(3), 327–471, doi:10.1023/A:1005069928850.

Chamberlin, P. C., T. N. Woods, and F. G. Eparvier (2007a), Flare irradiance spectral model (fism): Daily component algorithms and results, *Space Weather*, *5*(7), doi:https://doi.org/10.1029/2007SW000316.

Chamberlin, P. C., T. N. Woods, and F. G. Eparvier (2007b), Flare irradiance spectral model (fism): Daily component algorithms and results, *Space Weather*, *5*(7), doi:https://doi.org/10.1029/2007SW000316.

Chamberlin, P. C., T. N. Woods, and F. G. Eparvier (2008), Flare irradiance spectral model (fism): Flare component algorithms and results, *Space Weather*, *6*(5), doi: https://doi.org/10.1029/2007SW000372.

Chapman, S., and V. C. A. Ferraro (1930), A new theory of magnetic storms, *Nature*, *126*(3169), 129–130, doi:10.1038/126129a0.

Chau, J. L., and M. Clahsen (2019), Empirical phase calibration for multistatic specular meteor radars using a beamforming approach, *Radio Science*, *54*(1), 60–71, doi:https://doi.org/10.1029/2018RS006741.

Chau, J. L., J. M. Urco, J. Vierinen, B. J. Harding, M. Clahsen, N. Pfeffer, K. M. Kuyeng, M. A. Milla, and P. J. Erickson (2021), Multistatic specular meteor radar network in peru: System description and initial results, *Earth and Space Science*, *8*(1), e2020EA001,293, doi:https://doi.org/10.1029/2020EA001293, e2020EA001293 2020EA001293.

Chen, G.-m., J. Xu, W. Wang, J. Lei, and A. G. Burns (2012), A comparison of the effects of cir- and cme-induced geomagnetic activity on thermospheric densities and spacecraft orbits: Case studies, *Journal of Geophysical Research: Space Physics*, *117*(A8), doi:https://doi.org/10.1029/2012JA017782.

Chen, G.-m., J. Xu, W. Wang, and A. G. Burns (2014), A comparison of the effects of cir- and cme-induced geomagnetic activity on thermospheric densities and spacecraft orbits: Statistical studies, *Journal of Geophysical Research: Space Physics*, *119*(9), 7928–7939, doi:https://doi.org/10.1002/2014JA019831.

Cheng, X., J. Yang, C. Xiao, and X. Hu (2020), Density correction of nrlmsise-00 in the middle atmosphere (20–100 km) based on timed/saber density data, *Atmosphere*, *11*(4), doi:10.3390/atmos11040341.

Chern, J.-S., B. Wu, Y.-S. Chen, and A.-M. Wu (2012), Suborbital and low-thermospheric experiments using sounding rockets in taiwan, *Acta Astronautica*, *70*, 159–164, doi:https://doi.org/10.1016/j.actaastro.2011.07.030.

Chree, C. (1912), Some phenomena of sunspots and of terrestrial magnetism, at kew observatory, *Philosophical Transactions Royal Society London Series A*, *212*, 75.

Chree, C. (1913), Some phenomena of sunspots and of terrestrial magnetism, ii, *Philosophical Transactions Royal Society London Series A*, *213*, 245.

Chu, X., Z. Yu, C. S. Gardner, C. Chen, and W. Fong (2011), Lidar observations of neutral fe layers and fast gravity waves in the thermosphere (110–155 km) at mcmurdo (77.8°s, 166.7°e), antarctica, *Geophysical Research Letters*, *38*(23), doi: https://doi.org/10.1029/2011GL050016.

Cid, C., J. Palacios, E. Saiz, Y. Cerrato, J. Aguado, and A. Guerrero (2013a), Modeling the recovery phase of extreme geomagnetic storms, *Journal of Geophysical Research: Space Physics*, *118*(7), 4352–4359, doi:https://doi.org/10.1002/jgra.50409.

Cid, C., J. Palacios, E. Saiz, Y. Cerrato, J. Aguado, and A. Guerrero (2013b), Modeling the recovery phase of extreme geomagnetic storms, *Journal of Geophysical Research: Space Physics*, *118*(7), 4352–4359, doi:https://doi.org/10.1002/jgra.50409.

Clausen, L. B. N., S. E. Milan, and A. Grocott (2014), Thermospheric density perturbations in response to substorms, *Journal of Geophysical Research: Space Physics*, *119*(6), 4441–4455, doi:https://doi.org/10.1002/2014JA019837.

Coffey, H., and E. Erwin (2001), When do the geomagnetic aa and ap indices disagree?, *Journal of Atmospheric and Solar-Terrestrial Physics*, *63*(5), 551–556, doi:https://doi.org/10.1016/S1364-6826(00)00171-1, interplanetary medium and geophysical phenomena during geomagnetic stroms.

Cole, K. D. (1966), Magnetic storms and associated phenomena, *Space Science Reviews*, *5*(6), 699–770, doi:10.1007/BF00173103.

Conde, M., et al. (2001), Assimilated observations of thermospheric winds, the aurora, and ionospheric currents over alaska, *Journal of Geophysical Research: Space Physics*, *106*(A6), 10,493–10,508, doi:https://doi.org/10.1029/2000JA000135.

Craig, R. A. (1965), Chapter 6 composition and structure of the thermosphere, in *The Upper Atmosphere Meteorology and Physics*, *International Geophysics*, vol. 8, edited by R. A. Craig, pp. 234–278, Academic Press, doi:https://doi.org/10.1016/S0074-6142(08)60054-6.

Dai, Y., W. Pan, X. Hu, Z. Bai, C. Ban, H. Zhang, and Y. Che (2020), An approach for improving the nrlmsise-00 model using a radiosonde at golmud of the tibetan plateau, *Meteorology and Atmospheric Physics*, *132*(4), 451–459, doi:10.1007/s00703-019-00700-w.

Dalgarno, A., W. B. Hanson, N. W. Spencer, and E. R. Schmerling (1973), The atmosphere explorer mission, *Radio Science*, *8*(4), 263–266, doi:https://doi.org/10.1029/RS008i004p00263.

Danilov, A., and U. Kalgin (1992), Seasonal and latitudinal variations of eddy diffusion coefficient in the mesosphere and lower thermosphere, *Journal of Atmospheric and Terrestrial Physics*, *54*(11), 1481–1489, doi:https://doi.org/10.1016/0021-9169(92)90155-E.

Davis, T. N., and M. Sugiura (1966), Auroral electrojet activity index ae and its universal time variations, *Journal of Geophysical Research (1896-1977)*, *71*(3), 785–801, doi:https://doi.org/10.1029/JZ071i003p00785.

De Franceschi, G., T. L. Gulyaeva, and L. Perrone (2001), Forecasting geomagnetic activity three hours in advance for ionospheric applications, *Annals of Geophysics*, *44*(5-6), doi:10.4401/ag-3556.

de Wit, T. D., and S. Bruinsma (2017), The 30 cm radio flux as a solar proxy for thermosphere density modeling, *Journal of Space Weather and Space Climate*, *7*(A9), doi:10.1051/swsc/2017008.

de Wit, T. D., S. Bruinsma, and K. Shibasaki (2014), Synoptic radio observations as proxies for upper atmospheric modelling, *Journal of Space Weather and Space Climate*, *4*(A06), doi:10.1051/swsc/2014003.

Deng, Y., and A. J. Ridley (2006a), Dependence of neutral winds on convection e-field, solar euv, and auroral particle precipitation at high latitudes, *Journal of Geophysical Research: Space Physics*, *111*(A9), doi:https://doi.org/10.1029/2005JA011368.

Deng, Y., and A. J. Ridley (2006b), Role of vertical ion convection in the high-latitude ionospheric plasma distribution, *Journal of Geophysical Research: Space Physics*, *111*(A9), doi:https://doi.org/10.1029/2006JA011637.

Deng, Y., and A. J. Ridley (2006c), Dependence of neutral winds on convection e-field, solar euv, and auroral particle precipitation at high latitudes, *Journal of Geophysical Research*, *111*.

Deng, Y., and A. J. Ridley (2007), Possible reasons for underestimating joule heating in global models: E field variability, spatial resolution, and vertical velocity, *Journal of Geophysical Research: Space Physics*, *112*(A9), doi:https://doi.org/10.1029/2006JA012006.

Deng, Y., A. D. Richmond, A. J. Ridley, and H.-L. Liu (2008), Assessment of the non-hydrostatic effect on the upper atmosphere using a general circulation model (gcm), *Geophysical Research Letters*, *35*(1), doi:https://doi.org/10.1029/2007GL032182.

Deng, Y., T. J. Fuller-Rowell, R. A. Akmaev, and A. J. Ridley (2011), Impact of the altitudinal joule heating distribution on the thermosphere, *Journal of Geophysical Research: Space Physics*, *116*(A05313).

Deng, Y., C. Y. Lin, Q. Zhu, and C. Sheng (2021), *Influence of Nonhydrostatic Processes on the Ionosphere-Thermosphere*, chap. 4, pp. 65–78, American Geophysical Union (AGU), doi:https://doi.org/10.1002/9781119815631.ch4.

Denton, M. H., J. E. Borovsky, R. M. Skoug, M. F. Thomsen, B. Lavraud, M. G. Henderson, R. L. McPherron, J. C. Zhang, and M. W. Liemohn (2006), Geomagnetic storms driven by icme- and cir-dominated solar wind, *Journal of Geophysical Research: Space Physics*, *111*(A7), doi:https://doi.org/10.1029/2005JA011436.

Dickinson, R. E., E. C. Ridley, and R. G. Roble (1981), A three-dimensional general circulation model of the thermosphere, *Journal of Geophysical Research: Space Physics*, *86*(A3), 1499–1512, doi:https://doi.org/10.1029/JA086iA03p01499.

Domingos, J., D. Jault, M. A. Pais, and M. Mandea (2017), The south atlantic anomaly throughout the solar cycle, *Earth and Planetary Science Letters*, *473*, 154–163, doi:https://doi.org/10.1016/j.epsl.2017.06.004.

Donahue, T. M., B. Guenther, and J. E. Blamont (1972), Noctilucent clouds in daytime: Circumpolar particulate layers near the summer mesopause, *Journal of Atmospheric Sciences*, *29*(6), 1205 – 1209, doi:10.1175/1520-0469(1972)029⟨1205:NCIDCP⟩2.0.CO;2.

Doornbos, E. (2011), Thermospheric density and wind determination from satellite dynamics (ph.d. thesis), *Delft University of Technology, Delft, The Netherlands*.

Doornbos, E. (2012), *Empirical Modelling of the Thermosphere*, pp. 21–57, Springer Berlin Heidelberg, Berlin, Heidelberg.

Doornbos, E., H. Klinkrad, and P. Visser (2005), Atmospheric density calibration using satellite drag observations, *Advances in Space Research*, *36*(3), 515–521, doi:https://doi.org/10.1016/j.asr.2005.02.009, satellite Dynamics in the Era of Interdisciplinary Space Geodesy.

Doornbos, E., H. Klinkrad, and P. Visser (2008), Use of two-line element data for thermosphere neutral density model calibration, *Advances in Space Research*, *41*(7), 1115–1122, doi:https://doi.org/10.1016/j.asr.2006.12.025.

Doornbos, E., J. van den IJssel, H. Luhr, M. Forster, and G. Koppenwallner (2010), Neutral density and crosswind determination from arbitrarily oriented multiaxis accelerometers on satellites, *Journal of Spacecraft and Rockets*, *47*(4), 580–589, doi:10.2514/1.48114.

Drob, D. P., et al. (2008), An empirical model of the earth's horizontal wind fields: Hwm07, *Journal of Geophysical Research: Space Physics*, *113*(A12), doi:https://doi.org/10.1029/2008JA013668.

Drob, D. P., et al. (2015), An update to the horizontal wind model (hwm): The quiet time thermosphere, *Earth and Space Science*, *2*(7), 301–319, doi:https://doi.org/10.1002/2014EA000089.

Dungey, J. W. (1961), Interplanetary magnetic field and the auroral zones, *Physical Review Letters*, *6*, 47–48.

Dunlop, M. W., et al. (2015), Multispacecraft current estimates at swarm, *Journal of Geophysical Research: Space Physics*, *120*(10), 8307–8316, doi:https://doi.org/10.1002/2015JA021707.

Emmert, J. T., R. R. Meier, J. M. Picone, J. L. Lean, and A. B. Christensen (2006), Thermospheric density 2002–2004: Timed/guvi dayside limb observations and satellite drag, *Journal of Geophysical Research: Space Physics*, *111*(A10), doi:https://doi.org/10.1029/2005JA011495.

Emmert, J. T., D. P. Drob, G. G. Shepherd, G. Hernandez, M. J. Jarvis, J. W. Meriwether, R. J. Niciejewski, D. P. Sipler, and C. A. Tepley (2008), Dwm07 global empirical model of upper thermospheric storm-induced disturbance winds,

Journal of Geophysical Research: Space Physics, *113*(A11), doi:https://doi.org/10.1029/2008JA013541.

fang Du, L., G. tao Yang, J. hong Wang, C. Yue, and L. xiang Chen (2017), Implementing a wind measurement doppler lidar based on a molecular iodine filter to monitor the atmospheric wind field over beijing, *Journal of Quantitative Spectroscopy and Radiative Transfer*, *188*, 3–11, doi:https://doi.org/10.1016/j.jqsrt.2016.07.013, advances in Atmospheric Light Scattering: Theory and Remote Sensing Techniques.

Fejer, B. G., J. T. Emmert, G. G. Shepherd, and B. H. Solheim (2000), Average daytime f region disturbance neutral winds measured by uars: Initial results, *Geophysical Research Letters*, *27*(13), 1859–1862, doi:https://doi.org/10.1029/2000GL003787.

Floberghagen, R., M. Fehringer, D. Lamarre, D. Muzi, B. Frommknecht, C. Steiger, J. Piñeiro, and A. da Costa (2011), Mission design, operation and exploitation of the gravity field and steady-state ocean circulation explorer mission, *Journal of Geodesy*, *85*, 749–758, doi:https://doi.org/10.007/s00190-011-0498-3.

Flury, J., S. Bettadpur, and B. D. Tapley (2008), Precise accelerometry onboard the grace gravity field satellite mission, *Advances in Space Research*, *42*(8), 1414–1423, doi:https://doi.org/10.1016/j.asr.2008.05.004.

Foppiano, A., Y.-I. Won, X. Torres, P. Flores, A. D. Veloso, and M. Arriagada (2016), Ionosonde and optical determinations of thermospheric neutral winds over the antarctic peninsula, *Advances in Space Research*, *58*(10), 2026–2036, doi:https://doi.org/10.1016/j.asr.2016.01.001, space and Geophysical Research related to Latin America - Part 2.

Forbes, J. M., G. Lu, S. Bruinsma, S. Nerem, and X. Zhang (2005), Thermosphere density variations due to the 15–24 april 2002 solar events from champ/star accelerometer measurements, *Journal of Geophysical Research: Space Physics*, *110*(A12), doi:https://doi.org/10.1029/2004JA010856.

Foster, C., H. Hallam, and J. Mason (2015), Orbit determination and differential-drag control of planet labs cubesat constellations.

Frederick, J., and P. Hays (1978), Magnetic ordering of the polar airglow, *Planetary and Space Science*, *26*(4), 339–345, doi:https://doi.org/10.1016/0032-0633(78)90117-4.

Fujii, J., T. Nakamura, T. Tsuda, and K. Shiokawa (2004), Comparison of winds measured by mu radar and fabry–perot interferometer and effect of oi5577 airglow height variations, *Journal of Atmospheric and Solar-Terrestrial Physics*, *66*(6), 573–583, doi:https://doi.org/10.1016/j.jastp.2004.01.010, dynamics and Chemistry of the MLT Region - PSMOS 2002 International Symposium.

Fuller-Rowell, T. J. (), A three-dimensional, time-dependent global model of the thermosphere, Ph.D. thesis, University College London.

Fuller-Rowell, T. J., and D. S. Evans (1987), Height-integrated pedersen and hall conductivity patterns inferred from the tiros-noaa satellite data, *Journal of Geophysical Research: Space Physics*, *92*(A7), 7606–7618, doi:https://doi.org/10.1029/JA092iA07p07606.

Fuller-Rowell, T. J., and D. Rees (1980), A three-dimensional time-dependent global model of the thermosphere, *Journal of Atmospheric Sciences*, *37*(11), 2545 – 2567, doi:10.1175/1520-0469(1980)037⟨2545:ATDTDG⟩2.0.CO;2.

Fuller-Rowell, T. J., M. V. Codrescu, R. J. Moffett, and S. Quegan (1994), Response of the thermosphere and ionosphere to geomagnetic storms, *Journal of Geophysical Research: Space Physics*, *99*(A3), 3893–3914, doi:https://doi.org/10.1029/93JA02015.

Fuller-Rowell, T. J., D. Rees, S. Quegan, R. J. MOffett, M. V. Codrescu, and G. H. Millward (1996), A coupled thermosphere-ionosphere model (ctim), Utah State University, Logan, UT.

Gao, Q., X. Chu, X. Xue, X. Dou, T. Chen, and J. Chen (2015), Lidar observations of thermospheric na layers up to 170 km with a descending tidal phase at lijiang (26.7°n, 100.0°e), china, *Journal of Geophysical Research: Space Physics*, *120*(10), 9213–9220, doi:https://doi.org/10.1002/2015JA021808.

Gardner, J., A. Broadfoot, W. McNeil, S. Lai, and E. Murad (1999), Analysis and modeling of the glo-1 observations of meteoric metals in the thermosphere, *Journal of Atmospheric and Solar-Terrestrial Physics*, *61*(7), 545–562, doi:https://doi.org/10.1016/S1364-6826(99)00013-9.

Gasperini, F., J. M. Forbes, E. N. Doornbos, and S. L. Bruinsma (2015), Wave coupling between the lower and middle thermosphere as viewed from timed and goce, *Journal of Geophysical Research: Space Physics*, *120*(7), 5788–5804, doi:https://doi.org/10.1002/2015JA021300.

Gedalin, M. (2001), Chapter 3.6 - shock waves in space, in *Handbook of Shock Waves*, edited by G. Ben-dor, O. Igra, and T. Elperin, pp. 455–483, Academic Press, Burlington, doi:https://doi.org/10.1016/B978-012086430-0/50010-5.

Goncharenko, L. P., and J. E. Salah (1998), Climatology and variability of the semidiurnal tide in teh lower thermosphere over millstone hill, *Journal of Geophysical Research*, *103*, 20,715–20,726.

Gondelach, D. J., and R. Linares (2020), Real-time thermospheric density estimation via two-line element data assimilation, *Space Weather*, *18*(2), e2019SW002,356, doi:https://doi.org/10.1029/2019SW002356, e2019SW002356 10.1029/2019SW002356.

Gong, Y., Q. Zhou, S. Zhang, N. Aponte, M. Sulzer, and S. Gonzalez (2012), Midnight ionosphere collapse at arecibo and its relationship to the neutral wind, electric field, and ambipolar diffusion, *Journal of Geophysical Research: Space Physics*, *117*(A8), doi:https://doi.org/10.1029/2012JA017530.

Gonzalez, W. D., J. A. Joselyn, Y. Kamide, H. W. Kroehl, G. Rostoker, B. T. Tsurutani, and V. M. Vasyliunas (1994), What is a geomagnetic storm?, *Journal of Geophysical Research: Space Physics*, *99*(A4), 5771–5792, doi:https://doi.org/10.1029/93JA02867.

Gonzalez, W. D., B. T. Tsurutani, and A. L. C. de Gonzalez (1999), Interplanetary origin of geomagnetic storms, *Space Science Reviews*, *88*, 529–562.

Gosling, J. T., J. R. Asbridge, S. J. Bame, and W. C. Feldman (1978), Solar wind stream interfaces, *Journal of Geophysical Research: Space Physics*, *83*(A4), 1401–1412, doi:https://doi.org/10.1029/JA083iA04p01401.

Guo, J.-P., Y. Deng, D.-H. Zhang, Y. Lu, C. Sheng, and S.-R. Zhang (2018), The effect of subauroral polarization streams on ionosphere and thermosphere during the 2015 st. patrick's day storm: Global ionosphere-thermosphere model simulations, *Journal of Geophysical Research: Space Physics*, *123*(3), 2241–2256, doi:https://doi.org/10.1002/2017JA024781.

Guo, Z., Z. Li, J. Farquhar, A. J. Kaufman, N. Wu, C. Li, R. R. Dickerson, and P. Wang (2010), Identification of sources and formation processes of atmospheric sulfate by sulfur isotope and scanning electron microscope measurements, *Journal of Geophysical Research: Atmospheres*, *115*(D7), doi:https://doi.org/10.1029/2009JD012893.

Haaser, R. A., R. Davidson, R. A. Heelis, G. D. Earle, S. Venkatraman, and J. Klenzing (2013), Storm time meridional wind perturbations in the equatorial upper thermosphere, *Journal of Geophysical Research: Space Physics*, *118*(5), 2756–2764, doi:https://doi.org/10.1002/jgra.50299.

Hamilton, D. C., G. Gloeckler, F. M. Ipavich, W. Stüdemann, B. Wilken, and G. Kremser (1988), Ring current development during the great geomagnetic storm of february 1986, *Journal of Geophysical Research: Space Physics*, *93*(A12), 14,343–14,355, doi:https://doi.org/10.1029/JA093iA12p14343.

Harding, B. J., J. J. Makela, J. Qin, D. J. Fisher, C. R. Martinis, J. Noto, and C. M. Wrasse (2017), Atmospheric scattering effects on ground-based measurements of thermospheric vertical wind, horizontal wind, and temperature, *Journal of Geophysical Research: Space Physics*, *122*, 7654–7669.

Harding, B. J., A. J. Ridley, and J. J. Makela (2019), Thermospheric weather as observed by ground-based fpis and modeled by gitm, *Journal of Geophysical Research: Space Physics*, *124*(2), 1307–1316, doi:https://doi.org/10.1029/2018JA026032.

Harris, M. J., N. F. Arnold, and A. D. Aylward (2002), A study into the effect of the diurnal tide on the structure of the background mesosphere and thermosphere using the new coupled middle atmosphere and thermosphere (cmat) general circulation model, *Annales Geophysicae*, *20*(2), 225–235, doi:10.5194/angeo-20-225-2002.

Häusler, K., H. Lühr, M. E. Hagan, A. Maute, and R. G. Roble (2010), Comparison of champ and time-gcm nonmigrating tidal signals in the thermospheric zonal wind, *Journal of Geophysical Research: Atmospheres*, *115*(D1), doi:https://doi.org/10.1029/2009JD012394.

Hays, P. B., D. L. Wu, and T. H. S. Team (1994), Observations of the diurnal tide from space, *Journal of the Atmospheric Sciences*, *51*, 3077–3093, doi:https://doi.org/10.1175/1520-0469(1994)051⟨3077:OOTDTF⟩2.0.CO;2.

He, C., Y. Yang, B. Carter, K. Zhang, A. Hu, W. Li, F. Deleflie, R. Norman, and S. Wu (2020), Impact of thermospheric mass density on the orbit prediction of leo satellites, *Space Weather*, *18*(1), e2019SW002,336, doi:https://doi.org/10.1029/2019SW002336, e2019SW002336 10.1029/2019SW002336.

He, C., et al. (2018), Review and comparison of empirical thermospheric mass density models, *Progress in Aerospace Sciences*, *103*, 31–51, doi:https://doi.org/10.1016/j.paerosci.2018.10.003.

Heath, D. F., and B. M. Schlesinger (1986), The mg 280 nm doublet as a monitor of changes in solar ultraviolet irradiance, *Journal of Geophysical Research*, *91*, 8672–8682.

Heber, B., T. Sanderson, and M. Zhang (1999), Corotating interaction regions, *Advances in Space Research*, *23*(3), 567–579, doi:https://doi.org/10.1016/S0273-1177(99)80013-1, the Transport of Galactic and Anomalous Cosmic Rays in the Heliosphere: Observations, Simulations and Theory.

Hedin, A. (1988), The atmospheric model in the region 90 to 2000 km, *Advances in Space Research*, *8*(5), 9–25, doi:https://doi.org/10.1016/0273-1177(88)90038-5.

Hedin, A., et al. (1996), Empirical wind model for the upper, middle and lower atmosphere, *Journal of Atmospheric and Terrestrial Physics*, *58*(13), 1421–1447, doi:https://doi.org/10.1016/0021-9169(95)00122-0.

Hedin, A. E. (1983), A revised thermospheric model based on mass spectrometer and incoherent scatter data: Msis-83, *Journal of Geophysical Research: Space Physics*, *88*(A12), 10,170–10,188, doi:https://doi.org/10.1029/JA088iA12p10170.

Hedin, A. E. (1987), Msis-86 thermospheric model, *Journal of Geophysical Research: Space Physics*, *92*(A5), 4649–4662, doi:https://doi.org/10.1029/JA092iA05p04649.

Hedin, A. E. (1989), Hot oxygen geocorona as inferred from neutral exospheric models and mass spectrometer measurements, *Journal of Geophysical Research*, *94*, 5523–5529.

Hedin, A. E. (1991), Extension of the msis thermosphere model into the middle and lower atmosphere, *Journal of Geophysical Research: Space Physics*, *96*(A2), 1159–1172, doi:https://doi.org/10.1029/90JA02125.

Hedin, A. E., C. A. Reber, G. P. Newton, N. W. Spencer, H. C. Brinton, H. G. Mayr, and W. E. Potter (1977a), A global thermospheric model based on mass spectrometer and incoherent scatter data, msise 2., composition, *Journal of Geophysical Research*, *82*.

Hedin, A. E., N. W. Spencer, and T. L. Killeen (1988), Empirical global model of upper thermosphere winds based on atmosphere and dynamics explorer satellite data, *Journal of Geophysical Research: Space Physics*, *93*(A9), 9959–9978, doi:https://doi.org/10.1029/JA093iA09p09959.

Hedin, A. E., et al. (1977b), A global thermospheric model based on mass spectrometer and incoherent scatter data msis, 1. n2 density and temperature, *Journal of Geophysical Research (1896-1977)*, *82*(16), 2139–2147, doi:https://doi.org/10.1029/JA082i016p02139.

Hedin, A. E., et al. (1991), Revised global model of thermosphere winds using satellite and ground-based observations, *Journal of Geophysical Research: Space Physics*, *96*(A5), 7657–7688, doi:https://doi.org/10.1029/91JA00251.

Heikkila, W. J. (2011), Chapter 5 - magnetopause, in *Earth's Magnetosphere*, edited by W. J. Heikkila, pp. 171–224, Elsevier, Amsterdam, doi:https://doi.org/10.1016/B978-0-444-52864-3.10005-X.

Heikkila, W. J., and J. D. Winningham (1971), Penetration of magnetosheath plasma to low altitudes through the dayside magnetospheric cusps, *Journal of Geophysical Research (1896-1977)*, *76*(4), 883–891, doi:https://doi.org/10.1029/JA076i004p00883.

Hocking, W., B. Fuller, and B. Vandepeer (2001), Real-time determination of meteor-related parameters utilizing modern digital technology, *Journal of Atmospheric and Solar-Terrestrial Physics*, *63*(2), 155–169, doi:https://doi.org/10.1016/S1364-6826(00)00138-3, radar applications for atmosphere and ionosphere research - PIERS 1999.

Holton, J. R. (1982), The role of gravity wave induced drag and diffusion in the momentum budget of the mesosphere, *Journal of Atmospheric Sciences*, *39*(4), 791 – 799, doi:10.1175/1520-0469(1982)039⟨0791:TROGWI⟩2.0.CO;2.

Hough, M. E. (2012), Precise orbit determination using satellite radar ranging, *Journal of Guidance, Control, and Dynamics*, *35*(4), 1048–1058, doi:10.2514/1.56873.

Hsu, V. W., J. P. Thayer, J. Lei, and W. Wang (2014), Formation of the equatorial thermosphere anomaly trough: Local time and solar cycle variations, *J. Geophys. Res.: Sp. Phys.*, *119*.

Illing, R. M. E., and A. J. Hundhausen (1985), Observation of a coronal transient from 1.2 to 6 solar radii, *Journal of Geophysical Research: Space Physics*, *90*(A1), 275–282, doi:https://doi.org/10.1029/JA090iA01p00275.

Innis, J. L., and M. Conde (2002a), Characterization of acoustic–gravity waves in the upper thermosphere using dynamics explorer 2 wind and temperature spectrometer (wats) and neutral atmosphere composition spectrometer (nacs) data, *Journal of Geophysical Research: Space Physics*, *107*(A12), SIA 1–1–SIA 1–22, doi:https://doi.org/10.1029/2002JA009370.

Innis, J. L., and M. Conde (2002b), High-latitude thermospheric vertical wind activity from dynamics explorer 2 wind and temperature spectrometer observations: Indications of a source region for polar cap gravity waves, *J. Geophys. Res.: Sp. Phys.*, *107*, 1172.

Ishii, M., M. Conde, R. W. Smith, M. Krynicki, E. Sagawa, and S. Watari (2001), Vertical wind observations with two fabry-perot interferometers at poker flat, alaska, *Journal of Geophysical Research: Space Physics*, *106*(A6), 10,537–10,551, doi:https://doi.org/10.1029/2000JA900148.

Ishii, M., M. Kubota, M. Conde, R. W. Smith, and M. Krynicki (2004), Vertical wind distribution in the polar thermosphere during horizontal e region experiment (hex) campaign, *J. Geophys. Res.*, *109*(A12311).

Jacchia, L. (1979), Cira 1972, recent atmospheric models, and improvements in progress, in *COSPAR: Space Research*, edited by M. RYCROFT, pp. 179–192, Pergamon, doi:https://doi.org/10.1016/B978-0-08-023417-5.50032-6.

Jacchia, L. G. (1965), vol. 8, Smithsonian Center for Astrophysics, Washington, D.C.

Jacchia, L. G. (1971), Smithsonian center for Astrophysics, Washington, D.C.

Jacchia, L. G. (1977), *Thermospheric Temperature, Density, and Composition: New Models. Special Report No. 375*, Smithsonian center for Astrophysics, Washington, D.C.

Jacchia, L. G., and J. Slowey (1963), *Smithsonian Contr. Astrophys.*, *8*, 1–99.

Jäggi, A., and D. Arnold (2017), *Precise Orbit Determination*, pp. 35–80, Springer International Publishing, Cham.

Jiang, G., et al. (2018), A comparison of quiet time thermospheric winds between fpi observations and model calculations, *Journal of Geophysical Research: Space Physics*, *123*(9), 7789–7805, doi:https://doi.org/10.1029/2018JA025424.

Jin, H., and T. Maruyama (2008), Temporary decrease in daytime f-region peak electron density due to eastward electric field penetration during magnetic storm, *Journal of Geophysical Research: Space Physics*, *113*(A5), doi:https://doi.org/10.1029/2006JA011928.

Jin, H., Y. Miyoshi, H. Fujiwara, H. Shinagawa, K. Terada, N. Terada, M. Ishii, Y. Otsuka, and A. Saito (2011), Vertical connection from the tropospheric activities to the ionospheric longitudinal structure simulated by a new earth's whole atmosphere-ionosphere coupled model, *Journal of Geophysical Research: Space Physics*, *116*(A1), doi:https://doi.org/10.1029/2010JA015925.

Johnson, F. S., W. B. Hanson, R. R. Hodges, W. R. Coley, G. R. Carignan, and N. W. Spencer (1995), Gravity waves near 300 km over the polar caps, *Journal of Geophysical Research: Space Physics*, *100*(A12), 23,993–24,002, doi:https://doi.org/10.1029/95JA02858.

Jones, R., and M. Rees (1973), Time dependent studies of the aurora—i. ion density and composition, *Planetary and Space Science*, *21*(4), 537–557, doi:https://doi.org/10.1016/0032-0633(73)90069-X.

Jones, S. R., L. A. Barnard, C. J. Scott, M. J. Owens, and J. Wilkinson (2017), Tracking cmes using data from the solar stormwatch project; observing deflections and other properties, *Space Weather*, *15*(9), 1125–1140, doi:https://doi.org/10.1002/2017SW001640.

Jones, S. R., C. J. Scott, L. A. Barnard, R. Highfield, C. J. Lintott, and E. Baeten (2020), The visual complexity of coronal mass ejections follows the solar cycle, *Space Weather*, *18*(10), e2020SW002,556, doi:https://doi.org/10.1029/2020SW002556, e2020SW002556 2020SW002556.

Jordanova, V. K., R. Ilie, and M. W. Chen (2020), Chapter 1 - introduction and historical background, in *Ring Current Investigations*, edited by V. K. Jordanova, R. Ilie, and M. W. Chen, pp. 1–13, Elsevier, doi:https://doi.org/10.1016/B978-0-12-815571-4.00001-9.

Joselyn, J. A., and B. T. Tsurutani (1990), Geomagnetic sudden impulses and storm sudden commencements: A note on terminology, *Eos, Transactions American Geophysical Union*, *71*(47), 1808–1809, doi:https://doi.org/10.1029/90EO00350.

Katus, R. M., M. W. Liemohn, D. L. Gallagher, A. Ridley, and S. Zou (2013), Evidence for potential and inductive convection during intense geomagnetic events using normalized superposed epoch analysis, *Journal of Geophysical Research: Space Physics*, *118*(1), 181–191, doi:https://doi.org/10.1029/2012JA017915.

Kazimirovsky, E., O. Pirog, and G. Vergasova (1999), The upper mesosphere/lower thermosphere wind field nonzonality as possible sign of the external forcing from above and from below, *Advances in Space Research*, *24*(5), 607–610, doi:https://doi.org/10.1016/S0273-1177(99)00478-0, mesopause Region Structure, Dynamics and Composition.

Keating, G. M., J. C. Leary, B. D. Green, O. M. Uy, R. C. Benson, R. E. Eriandson, T. E. Phillips, J. C. Lesbo, and M. T. Boies (1998), Neutral and ion drag effects

near the exobase: Msx satellite measurements of the he and o+, pp. 549–556, American Astronautical Society, San Diego, CA, USA.

Kessler, D. J., and B. G. Cour-Palais (1978), Collision frequency of artificial satellites: The creation of a debris belt, *Journal of Geophysical Research: Space Physics*, *83*(A6), 2637–2646, doi:https://doi.org/10.1029/JA083iA06p02637.

Khattatov, B. V., V. A. Yubin, M. A. Geller, P. B. Hays, and R. A. Vincent (1997), Diurnal migrating tide as seen by the high-resolution doppler imager/uars: 1. monthly mean global meridional winds, *Journal of Geophysical Research: Atmospheres*, *102*(D4), 4405–4422, doi:https://doi.org/10.1029/96JD03655.

Killeen, T. L., and P. B. Hays (1984), Doppler line profile analysis for a multichannel fabry-perot interferometer, *Appl. Opt.*, *23*(4), 612–620, doi:10.1364/AO.23.000612.

Killeen, T. L., P. B. Hays, N. W. Spencer, and L. E. Wharton (1982), Neutral winds in the polar thermosphere as measured from dynamics explorer, *Geophysical Research Letters*, *9*(9), 957–960, doi:https://doi.org/10.1029/GL009i009p00957.

Killeen, T. L., Y.-I. Won, R. J. Niciejewski, and A. G. Burns (1995), Upper thermosphere winds and temperatures in the geomagnetic polar cap: Solar cycle, geomagnetic activity, and interplanetary magnetic field dependencies, *Journal of Geophysical Research: Space Physics*, *100*(A11), 21,327–21,342, doi:https://doi.org/10.1029/95JA01208.

Killeen, T. L., Q. Wu, S. C. Solomon, D. A. Ortland, W. R. Skinner, R. J. Niciejewski, and D. A. Gell (2006), Timed doppler interferometer: Overview and recent results, *Journal of Geophysical Research: Space Physics*, *111*(A10), doi:https://doi.org/10.1029/2005JA011484.

Kim, J. H., Y. H. Kim, N. Ssessanga, S. H. Jeong, S. I. Moon, Y.-S. Kwak, and J. Y. Yun (2019), Regional ionosphere specification by assimilating ionosonde data into the sami2 model, *Advances in Space Research*, *64*(7), 1343–1357, doi:https://doi.org/10.1016/j.asr.2019.06.036.

King-Hele, D. (1987), Satellite orbits in an atmosphere: Theory and applications.

Kohl, H., and J. King (1967), Atmospheric winds between 100 and 700 km and their effects on the ionosphere, *Journal of Atmospheric and Terrestrial Physics*, *29*(9), 1045–1062, doi:https://doi.org/10.1016/0021-9169(67)90139-0.

Korotyshkin, D., E. Merzlyakov, O. Sherstyukov, and F. Valiullin (2019), Mesosphere/lower thermosphere wind regime parameters using a newly installed skiymet meteor radar at kazan (56°n, 49°e), *Advances in Space Research*, *63*(7), 2132–2143, doi:https://doi.org/10.1016/j.asr.2018.12.032.

Kozai, Y. (1959), The motion of a close earth satellite, *The Astronomical Journal*, *64*(397).

Kumar, A., and B. Badruddin (2021), Study of the evolution of the geomagnetic disturbances during the passage of high-speed streams from coronal holes in solar cycle 2009-2016, *Astrophysics and Space Science*, *366*(2), 21, doi:10.1007/s10509-021-03927-5.

Kurihara, J., et al. (2006), Observations of the lower thermospheric neutral temperature and density in the delta campaign, *Earth, Planets and Space*, *58*, 1123–1130, doi:10.1186/BF03352001.

Labs, P. (2015), Planet labs at a glance.

Larsen, M. (2003), Observation platforms — rockets, in *Encyclopedia of Atmospheric Sciences*, edited by J. R. Holton, pp. 1449–1454, Academic Press, Oxford, doi:https://doi.org/10.1016/B0-12-227090-8/00258-X.

Larsen, M. F., and J. W. Meriwether (2012), Vertical winds in the thermosphere, *Journal of Geophysical Research: Space Physics*, *117*(A9), doi:https://doi.org/10.1029/2012JA017843.

Lathuillére, C., and M. Menville (2010), Comparison of the observed and modeled low- to mid-latitude thermosphere response to magnetic activity: Effects of solar cycle and disturbance time delay, *Advances in Space Research*, *45*(9), 1093–1100, doi:https://doi.org/10.1016/j.asr.2009.08.016, special Issue: Recent Advances in Space Weather Monitoring, Modelling, and Forecasting.

Le, G., J. A. Slavin, and R. J. Strangeway (2010), Space technology 5 observations of the imbalance of regions 1 and 2 field-aligned currents and its implication to the cross-polar cap pedersen currents, *Journal of Geophysical Research: Space Physics*, *115*(A7), doi:https://doi.org/10.1029/2009JA014979.

Lei, J., J. P. Thayer, A. G. Burns, G. Lu, and Y. Deng (2010), Wind and temperature effects on thermosphere mass density response to the november 2004 geomagnetic storm, *Journal of Geophysical Research: Space Physics*, *115*(A5), doi:https://doi.org/10.1029/2009JA014754.

Lei, J., J. P. Thayer, G. Lu, A. G. Burns, W. Wang, E. K. Sutton, and B. A. Emery (2011), Rapid recovery of thermosphere density during the october 2003 geomagnetic storms, *Journal of Geophysical Research: Space Physics*, *116*(A3), doi:https://doi.org/10.1029/2010JA016164.

Lemoine, F., et al. (1997), *The Development of the NASA GSFC and NIMA Joint Geopotential Model*, pp. 461–469, Springer Berlin Heidelberg, Berlin, Heidelberg, doi:10.1007/978-3-662-03482-8_62.

Lindzen, R. S., and S. Chapman (1969), Atmospheric tides, *Space Science Reviews*, *10*(1), 3–188, doi:10.1007/BF00171584.

Lissauer, J. J., and I. de Pater (2019), *Fundamental Planetary Science: Physics, Chemistry and Habitability*, Cambridge University Press.

Liu, A. Z., Y. Guo, F. Vargas, and G. R. Swenson (2016a), First measurement of horizontal wind and temperature in the lower thermosphere (105–140 km) with a na lidar at andes lidar observatory, *Geophysical Research Letters*, *43*(6), 2374–2380, doi:https://doi.org/10.1002/2016GL068461.

Liu, H., E. Doornbos, and J. Nakashima (2016b), Thermospheric wind observed by goce: Wind jets and seasonal variations, *Journal of Geophysical Research: Space Physics*, *121*(7), 6901–6913, doi:https://doi.org/10.1002/2016JA022938.

Liu, H.-L. (2021), Effective vertical diffusion by atmospheric gravity waves, *Geophysical Research Letters*, *48*(1), e2020GL091,474, doi:https://doi.org/10.1029/2020GL091474, e2020GL091474 2020GL091474.

Liu, H.-L., et al. (2010), Thermosphere extension of the whole atmosphere community climate model, *Journal of Geophysical Research: Space Physics*, *115*(A12), doi:https://doi.org/10.1029/2010JA015586.

Liu, H.-L., et al. (2018), Development and validation of the whole atmosphere community climate model with thermosphere and ionosphere extension (waccm-x 2.0), *Journal of Advances in Modeling Earth Systems*, *10*(2), 381–402, doi:https://doi.org/10.1002/2017MS001232.

Liuzzo, L. R., A. J. Ridley, N. J. Perlongo, E. J. Mitchell, M. Conde, D. L. Hampton, W. A. Bristow, and M. J. Nicolls (2015a), High-latitude ionospheric drivers and their effects on wind patterns in the thermosphere, *Journal of Geophysical Research: Space Physics*, *120*(1), 715–735, doi:https://doi.org/10.1002/2014JA020553.

Liuzzo, L. R., A. J. Ridley, N. J. Perlongo, E. J. Mitchell, M. Conde, D. L. Hampton, W. A. Bristow, and M. J. Nicolls (2015b), High-latitude ionospheric drivers and their effects on wind patterns in the thermosphere, *Journal of Geophysical Research: Space Physics*, *120*(1), 715–735, doi:https://doi.org/10.1002/2014JA020553.

Lu, G., M. G. Mlynczak, L. A. Hunt, T. N. Woods, and R. G. Roble (2010), On the relationship of joule heating and nitric oxide radiative cooling in the thermosphere, *Journal of Geophysical Research: Space Physics*, *115*(A5), doi:https://doi.org/10.1029/2009JA014662.

Lu, X., A. Z. Liu, J. Oberheide, Q. Wu, T. Li, Z. Li, G. R. Swenson, and S. J. Franke (2011), Seasonal variability of the diurnal tide in the mesosphere and lower thermosphere over maui, hawaii (20.7n, 156.3w), *Journal of Geophysical Research: Atmospheres*, *116*(D17), doi:https://doi.org/10.1029/2011JD015599.

Lühr, H., and H. Liu (2006), The thermospheric response to geomagnetic storms, in *Proceedings of the ILWS Workshop*, edited by N. Gopalswamy and A. Bhattacharyya, p. 369, Goa, India.

Lyddane, R. H. (1963), Small eccentricities or inclinations in the brouwer theory of the artifical satellite, *The Astronomical Journal*, *68*(555).

Maeda, S., T. J. Fuller-Rowell, and D. S. Evans (1992), Heat budget of the thermosphere and temperature variations during the recovery phase of a geomagnetic storm, *Journal of Geophysical Research: Space Physics*, *97*(A10), 14,947–14,957, doi:https://doi.org/10.1029/92JA01368.

Makela, J., J. W. Meriwether, A. J. Ridley, M. Ciocca, and M. W. Castellez (2012), Large-scale measurements of thermospheric dynamics with a multisite fabry-perot interferometer network: Overview of plans and results from midlatitude measurements, *International Journal of Geophysics*, *2012*, doi:https://doi.org/10.1155/2012/872140.

Makela, J. J., D. J. Fisher, J. W. Meriwether, R. A. Buriti, and A. F. Medeiros (2013), Near-continual ground-based nighttime observations of thermospheric neutral winds and temperatures over equatorial brazil from 2009 to 2012, *Journal of Atmospheric and Solar-Terrestrial Physics*, *103*, 94–102.

Marshall, R. A., and C. M. Cully (2020), Chapter 7 - atmospheric effects and signatures of high-energy electron precipitation, in *The Dynamic Loss of Earth's Radiation Belts*, edited by A. N. Jaynes and M. E. Usanova, pp. 199–255, Elsevier, doi:https://doi.org/10.1016/B978-0-12-813371-2.00007-X.

Mason, J. P., and J. T. Hoeksema (2010), TESTING AUTOMATED SOLAR FLARE FORECASTING WITH 13 YEARS OF MICHELSON DOPPLER IMAGER MAGNETOGRAMS, *The Astrophysical Journal*, *723*(1), 634–640, doi:10.1088/0004-637x/723/1/634.

Matsushita, S. (1962), On geomagnetic sudden commencements, sudden impulses, and storm durations, *Journal of Geophysical Research (1896-1977)*, *67*(10), 3753–3777, doi:https://doi.org/10.1029/JZ067i010p03753.

Maus, S., et al. (2005), The 10th generation international geomagnetic reference field, *Physics of the Earth and Planetary Interiors*, *151*(3), 320–322, doi:https://doi.org/10.1016/j.pepi.2005.03.006.

Mayr, H. G., I. Harris, and N. W. Spencer (1978), Some properties of upper atmosphere dynamics, *Reviews of Geophysics*, *16*(4), 539–565, doi:https://doi.org/10.1029/RG016i004p00539.

Mayr, H. G., I. Harris, F. A. Herrero, N. W. Spencer, F. Varosi, and W. D. Pesnell (1990), Thermospheric gravity waves: observations and interpretation using the transfer function model (tfm), *Space Science Reviews*, *54*, 297–375.

McLaughlin, C. A., S. Mance, and T. Lichtenberg (2011), Drag coefficient estimation in orbit determination, *The Journal of the Astronautical Sciences*, *58*(3), 513–530, doi:10.1007/BF03321183.

Mehta, P. M., and R. Linares (2017), A methodology for reduced order modeling and calibration of the upper atmosphere, *Space Weather*, *15*(10), 1270–1287, doi:https://doi.org/10.1002/2017SW001642.

Mehta, P. M., A. Walker, E. Lawrence, R. Linares, D. Higdon, and J. Koller (2014), Modeling satellite drag coefficients with response surfaces, *Advances in Space Research*, *54*(8), 1590–1607, doi:https://doi.org/10.1016/j.asr.2014.06.033.

Mehta, P. M., A. C. Walker, E. K. Sutton, and H. C. Godinez (2017), New density estimates derived using accelerometers on board the champ and grace satellites, *Space Weather*, *15*(4), 558–576, doi:https://doi.org/10.1002/2016SW001562.

Mendaza, T., J. Blanco-Ávalos, and J. Martín-Torres (2017), Interplanetary coronal mass ejection effects on thermospheric density as inferred from international space station orbital data, *Advances in Space Research*, *60*(10), 2233–2251, doi:https://doi.org/10.1016/j.asr.2017.08.016.

Menvielle, M., T. Iyemori, A. Marchaudon, and M. Nosé (2011), *Geomagnetic Indices*, pp. 183–228, Springer Netherlands, Dordrecht, doi:10.1007/978-90-481-9858-0_8.

Mikhnevich, V. V., B. S. Danilin, A. I. Repnev, and V. A. Sokolov (1959), Some results of the determination of the structural parameters of the atmosphere using the third soviet artificial satellite, *Iskusstv. Sputnik Zemli*, *3*(84), 119–136.

Milan, S. E., G. Provan, and B. Hubert (2007), Magnetic flux transport in the dungey cycle: A survey of dayside and nightside reconnection rates, *Journal of Geophysical Research*, *112*(A01209), doi:10.1029/2006JA011642.

Miller, K. L., D. G. Torr, and P. G. Richards (1986), Meridional winds in the thermosphere derived from measurement of f 2 layer height, *Journal of Geophysical Research: Space Physics*, *91*(A4), 4531–4535, doi:https://doi.org/10.1029/JA091iA04p04531.

Millward, G. H., R. J. Moffett, S. Quegan, and T. J. Fuller-Rowell (1993), Effects of an atmospheric gravity wave on the midlatitude ionospheric f layer, *Journal of Geophysical Research: Space Physics*, *98*(A11), 19,173–19,179, doi:https://doi.org/10.1029/93JA02093.

Millward., G. H., R. J. Moffet, S. Quegan, and T. J. Fuller-Rowell (1996), A coupled thermosphere-ionosphere-plasmasphere model (ctip), pp. 239–279, Center for Atmospheric and Space Science, Utah State University, Logan, Utah.

Millward, G. H., I. C. F. Müller-Wodarg, A. D. Aylward, T. J. Fuller-Rowell, A. D. Richmond, and R. J. Moffett (2001), An investigation into the influence of tidal forcing on f region equatorial vertical ion drift using a global ionosphere-thermosphere model with coupled electrodynamics, *Journal of Geophysical Research: Space Physics*, *106*(A11), 24,733–24,744, doi:https://doi.org/10.1029/2000JA000342.

Mlynczak, M. G., L. A. Hunt, C. J. Mertens, B. Thomas Marshall, J. M. Russell III, T. Woods, R. Earl Thompson, and L. L. Gordley (2014), Influence of solar variability on the infrared radiative cooling of the thermosphere from 2002 to 2014, *Geophysical Research Letters*, *41*(7), 2508–2513, doi:https://doi.org/10.1002/2014GL059556.

Mlynczak, M. G., et al. (2010), Observations of infrared radiative cooling in the thermosphere on daily to multiyear timescales from the timed/saber instrument, *Journal of Geophysical Research: Space Physics*, *115*(A3), doi:https://doi.org/10.1029/2009JA014713.

Moe, K. (1967), The corpuscular heating effect observed by explorer 6 near sunspot maximum, *Planetary and Space Science*, *15*(12), 1821–1827, doi:https://doi.org/10.1016/0032-0633(67)90019-0.

Moe, K. (1973), Density and composition of the lower thermosphere, *Journal of Geophysical Research (1896-1977)*, *78*(10), 1633–1644, doi:https://doi.org/10.1029/JA078i010p01633.

Moe, K., and M. M. Moe (2005), Gas–surface interactions and satellite drag coefficients, *Planetary and Space Science*, *53*(8), 793–801, doi:https://doi.org/10.1016/j.pss.2005.03.005.

Moe, K., and M. M. Moe (2011), Operational models and drag-derived density trends in the thermosphere, *Space Weather*, *9*(5), doi:https://doi.org/10.1029/2010SW000650.

Moe, K., M. M. Moe, and S. D. Wallace (), Drag coefficients of spheres in free-molecular flow, *Advances in the Astronautical Sciences*, *93*(1), 391–406.

Moe, K., M. M. Moe, and C. J. Rice (2004), Simultaneous analysis of multi-instrument satellite measurements of atmospheric density, *Journal of Spacecraft and Rockets*, *41*, 849–853.

Müller-Wodarg, I. C. F., T. T. Koskinen, L. Moore, J. Serigano, R. V. Yelle, S. Hörst, J. H. Waite, and M. Mendillo (2019), Atmospheric waves and their possible effect on the thermal structure of saturn's thermosphere, *Geophysical Research Letters*, *46*(5), 2372–2380, doi:https://doi.org/10.1029/2018GL081124.

Nakamura, Y., et al. (2017), Measurement of thermospheric temperatures using omti fabry–perot interferometers with 70-mm etalon, *Earth, Planets and Space*, *69*(1), 57, doi:10.1186/s40623-017-0643-1.

Newton, G. P., R. Horowitz, and W. Priester (1965), Atmospheric density and temperature variations from the explorer xvii satellite and a further comparison with satellite drag, *Planetary and Space Science*, *13*(7), 599–616, doi:https://doi.org/10.1016/0032-0633(65)90042-5.

Nicholas, A., J. Picone, S. Thonnard, R. Meier, K. Dymond, and D. Drob (2000), A methodology for using optimal msis parameters retrieved from ssuli data to compute satellite drag on leo objects, *Journal of Atmospheric and Solar-Terrestrial Physics*, *62*(14), 1317–1326, doi:https://doi.org/10.1016/S1364-6826(00)00105-X, space Weather Week.

Nier, A. O., W. E. Potter, D. R. Hickman, and K. Mauersberger (1973), The open-source neutral-mass spectrometer on atmosphere explorer-c, -d, and -e, *Radio Science*, *8*(4), 271–276, doi:https://doi.org/10.1029/RS008i004p00271.

NIMA (2000), United states department of defense, world geodetic system 1984: Its definition and relationships with local geodetic systems, *Tech. Rep., TR8350.2*.

Nisbet, J., B. Wydra, C. Reber, and J. Luton (1977), Global exospheric temperatures and densities under active solar conditions, *Planetary and Space Science*, *25*(1), 59–69, doi:https://doi.org/10.1016/0032-0633(77)90118-0.

Nisbet, J. S. (1967), Neutral atmospheric temperatures from incoherent scatter observations, *Journal of Atmospheric Sciences*, *24*(5), 586–593, doi:10.1175/1520-0469(1967)024⟨0586:NATFIS⟩2.0.CO;2.

Oliveira, D. M., and E. Zesta (2019), Satellite orbital drag during magnetic storms, *Space Weather*, *17*(11), 1510–1533, doi:https://doi.org/10.1029/2019SW002287.

Oliveira, D. M., E. Zesta, P. W. Schuck, H. K. Connor, and E. K. Sutton (2017a), Ionosphere-thermosphere global time response to geomagnetic storms.

Oliveira, D. M., E. Zesta, P. W. Schuck, and E. K. Sutton (2017b), Thermosphere global time response to geomagnetic storms caused by coronal mass ejections, *Journal of Geophysical Research: Space Physics*, *122*(10), 10,762–10,782, doi:https://doi.org/10.1002/2017JA024006.

Oppenheim, M. M., A. F. vom Endt, and L. P. Dyrud (2000), Electrodynamics of meteor trail evolution in the equatorial e-region ionosphere, *Geophysical Research Letters*, *27*(19), 3173–3176, doi:https://doi.org/10.1029/1999GL000013.

Oppenheim, M. M., G. Sugar, N. O. Slowey, E. Bass, J. L. Chau, and S. Close (2009), Remote sensing lower thermosphere wind profiles using non-specular meteor echoes, *Geophysical Research Letters*, *36*(9), doi:https://doi.org/10.1029/2009GL037353.

Pardini, C., and L. Anselmo (2000), Comparison of thermospheric density models by satellite orbital decay analysis, Rio de Janeiro, Brazil.

Pardini, C., L. Anselmo, K. Moe, and M. Moe (2010), Drag and energy accommodation coefficients during sunspot maximum, *Advances in Space Research*, *45*(5), 638–650, doi:https://doi.org/10.1016/j.asr.2009.08.034.

Pardini, C., K. Moe, and L. Anselmo (2012), Thermospheric density model biases at the 23rd sunspot maximum, *Planetary and Space Science*, *67*(1), 130–146, doi:https://doi.org/10.1016/j.pss.2012.03.004.

Parks, G. K. (1991), *Physics of Space Plasma: An Introduction*, Basic Books.

Pawlowski, D. J., A. J. Ridley, I. Kim, and D. S. Bernstein (2008), Global model comparison with millstone hill during september 2005, *Journal of Geophysical Research: Space Physics*, *113*(A1), doi:https://doi.org/10.1029/2007JA012390.

Pedatella, N. M., and J. M. Forbes (2011), Electrodynamic response of the ionosphere to high-speed solar wind streams, *Journal of Geophysical Research: Space Physics*, *116*(A12), doi:https://doi.org/10.1029/2011JA017050.

Philbrick, C. P., F. Yang, F. A. Vargas, G. R. Swenson, and A. Z. Liu (2021), A na density lidar method and measurements of turbulence to 105 km at the andes lidar observatory, *Journal of Atmospheric and Solar-Terrestrial Physics*, *219*, 105,642, doi:https://doi.org/10.1016/j.jastp.2021.105642.

Picone, J. M., A. E. Hedin, D. P. Drob, and A. C. Aikin (2002), Nrlmsise-00 empirical model of the atmosphere: Statistical comparisons and scientific issues, *Journal of Geophysical Research: Space Physics*, *107*(A12), SIA 15–1–SIA 15–16, doi:https://doi.org/10.1029/2002JA009430.

Picone, J. M., J. T. Emmert, and J. L. Lean (2005a), Thermospheric densities derived from spacecraft orbits: Accurate processing of two-line element sets, *Journal of Geophysical Research: Space Physics*, *110*(A3), doi:https://doi.org/10.1029/2004JA010585.

Picone, J. M., J. T. Emmert, and J. L. Lean (2005b), Thermospheric densities derived from spacecraft orbits: Accurate processing of two-line element sets, *Journal of Geophysical Research: Space Physics*, *110*(A3), doi:https://doi.org/10.1029/2004JA010585.

Pilinski, M. D., G. Crowley, E. Sutton, and M. Codrescu (2016), Improved orbit determination and forecasts with an assimilative tool for satellite drag specification, in *Advanced Maui Optical and Space Surveillance Technologies Conference*, Wailea, HI.

Priester, W., M. Roemer, and H. Volland (1967), The physical behavior of the upper atmosphere deduced from satellite drag data, *Space Science Reviews*, *6*, 707–780, doi:10.1007/BF00222406.

Proctor, J. L., S. L. Brunton, and J. N. Kutz (2016), Dynamic mode decomposition with control, *SIAM Journal on Applied Dynamical Systems*, *15*, 142–161.

Prölss, G. W. (1980), Magnetic storm associated perturbations of the upper atmosphere: Recent results obtained by satellite-borne gas analyzers, *Reviews of Geophysics*, *18*(1), 183–202, doi:https://doi.org/10.1029/RG018i001p00183.

Qian, L., S. C. Solomon, and T. J. Kane (2009), Seasonal variation of thermospheric density and composition, *Journal of Geophysical Research: Space Physics*, *114*(A1), doi:https://doi.org/10.1029/2008JA013643.

Qian, L., W. Wang, A. G. Burns, P. C. Chamberlin, A. Coster, S.-R. Zhang, and S. C. Solomon (2019), Solar flare and geomagnetic storm effects on the thermosphere and ionosphere during 6–11 september 2017, *Journal of Geophysical Research: Space Physics*, *124*(3), 2298–2311, doi:https://doi.org/10.1029/2018JA026175.

Ramesh, K. B. (2010), CORONAL MASS EJECTIONS AND SUNSPOTS—SOLAR CYCLE PERSPECTIVE, *The Astrophysical Journal*, *712*(1), L77–L80, doi:10.1088/2041-8205/712/1/l77.

Rees, D. (1985), Theoretical thermosphere models, *Advances in Space Research*, *5*(7), 215–228, doi:https://doi.org/10.1016/0273-1177(85)90378-3.

Rees, M. H. (1989), Physics and chemistry of the upper atmosphere, Cambridge University Press, New York, NY 10022, USA.

Reigber, C., H. Lühr, and P. Schwintzer (2002), Champ mission status, *Advances in Space Research*, *30*(2), 129–134, doi:https://doi.org/10.1016/S0273-1177(02)00276-4.

Richards, P. G. (1991), An improved algorithm for determining neutral winds from the height of the f 2 peak electron density, *Journal of Geophysical Research: Space Physics*, *96*(A10), 17,839–17,846, doi:https://doi.org/10.1029/91JA01467.

Richmond, A. D. (1995), Ionosphere electrodynamics using apex coordinates, *Journal of Geomagnetism and Geoelectricity*, *47*, 191–212, doi:https://doi.org/10.5636/jgg.47.191.

Richmond, A. D., and S. Matsushita (1975), Thermospheric response to a magnetic substorm, *Journal of Geophysical Research (1896-1977)*, *80*(19), 2839–2850, doi:https://doi.org/10.1029/JA080i019p02839.

Richmond, A. D., E. C. Ridley, and R. G. Roble (1992), A thermosphere/ionosphere general circulation model with coupled electrodynamics, *Geophysical Research Letters*, *19*(6), 601–604, doi:https://doi.org/10.1029/92GL00401.

Ridley, A., Y. Deng, and G. Tóth (2006), The global ionosphere–thermosphere model, *Journal of Atmospheric and Solar-Terrestrial Physics*, *68*(8), 839–864, doi:https://doi.org/10.1016/j.jastp.2006.01.008.

Rishbeth, H. (1972), Thermospheric winds and the f-region: A review, *Journal of Atmospheric and Terrestrial Physics*, *34*(1), 1–47, doi:https://doi.org/10.1016/0021-9169(72)90003-7.

Rishbeth, H. (1979), Ion-drag effects in the thermosphere, *Journal of Atmospheric and Terrestrial Physics*, *41*(7), 885–894, doi:https://doi.org/10.1016/0021-9169(79)90130-2.

Rishbeth, H., and I. C. F. Müller-Wodarg (1999), Vertical circulation and thermospheric composition: a modelling study, *Annales Geophysicae*, *17*(6), 794–805, doi:10.1007/s00585-999-0794-x.

Rishbeth, H., R. Moffett, and G. Bailey (1969), Continuity of air motion in the mid-latitude thermosphere, *Journal of Atmospheric and Terrestrial Physics*, *31*(8), 1035–1047, doi:https://doi.org/10.1016/0021-9169(69)90103-2.

Rishbeth, H., T. Fuller-Rowell, and D. Rees (1987), Diffusive equilibrium and vertical motion in the thermosphere during a severe magnetic storm : A computational study, *Planetary and Space Science*, *35*(9), 1157–1165, doi:https://doi.org/10.1016/0032-0633(87)90022-5.

Roble, R. (2003), Thermosphere, in *Encyclopedia of Atmospheric Sciences*, edited by J. R. Holton, pp. 2282–2290, Academic Press, Oxford, doi:https://doi.org/10.1016/B0-12-227090-8/00408-5.

Roble, R. G., and E. C. Ridley (1994a), A thermosphere-ionosphere-mesosphere-electrodynamics general circulation model (time-gcm): Equinox solar cycle minimum simulations (30–500 km), *Geophysical Research Letters*, *21*(6), 417–420, doi:https://doi.org/10.1029/93GL03391.

Roble, R. G., and E. C. Ridley (1994b), A thermosphere-ionosphere-mesosphere-electrodynamics general circulation model (time-gcm): Equinox solar cycle minimum simulations (30–500 km), *Geophysical Research Letters*, *21*(6), 417–420, doi:https://doi.org/10.1029/93GL03391.

Roble, R. G., E. C. Ridley, A. D. Richmond, and R. E. Dickinson (1988), A coupled thermosphere/ionosphere general circulation model, *Geophysical Research Letters*, *15*(12), 1325–1328, doi:https://doi.org/10.1029/GL015i012p01325.

Rodrigo, R., J. S. Nisbet, and E. Battaner (1981), The effect of horizontal winds upon the chemical composition of the lower thermosphere at high latitude, *Journal of Geophysical Research: Space Physics*, *86*(A5), 3501–3508, doi:https://doi.org/10.1029/JA086iA05p03501.

Rodrigues, M., B. Foulon, F. Liorzou, and P. Touboul (2003), Flight experience on champ and grace with ultra-sensitive accelerometers and return for lisa, *Classical and Quantum Gravity*, *20*, S291–S300, doi:10.1088/0264-9381/20/10/332.

Romanazzo, M., C. Steiger, V. Tran, A. Niño, P. Emanuelli, R. Floberghagen, and M. Fehringer (2013), Low orbit operations of esa's gravity mission goce, Munich, Germany.

Roy, A. E. (1988), *Orbital Motion*, 3rd ed., Institute of Physics Publishing.

Ruf, C., S. Gleason, Z. Jelenak, S. Katzberg, A. Ridley, R. Rose, J. Scherrer, and V. Zavorotny (2013), The nasa ev-2 cyclone global navigation satellite system (cygnss) mission, in *2013 IEEE Aerospace Conference*, pp. 1–7, doi:10.1109/AERO.2013.6497202.

Safyan, M. (2015), Overview of the planet labs constellation of earth imaging satellites.

Salah, J., and L. Goncharenko (2001), Search for geomagnetic storm effects on lower thermospheric winds at midlatitudes, *Journal of Atmospheric and Solar-Terrestrial Physics*, *63*(9), 951–963, doi:https://doi.org/10.1016/S1364-6826(00)00192-9, mesosphere-Thermosphere-Ionosphere Coupling and Energetics.

Salah, J. E., R. M. Johnson, and C. A. Tepley (1991), Coordinated incoherent scatter radar observations of the semidiurnal tide in the lower thermosphere, *Journal of Geophysical Research*, *96*, 1071–1080.

Schunk, R. W., and A. F. Nagy (2018), Neutral atmospheres, in *Ionospheres: Physics, Plasma Physics, and Chemistry*, edited by J. T. Houghton, M. J. Rycroft, and A. J. Dessler, second edition ed., pp. 289–334, Cambridge University Press.

Shen, H.-W., J.-H. Shue, J. Dombeck, and T.-P. Lee (2021), An evaluation of space weather conditions for formosat-3 satellite anomalies, *Earth, Planets and Space*, *73*(1), 111, doi:10.1186/s40623-021-01429-w.

Sheng, C., G. Lu, S. C. Solomon, W. Wang, E. Doornbos, L. A. Hunt, and M. G. Mlynczak (2017), Thermospheric recovery during the 5 april 2010 geomagnetic storm, *Journal of Geophysical Research: Space Physics*, *122*(4), 4588–4599, doi:https://doi.org/10.1002/2016JA023520.

Shepherd, G. G., et al. (1993), Windii, the wind imaging interferometer on the upper atmosphere research satellite, *Journal of Geophysical Research: Atmospheres*, *98*(D6), 10,725–10,750, doi:https://doi.org/10.1029/93JD00227.

Shi, C., W. Li, M. Li, Q. Zhao, and J. Sang (2015), Calibrating the scale of the nrlmsise00 model during solar maximum using the two line elements dataset, *Advances in Space Research*, *56*(1), 1–9, doi:https://doi.org/10.1016/j.asr.2015.03.024.

Shim, J. S., et al. (2012), Cedar electrodynamics thermosphere ionosphere (eti) challenge for systematic assessment of ionosphere/thermosphere models: Electron density, neutral density, nmf2, and hmf2 using space based observations, *Space Weather*, *10*(10), doi:https://doi.org/10.1029/2012SW000851.

Shiokawa, K., Y. Otsuka, S. Oyama, S. Nozawa, M. Satoh, Y. Katoh, Y. Hamaguchi, Y. Yamamoto, and J. Meriwether (2012), Development of low-cost sky-scanning fabry-perot interferometers for airglow and auroral studies, *Earth, Planets and Space*, *64*(11), 1033–1046, doi:10.5047/eps.2012.05.004.

Siemes, C. (2020), Swarm satellite thermo-optical properties and external geometry.

Siemes, C., et al. (2016), Swarm accelerometer data processing from raw accelerations to thermospheric neutral densities, *Earth, Planets and Space*, *68*(1), 92, doi:10.1186/s40623-016-0474-5.

Singh, Y., and Badruddin (2006), Statistical considerations in superposed epoch analysis and its applications in space research, *Journal of Atmospheric and Solar-Terrestrial Physics*, *68*(7), 803–813, doi:https://doi.org/10.1016/j.jastp.2006.01.007.

Sinnhuber, M., H. Nieder, and N. Wieters (2012), Energetic particle precipitation and the chemistry of the mesosphere/lower thermosphere, *Surveys in Geophysics*, *33*, 1281–1334, doi:https://doi.org/10.1007/s10712-012-9201-3.

Snevkik, K., N. Østgaard, P. Tenfjord, J. P. Reistad, K. M. Laundal, S. E. Milan, and S. E. Haaland (), Dayside and nightside magnetic field responses at 780 km altitude to dayside reconnection, *Journal of Geophysical Research: Space Physics*, *122*, 1670–1689, doi:10.1002/2016JA023177.

Solomon, S., and R. Roble (2015), Thermosphere, in *Encyclopedia of Atmospheric Sciences (Second Edition)*, edited by G. R. North, J. Pyle, and F. Zhang, second edition ed., pp. 402–408, Academic Press, Oxford, doi:https://doi.org/10.1016/B978-0-12-382225-3.00408-4.

Sośnica, K., A. Jäggi, D. Thaller, G. Beutler, and R. Dach (2014), Contribution of starlette, stella, and ajisai to the slr-derived global reference frame, *Journal of Geodesy*, *88*(8), 789–804, doi:10.1007/s00190-014-0722-z.

Spencer, N. W., L. H. Brace, and D. W. Grimes (1973), The atmosphere explorer spacecraft system, *Radio Science*, *8*(4), 267–269, doi:https://doi.org/10.1029/RS008i004p00267.

Spencer, N. W., L. E. Wharton, H. B. Niemann, A. E. Hedin, G. R. Carignan, and J. C. Maurer (1981), The dynamics explorer wind and temperature spectrometer, *Space Science Instrumentation*, *5*, 417–428.

Spencer, N. W., L. E. Warton, G. R. Carignan, and M. J. C. (1982a), Thermosphere zonal winds, vertical motions and temperature as measured from dynamics explorer, *Geophysical Research Letters*, *9*(9), 953–956, doi:https://doi.org/10.1029/GL009i009p00953.

Spencer, N. W., L. E. Wharton, G. R. Carignan, and J. C. Maurer (1982b), Thermosphere zonal winds, vertical motions and temperature as measured from dynamics explorer, *Geophys. Res. Lett.*, *9*(9), 953–956.

Storz, M. F., B. R. Bowman, M. J. I. Branson, S. J. Casali, and W. K. Tobiska (2005), High accuracy satellite drag model (hasdm), *Advances in Space Research*, *36*(12), 2497–2505, doi:https://doi.org/10.1016/j.asr.2004.02.020, space Weather.

Strugarek, D., K. Sośnica, and A. Jäggi (2019), Characteristics of goce orbits based on satellite laser ranging, *Advances in Space Research*, *63*(1), 417–431, doi:https://doi.org/10.1016/j.asr.2018.08.033.

Sugiara, M., and S. Chapman (1960), The average morphology of geomagnetic storms with sudden commencements, *Abh. Akad. Wiss. Göttingen, Math.-phys., Kl., Sonderheft, Spec. Issue 4*, p. 53.

Sutton, E. K., R. S. Nerem, and J. M. Forbes (2007), Density and winds in the thermosphere deduced from accelerometer data, *Journal of Spacecraft and Rockets*, *44*(6), 1210–1219, doi:10.2514/1.28641.

Sutton, E. K., J. M. Forbes, and D. J. Knipp (2009), Rapid response of the thermosphere to variations in joule heating, *Journal of Geophysical Research: Space Physics*, *114*(A4), doi:https://doi.org/10.1029/2008JA013667.

Sutton, E. K., J. P. Thayer, M. D. Pilinski, S. M. Mutschler, T. E. Berger, V. Nguyen, and D. Masters (2021), Toward accurate physics-based specifications of neutral density using gnss-enabled small satellites, *Space Weather*, *19*(6), e2021SW002,736, doi:https://doi.org/10.1029/2021SW002736, e2021SW002736 2021SW002736.

Tapping, K. F., and B. DeTracey (1990), The origin of the 10.7 cm flux, *Solar Physics*, *127*(2), 321–332, doi:10.1007/BF00152171.

Titheridge, J. E. (1995), Winds in the ionosphere-a review, *Journal of Atmospheric and Terrestrial Physics*, *57*, 1681–1714.

Tobiska, W., T. Woods, F. Eparvier, R. Viereck, L. Floyd, D. Bouwer, G. Rottman, and O. White (2000), The solar2000 empirical solar irradiance model and forecast tool, *Journal of Atmospheric and Solar-Terrestrial Physics*, *62*(14), 1233–1250, doi:https://doi.org/10.1016/S1364-6826(00)00070-5, space Weather Week.

Touboul, P. (2003a), Microscope instrument development, lessons for goce, *108*, 393–408, doi:10.1023/A:1026152114467.

Touboul, P. (2003b), Microscope instrument development, lessons for goce, *Space Science Reviews*, *108*, 393–408.

Touboul, P., B. Foulon, M. Rodrigues, and J. Marque (2004), In orbit nano-g measurements, lessons for future space missions, *Aerospace Science and Technology*, *8*(5), 431–441, doi:https://doi.org/10.1016/j.ast.2004.01.006.

Trinks, H., and U. von Zahn (1975), The esro 4 gas analyzer, *Review of Scientific Instruments*, *46*, 213–217, doi:10.1063/1.1134170.

Tsuda, T. T., S. Nozawa, A. Brekke, Y. Ogawa, T. Motoba, R. Roble, and R. Fujii (2007), An ion drag contribution to the lower thermospheric wind in the summer polar region, *Journal of Geophysical Research: Space Physics*, *112*(A6), doi:https://doi.org/10.1029/2006JA011785.

Tsurutani, B. T., W. D. Gonzalez, A. L. C. Gonzalez, F. Tang, J. K. Arballo, and M. Okada (1995), Interplanetary origin of geomagnetic activity in the declining phase of the solar cycle, *Journal of Geophysical Research: Space Physics*, *100*(A11), 21,717–21,733, doi:https://doi.org/10.1029/95JA01476.

Tsurutani, B. T., G. S. Lakhina, J. S. Pickett, F. L. Guarnieri, N. Lin, and B. E. Goldstein (2005), Nonlinear alfvén waves, discontinuities, proton perpendicular acceleration, and magnetic holes/decreases in interplanetary space and the magnetosphere: intermediate shocks?, *Nonlinear Processes in Geophysics*, *12*(3), 321–336, doi:10.5194/npg-12-321-2005.

Tucker-Hood, K., et al. (2015), Validation of a priori cme arrival predictions made using real-time heliospheric imager observations, *Space Weather*, *13*(1), 35–48, doi:https://doi.org/10.1002/2014SW001106.

Turner, N. E., W. D. Cramer, S. K. Earles, and B. A. Emery (2009), Geoefficiency and energy partitioning in cir-driven and cme-driven storms, *Journal of Atmospheric and Solar-Terrestrial Physics*, *71*(10), 1023–1031, doi:https://doi.org/10.1016/j.jastp.2009.02.005, high Speed Solar Wind Streams and Geospace Interactions.

Vadas, S. L., and G. Crowley (2017), Neutral wind and density perturbations in the thermosphere created by gravity waves observed by the tiddbit sounder, *Journal of Geophysical Research: Space Physics*, *122*(6), 6652–6678, doi:https://doi.org/10.1002/2016JA023828.

Vallada, D. A., and P. Crawford (2008), Sgp4 orbit determination.

Vallado, D. A., and D. Finkleman (2014), A critical assessment of satellite drag and atmospheric density modeling, *Acta Astronautica*, *95*, 141–165, doi:https://doi.org/10.1016/j.actaastro.2013.10.005.

Vallado, D. A., and W. D. McClain (2007), Fundamentals of astrodynamics and applications, Microcosm Press, Hawthorne, CA, USA.

Vallado, D. A., P. Crawford, R. Husjak, and T. S. Kelso (2006), Revisiting spacetrack report #3, *Astrodynamics Specialist Conference*.

Venkataramani, K., J. D. Yonker, and S. M. Bailey (2016), Contribution of chemical processes to infrared emissions from nitric oxide in the thermosphere, *Journal of Geophysical Research: Space Physics*, *121*(3), 2450–2461, doi:https://doi.org/10.1002/2015JA022055.

Viereck, R., L. Puga, D. McMullin, D. Judge, M. Weber, and W. K. Tobiska (2001), The mg ii index: A proxy for solar euv, *Geophysical Research Letters*, *28*(7), 1343–1346.

Visser, P. N. A. M., and J. A. A. v. d. IJssel (2016), Calibration and validation of individual goce accelerometers by precise orbit determination, *Journal of Geodesy*, *90*(1), 1–13, doi:10.1007/s00190-015-0850-0.

Visser, T., E. Doornbos, C. de Visser, P. Visser, and B. Fritsche (2018), Torque model verification for the goce satellite, *Advances in Space Research*, *62*, 1114–1136.

Visser, T., G. March, E. Doornbos, C. de Visser, and P. Visser (2019a), Horizontal and vertical thermospheric cross-wind from goce linear and angular accelerations, *Advances in Space Research*, *63*(10), 3139–3153, doi:https://doi.org/10.1016/j.asr.2019.01.030.

Visser, T., G. March, E. N. Doornbos, C. C. de Visser, and P. N. A. M. Visser (2019b), Characterization of thermospheric vertical wind activity at 225- to 295-km altitude using goce data and validation against explorer missions, *Journal of Geophysical Research: Space Physics*, *124*(6), 4852–4869, doi:https://doi.org/10.1029/2019JA026568.

Visser, T., G. March, E. N. Doornbos, C. C. de Visser, and P. N. A. M. Visser (2019c), Characterization of thermospheric vertical wind activity at 225-km to 295-km altitude using goce data and validation against explorer missions, *J. Geophys. Res.: Sp. Phys.*, *124*, 4852–4869.

Waheed, M. A., P. A. Khan, and A. K. Gwal (2019), Distribution of intense, moderate and weak geomagnetic storms over the solar cycle, *Indian Journal of Physics*, *93*, 1103–1112, doi:10.1007/s12648-019-01379-w.

Walker, J. C. G. (1965), Analytic representation of upper atmosphere densities based on jacchia's static diffusion models, *Journal of Atmospheric Sciences*, *22*(4), 462 – 463, doi:10.1175/1520-0469(1965)022⟨0462:AROUAD⟩2.0.CO;2.

Wang, H., A. J. Ridley, and J. Zhu (2015), Theoretical study of zonal differences of electron density at midlatitudes with gitm simulation, *Journal of Geophysical Research: Space Physics*, *120*(4), 2951–2966, doi:https://doi.org/10.1002/2014JA020790.

Wang, H., K. D. Zhang, X. Wan, and H. Lühr (2017), Universal time variation of high-latitude thermospheric disturbance wind in response to a substorm, *Journal of Geophysical Research: Space Physics*, *122*(4), 4638–4653, doi:https://doi.org/10.1002/2016JA023630.

Wang, H. B. (2010), The application of satellite borne accelerometer data to the study of the upper atmosphere, *Acta Astronomica Sinica*, *51*(4), 435–436.

Wang, W., A. G. Burns, M. Wiltberger, S. C. Solomon, and T. L. Killeen (2008), Altitude variations of the horizontal thermospheric winds during geomagnetic storms, *Journal of Geophysical Research: Space Physics*, *113*(A2), doi:https://doi.org/10.1029/2007JA012374.

Wang, Z., Q. Hu, Q. Zhong, and Y. Wang (2018), Linear multistep f10.7 forecasting based on task correlation and heteroscedasticity, *Earth and Space Science*, *5*(12), 863–874, doi:https://doi.org/10.1029/2018EA000393.

Weimer, D. R. (2005), Improved ionospheric electrodynamic models and application to calculating joule heating rates, *Journal of Geophysical Research: Space Physics*, *110*(A5), doi:https://doi.org/10.1029/2004JA010884.

Wescott, E. M., H. Stenbaek-Nielsen, M. Conde, M. Larsen, and D. Lummerzheim (2006), The hex experiment: Determination of the neutral wind field from 120 to 185 km altitude near a stable premidnight auroral arc by triangulating the drift of rocket-deployed chemical trails, *Journal of Geophysical Research: Space Physics*, *111*(A9), doi:https://doi.org/10.1029/2005JA011002.

Weygand, J. M., E. Zesta, and O. Troshichev (2014), Auroral electrojet indices in the northern and southern hemispheres: A statistical comparison, *Journal of Geophysical Research: Space Physics*, *119*(6), 4819–4840, doi:https://doi.org/10.1002/2013JA019377.

Wimmer-Schweingruber, R. F., R. von Steiger, and R. Paerli (1997), Solar wind stream interfaces in cororating interaction regions: Swics/ulysses results, *Journal of Geophysical Research*, *102*(A8), 17,407–17,417.

Woods, T. N., et al. (2012), Extreme ultraviolet variability experiment (eve) on the solar dynamics observatory (sdo): Overview of science objectives, instrument design, data products, and model developments, *Solar Physics*, *215*, 115–143, doi:10.1007/s11207-009-9487-6.

Wrenn, G. L. (1987), Time-weighted accumulations ap(τ) and kp((τ), *Journal of Geophysical Research: Space Physics*, *92*(A9), 10,125–10,129, doi:https://doi.org/10.1029/JA092iA09p10125.

Wu, Q., W. Wang, R. G. Roble, I. Häggström, and A. Strømme (2012), First daytime thermospheric wind observation from a balloon-borne fabry-perot interferometer over kiruna (68n), *Geophysical Research Letters*, *39*(14), doi:https://doi.org/10.1029/2012GL052533.

Wu, S.-H., J. Yin, B. Liu, J. Liu, R. Li, X. Wang, C. Feng, and K. Zhang (2014), Coherent doppler lidar to investigate wind turbulence, doi:10.1117/2.1201412.005658.

Wyatt, S. P. (1961), The effect of radiation pressure on the secular acceleration of satellites, in *SAO Special Report #60*, Smithsonian Institution, Washington, D.C.

Xu, H., K. Shiokawa, S.-i. Oyama, and Y. Otsuka (2019), Thermospheric wind variations observed by a fabry–perot interferometer at tromsø, norway, at substorm onsets, *Earth, Planets and Space*, *71*(1), 93, doi:10.1186/s40623-019-1072-0.

Yermolaev, Y. I., I. G. Lodkina, N. S. Nikolaeva, and M. Y. Yermolaev (2014), Influence of the interplanetary driver type on the durations of the main and recovery phases of magnetic storms, *Journal of Geophysical Research: Space Physics*, *119*(10), 8126–8136, doi:https://doi.org/10.1002/2014JA019826.

Yin, Z., H. Zou, Y. Ye, Q. Zong, and Y. Wang (2019), Superposed epoch analysis of the energetic electron flux variations during cirs measured by bd-ies, *Space Weather*, *17*(12), 1765–1782, doi:https://doi.org/10.1029/2019SW002296.

Yiğit, E., and A. J. Ridley (2011a), Role of variability in determining the vertical wind speeds and structure, *Journal of Geophysical Research: Space Physics*, *116*(A12), doi:https://doi.org/10.1029/2011JA016714.

Yiğit, E., and A. J. Ridley (2011b), Effects of high-latitude thermosphere heating at various scale sizes simulated by a nonhydrostatic global thermosphere–ionosphere model, *Journal of Atmospheric and Solar-Terrestrial Physics*, *73*(5), 592–600, doi:https://doi.org/10.1016/j.jastp.2010.12.003.

Yuan, L., S. Jin, and A. Calabia (2019), Distinct thermospheric mass density variations following the september 2017 geomagnetic storm from grace and swarm, *Journal of Atmospheric and Solar-Terrestrial Physics*, *184*, 30–36, doi:https://doi.org/10.1016/j.jastp.2019.01.007.

Yuan, W., X. Liu, J. Xu, Q. Zhou, G. Jiang, and R. Ma (2013), Fpi observations of nighttime mesospheric and thermospheric winds in china and their comparisons with hwm07, *Annales Geophysicae*, *31*(8), 1365–1378, doi:10.5194/angeo-31-1365-2013.

Zesta, E., and D. M. Oliveira (2019), Thermospheric heating and cooling times during geomagnetic storms, including extreme events, *46*, 12,739–12,746, doi:10.1029/2019GL085120.

Zhang, Q.-H., M. Lockwood, J. C. Foster, S.-R. Zhang, B.-C. Zhang, I. W. McCrea, J. Moen, M. Lester, and J. M. Ruohoniemi (2015), Direct observations of the full dungey convection cycle in the polar ionosphere for southward interplanetary magnetic field conditions, *Journal of Geophysical Research: Space Physics*, *120*(6), 4519–4530, doi:https://doi.org/10.1002/2015JA021172.

Zhao, S., J. Urbina, L. Dyrud, and R. Seal (2011), Multilayer detection and classification of specular and nonspecular meteor trails, *Radio Science*, *46*(6), doi:https://doi.org/10.1029/2010RS004548.

Zhou, Q. H., M. P. Sulzer, and C. A. Tepley (1997), An analysis of tidal and planetary waves in the neutral winds and temperature observed at low-latitude e region heights, *Journal of Geophysical Research: Space Physics*, *102*(A6), 11,491–11,505, doi:https://doi.org/10.1029/97JA00440.

Zhou, S., X. Luan, and X. Dou (2016), Solar activity dependence of nightside aurora in winter conditions, *Journal of Geophysical Research: Space Physics*, *121*(2), 1619–1626, doi:https://doi.org/10.1002/2015JA021865.

Zhu, J., A. J. Ridley, and Y. Deng (2016), Simulating electron and ion temperature in a global ionosphere thermosphere model: Validation and modeling an idealized substorm, *Journal of Atmospheric and Solar-Terrestrial Physics*, *138-139*, 243–260, doi:https://doi.org/10.1016/j.jastp.2016.01.005.